DOCTOR OF PHILOSOPHY (1985) McMASTER UNIVERSITY

(Engineering) Hamilton, Ontario

TITLE: A High-Capacity Terrestrial Digital Microwave Radio System Employing Adaptive Techniques

AUTHOR: Carl Francis Weaver, B.A.Sc. (Universiy of Waterloo)

M. Eng. (McMaster University)

SUPERVISOR: Professor D. P. Taylor

NUMBER OF PAGES: xxv,194

ABSTRACT

A prototype 90 Mbit/s, 4.5 bits/cycle digital microwave radio is constructed which uses 49QPRS modulation. Feedback is used to linearize the transmitter power amplifier and in the receiver an adaptive decision feedback equalizer (DFE) is used to counter the effects of multipath distortion.

The modulation envelope at the output of the cascade of a quadrature amplitude modulator and a microwave GaAsFET power amplifier is linearized with respect to the baseband signal, by feedback of the coherently demodulated microwave output. The power amplifier was operated at the 0.5dB compression point with only a very small increase in the receiver bit error rate (BER). To be practical, the feedback loop must have small physical size so that the loop transit time is small relative to the modulation symbol period.

The receiver sampling phase and DFE tap-weights are jointly adapted to minimize the mean squared error and peak error respectively, of the DFE output. A one bit quantized estimated gradient algorithm is used to digitally adjust the adapted parameters. In the presence of a two-ray multipath, causing a transmission zero at the mid-band frequency of the

receiver, the adaptive receiver can operate with only a small increase in the BER. In addition, the adaptive receiver can track easily between the minimum phase and non-minimum phase regions which are separated by the transmission zero.

A recursive matrix equation is derived to describe the joint steepest descent adjustment of the equalizer tap-weights and sampling phase. The eigenvalues of the adjustment matrix of that equation are used to explain the observed behaviour of the constructed system.

ACKNOWLEDGEMENTS

I would like to express my gratitude to my supervisor, Dr. Desmond P. Taylor for his guidance and support throughout the course of my studies. I would like to thank fellow graduate students, Gary R. McMillen and George H. Niezgoda, for their interest in and contribution to digital radio research at McMaster University. I would also like to thank Andrew McColm for his contribution in the assembly of the transmitter, the IF transversal equalizer and for the printed circuit board layout of the accumulator board and forward equalizer board. Also, I would like to thank Com Dev Ltd. for the donation of their time to design and construct the transmitter RF filter. I would also like to thank Dr. Mansor Shafi for helping to create an atmosphere for achievement in digital radio research at McMaster University.

For their help in drawing and lettering of figures, I would like to thank Corey Holota and Jackie Holota. Finally, I would like to thank my wife Christine for her help in typing, and organizing paper, but most of all, I would like to acknowledge her continuous support, which has enabled the timely completion of this work.

TABLE OF CONTENTS

LIST OF FIGURES		ix
LIST OF TABLES		xiii
LIST OF VARIABLES		xiv
LIST OF ABBREVIATIONS		xxiii
CHAPTER 1 - INTRODUCTION		1
1.1	Historical Perspective on Terrestrial Microwave Radio	1
1.2	What Is Meant By High Capacity?	3
1.3	What Are the Alternate Technologies?	3
1.4	System Performance Measures	4
1.5	Propagation Outage	5
1.6	Current Trends in Digital Microwave Radio	9
1.7	Transmitter Power Amplifier Linearization	10
1.8	Adaptive Equalization of Multipath Distortion	12
1.9	Scope of Thesis	15
Chapter 2 - TRANSMITTER DESIGN		19
2.1	Introduction	19
2.2	Simulation of Feedback Linearized Transmitter	21
2.3	Results and Observations From Simulation	25
2.4	Implementation of the Feedback Linearized Transmitter	37

2.5	Transmit Filter Design	40
2.6	Transmitter Interface Card	48
CHAPTER 3 -	IMPLEMENTATION OF THE 49QPRS RECEIVER	49
3.1	Introduction	49
3.2	Receiver Front End Implementation	52
3.3	Bandpass Transversal Equalizer Implementation	54
3.4	Demodulator, Forward, and Backward Equalizer Implementation	57
3.5	Tap-Weight Adaptation	66
3.6	Clock Recovery	78
3.7	Carrier Recovery	83
3.8	Differential Decoding and Data Combiner Implementation	85
CHAPTER 4 -	STABILITY OF THE JOINT ADAPTATION OF TAP-WEIGHTS, SAMPLING PHASE, AND CARRIER PHASE	87
4.1	Introduction	87
4.2	System Definition	89
4.3	Minimization With Respect to Tap-Weights, Sampling Phase, Carrier Phase	97
4.4	Stability of the Steepest Descent Algorithm	102
4.5	LMS and Quantized Gradient Algorithms	109
4.6	Eigenvalues versus Multipath	118
CHAPTER 5 -	EXPERIMENTAL AND THEORETICAL PERFORMANCE OF THE 49QPRS RADIO SYSTEM	137
5.1	Introduction	137

5.2 BER Versus Receiver Input Signal Level 140

5.3 Transmitter Performance 143

5.4 Performance For Mid-Band Eading 150

5.5 Measured and Theoretical Outage Region 169

CHAPTER 6 - CONCLUSION 177

6.1 Introduction 177

6.2 Description of Significant Contributions 177

6.3 Conclusions and Future Work 180

LIST OF FIGURES

Figure	Title	Page
2.1	Transmitter Subsystems	20
2.2	Feedback Linearized Transmitter Functional Diagram	22
2.3	Power Amplifier Output versus Input Power Model	26
2.4	Power Amplifier Phase Transfer and AMPM versus Input Power Model	27
2.5	I-Q Response to a 256 Symbol Sequence Without Feedback the 0.7dB Compression Point	29
2.6	I-Q Response to a 256 Symbol Sequence With Feedback the 0.7dB Compression Point	30
2.7	Sampled I-Q Response to a 256 Symbol Sequence Without Feedback at the 0.7dB Point	31
2.8	Sampled I-Q Response to a 256 Symbol Sequence With Feedback at the 0.7dB Compression Point	32
2.9	Peak Eye Closure versus Input Power for various Loop Gains	34
2.10	Logarithm of Peak Eye Closure versus Input Power for various Loop Gains	35
2.11	Logarithm of Peak Eye Closure versus Loop Gain	36
2.12	Implemented Feedback Linearized Transmitter Block Diagram	38
2.13	Compensation Network Schematic	39
2.14	RF Multiplexing of Receiving and Transmitting Channels	42
2.15	Data Encoder Block Diagram	47
2.16	Multilevel Modulator Partial Schematic	48

3.1	Receiver Subsystems	51
3.2	Measured IF Filter Amplitude versus Frequency Response	55
3.3	Diagram of Tap-Weight Multiplier and Delay Element of the IF Transversal Equalizer	56
3.4	Functional Diagram Two Forward and Two Backward Taps of the DFE	59
3.5	Forward Equalizer Tap-Weight Multiplier and Summer Partial Schematic	61
3.6	Quantizer Input Interface Partial Schematic	63
3.7	Backward Equalizer Tap-Weight Multiplier and Summer Partial Schematic	65
3.8	Photographs of Forward Equalizer, Backward Equalizer, and Quantizer Printed Circuit Boards	67
3.9	Functional Diagram of Decision-Directed Tap-Weight Adjustment Algorithm	73
3.10	Functional Diagram of Up-Down Counter	75
3.11	Photographs of Up-Down Counter Board, Data Combiner and Clock Distribution Board, and the DFE.	77
3.12	Functional Diagram of Analog Clock and Carrier Recovery System (only considered for implementation)	80
3.13	Functional Diagram of Implemented Clock Recovery System and Proposed Carrier Recovery System	81
3.14	Differential Decoder and Data Combiner Functional Diagram	86
4.1	Functional Diagram of DFE	90
4.2	Optimum Sampling Instant versus Multipath Relative Amplitude for various Notch Frequency Offsets	122
4.3	MMSE versus Multipath Relative Amplitude for various Notch Frequency Offsets	125

4.4 MMSE versus Multipath Relative Amplitude for various Notch Frequency Offsets 126

4.5 MMSE versus Multipath Relative Amplitude for various Notch Frequency Offsets 127

4.6 Maximum Eigenvalue of Adjustment Matrix versus Multipath Relative Amplitude for various Notch Frequency Offsets 129

4.7 Minimum Eigenvalue of Adjustment Matrix versus Multipath Relative Amplitude for various Notch Frequency Offsets 130

4.8 Eigenvalue Spread of Adjustment Matrix versus Multipath Relative Amplitude for various Notch Frequency Offsets 131

4.9 Determinant of Matrix R_a versus Multipath Relative Amplitude for various Notch Frequency Offsets 134

4.10 AGC Gain versus Multipath Relative Amplitude for various Notch Frequency Offsets 135

4.11 Sum of Eigenvalues of the Adjustment Matrix versus Multipath Relative Amplitude for various Notch Frequency Offsets 136

5.1 Measured BER versus Received Signal Level and Theoretical BER Assuming Gaussian Noise 141

5.2 Transmitter Power Amplifier Output Power versus Input Power 145

5.3 Measured BER versus Amplitude Unbalance and Theoretical BER Assuming Independent Adjustment of I-axis and Q-axis Tap-Weights 147

5.4 Measured BER versus ±16° Phase Unbalances of FLT Demodulator for various FLT Modulator Phase Unbalances, and Theoretical BER versus a Simple Modulator or Demodulator Phase Unbalance 148

5.5 Transmitter Spectrum Photographs 151

5.6 Photographs of Eye Diagrams at DFE Input, and at DFE Quantizer Input Without Multipath 153

5:7	Photographs of Eye Diagrams at DFE Quantizer Input for various Relative Amplitudes of Two-Ray Multipath	155 156
5.8	Photographs of Receiver IF Spectrum at IF Filter Output for various Relative Amplitudes of Two-Ray Multipath	157 158
5.9	Measured and Theoretical Sampling Phase versus Two-Ray Multipath Relative Amplitude	160
5.10	Measured BER and Theoretical MMSE versus Two-Ray Multipath Relative Amplitude and at an RSL of -34dBm	161
5.11	Measured BER versus Two-Ray Multipath Relative Amplitude for Received Signal Levels of -34dBm and -24dBm	162
5.12	Logarithm of Reference Tap and Sampling Phase Control RMS Voltage and Logarithm of the Sum of Adjustment Matrix Eigenvalues	165
5.13	Photographs of On-axis and Cross-axis Reference Tap-Weight Voltages over One Second Time Period for various Two-Ray Multipath Relative Amplitudes	166
5.14	Measured Outage Region at SNR = 41dB and Theoretical Outage Region for τ_g equal to 16T at SNR>36dB, and Outage Region Typical of "Second Generation" Digital Radios at High SNR	171
5.15	Theoretically Predicted Outage Region for τ_g equal to 8T at SNR > 36dB and Outage Region Typical of "Second Generation" Digital Radios at High SNR	175
6.1	A Magnitude and Phase Based Method of Feedback Linearizing a Bandpass Signal, suggested for Future Investigation	179
6.2	A Clock Recovery System With Squaring Loop Derived Frequency Control and MMSE Derived Phase Control	186

LIST OF TABLES

Table	Title	Page
1.1	Trans Canada Telephone System Reference Circuit Description	2
1.2	Trans Canada System Availability Requirements	2

LIST OF VARIABLES

A	Flat fade depth (dB) in physical two-ray multipath model
A_o	Flat fade depth in Rummler's multipath model
A_v	Small signal voltage gain of PA
a	Gain of physical multipath model
$\underset{\sim}{a}$	M dimensioned complex forward tap-weight vector
$\underset{\sim}{a}_s$	M dimensioned complex forward tap-weight which satisfies Normal Equation for arbitrary sampling phase and carrier phase
a_o	Gain of Rummler's multipath model
a_k	Complex tap-weight in forward equalizer of DFE
B	Notch depth (dB) of physical two-ray multipath model
B_o	Rummler's notch depth parameter (dB)

b — Relative amplitude of physical two-ray multipath model

$\underset{\sim}{b}$ — N dimensioned complex backward tap-weight vector

$\underset{\sim}{b}_s$ — N dimensioned complex backward tap-weight vector which satisfies the Normal Equation for arbitrary sampling phase and carrier phase

b_o — Rummler's relative amplitude

b_j — Complex tap-weight in forward equalizer of DFE

$\underset{\sim}{c}$ — M+N dimensioned complex tap-weight error vector

C — Half of up-down counter size in Lucky's algorithm

d — Half the distance between signal states

$d(n)$ — Complex transmitted data and desired response at the quantizer input at the n-th sample instant

$\hat{d}(n,t_s,\Phi_c)$ — Complex estimated data at quantizer input

$\tilde{d}(n)$ — Complex decided data at n-th sample

$\underset{\sim}{D}_i$	Defined in Eq. 4.74
$e(n,t_s,\Phi_c)$	Instantaneous error between estimate of desired response and desired response
f	Frequency (except in Section 4.5)
f	Defined by Eq. 4.67 (in Section 4.5 only)
f_i	Defined by Eq. 4.65
f_o	Notch frequency offset in Rummler's model (except in Section 4.5)
f_o	Defined by Eq. 4.62 (in Section 4.5 only)
$\underset{\sim}{g}$	Defined in Eq. 4.63
$\underset{\sim}{g}_i$	Defined in Eq. 4.66
$\underset{\sim}{g}_Q$	Defined in Eq. 4.61
$g_T(t)$	$= 1$ for $-T/2 < t < T/2$ $= 0$ elsewhere
H_o	Rummler's multipath transfer function
H_p	A two-ray multipath transfer function in which the relative amplitude b may be greater than one
$h_r(t)$	Impulse response of system to DFE input

J	Mean squared error cost function
$\bar{K}$	Mean number of counts between a single tap-weight adjusment in Lucky's algorithm
M	Number of forward taps of DFE
N	Number of backward taps of DFE
P_e	Probability of symbol detection error
P_c	Probability of correct tap-weight adjustment in Lucky's algorithm
P_g	Probability of correct gradient indication in Lucky's algorithm
P_r	Ideal or non-distorted PA output power
$\underset{\sim}{p}$	2(M+N)+1 dimensioned real parameter vector containing both real and imaginary parts of tap-weights and the sampling phase
$\underset{\sim}{Q}$	Matrix of eigenvectors of adjustment matrix
R_o	Signal magnitude at PA output
$\underset{\sim}{R}_{ro}$	Defined in Eq. 4.72
$\underset{\sim}{R}_{so}$	Defined in Eq. 4.73

r_d	Sampled autocorrelation function of desired response
$r_{du}(k,t_s,\Phi_c)$	Cross-correlation function of desired response and an equalizer data value
$\underset{\sim}{r}_{du}$	M+N dimensioned cross-correlation vector of the desired response and the equalizer data
$\underset{\sim}{r}_{duo}$	$\underset{\sim}{r}_{du}$ evaluated at sampling phase error of zero
$\underset{\sim}{r}_{df}$	M dimensioned cross-correlation vector of the desired response and forward equalizer data
$\underset{\sim}{r}_{db}$	N dimensioned cross-correlation vector of the desired response and backward equalizer data
$r_u(k,t_s)$	Autocorrelation function of equalizer input data
$\underset{\sim}{R}_a$	See Equation 4.33 on p. 98
$\underset{\sim}{R}_{bb}$	N square autocorrelation matrix of the backward equalizer data vector
$\underset{\sim}{R}_{fb}$	M by N dimensioned correlation matrix of the forward equalizer and backward equalizer data vectors
$\underset{\sim}{R}_{ff}$	M square autocorrelation matrix of the forward equalizer data vector

$\underset{\sim}{R}_p$	2(M+N)+1 real square matrix defined in Equation 4.69 and 4.70
$\underset{\sim}{R}_{po}$	$\underset{\sim}{R}_p$ evaluated for zero sampling phase error
$\underset{\sim}{R}_u$	M+N square autocorrelation matrix of the equalizer data vector
$\underset{\sim}{R}_{uo}$	$\underset{\sim}{R}_u$ evaluated at zero sampling phase error
$\underset{\sim}{R}_{ui}$	See Equation 4.60
s	Complex frequency of Laplace transform
T	Time period of transmitted data symbol
t	Time
t_o	Receiver sampling phase which satisfies $\nabla_t = 0$
t_e	Receiver sampling phase error
t_s	Receiver sampling phase estimate
$u(t,n+M-1,\Phi)$	Complex received signal at input to decision feedback equalizer
$\underset{\sim}{u}$	M+N dimensioned data vector including data in forward and backward equalizer
$\underset{\sim}{u}_f$	M dimensioned data vector of data in forward equalizer

$\underset{\sim}{u}_b$	N dimensioned data vector of data in backward equalizer
V_d	Complex FLT input signal
V_e	Complex FLT error siganl
V_f	Complex FLT output signal
V_i	Complex PA input signal
V_o	Complex PA output signal
$\underset{\sim}{w}_s$	M+N dimensioned complex tap-weight vector which satisfies Normal Equation for arbitrary sampling phase and carrier phase
$\underset{\sim}{w}_o$	M+N dimensioned complex tap-weight vector which satisfies Normal Equation for sampling phase t_o and carrier phase Φ_o
$\underset{\sim}{w}$	M+N dimensioned complex tap-weight vector
$z(t,n,\Phi)$	Signal at quantizer input of DFE
ε	A small tap-weight error
$\underset{\sim}{\nabla}_w$	Gradient of mean square error with respect to the tap-weight vector

∇_t	Gradient of mean square error with respect to sampling phase
∇_Φ	Gradient of mean square error with respect to carrier phase
$\nabla_{\underset{\sim}{p}}$	Gradient of mean square error with respect to a parameter vector
Δ	Distance between quantization levels of tap-weights in the single bit quantized gradient algorithm
ϵ_o	An allowable increase in cost defining the convergent region of a cost function
$\underset{\sim}{\Lambda}$	Diagonal matrix containing the eigenvalues of the adjustment matrix $\underset{\sim}{R}_{po}$
λ	Eigenvalue of the adjustment matrix $\underset{\sim}{R}_{po}$
μ	Step size of the steepest descent algorithm
σ^2	Variance of thermal noise and residual ISI
τ	Delay time between two rays of multipath model
τ_a	Overall time constant of adaptive system
τ_g	Half amplitude time period of Gaussian pulse

τ_d	Loop transit time in FLT
Φ	Phase
Φ_c	Receiver carrier estimate
Φ_o	Carrier phase which satisfies $\alpha_\Phi = 0$ (except in Chapter 2)
Φ_o	PA output phase (in Chapter 2 only)
ω	Radian frequency
ω_a	Frequency of a FLT transfer function zero
ω_b	Frequency of a FLT transfer function pole
ω_c	Frequency of a FLT transfer function pole

LIST OF ABBREVIATIONS

A/D	Analog to Digital Convertor
AC	Alternating Current
AGC	Automatic Gain Control
BE	Backward Equalizer
BER	Bit Error Rate
BNR	Bell Northern Research
C/N	Carrier to Noise Ratio
D/A	Digital to Analog Convertor
DC	Direct Current
DFE	Decision Feedback Equalizer
DS-3	Digital System -3 , a telephone system for communicating 672 telephone voice channnels in 44.736 Mbits/s time multiplexed data streams
ECL	Emitter Coupled Logic
FCC	Federal Communications Commission (in U.S.A.)
FE	Forward Equalizer (part of DFE)
FET	Field Effect Transistor
FLT	Feedback Linearized Transmitter
FM	Frequency Modulation
I-axis	Real axis of complex baseband signal or in phase reference of bandpass signal
IPA	Intermediate Power Amplifier

I-Q	Real and Imaginary axes of complex baseband signal or in phase and quadrature phase reference of a bandpass signal
IF	Intermediate Frequency of super-heterodyne receiver
ISI	Inter-Symbol-Interference
LNA	Low Noise Amplifier
LMS	Least Mean Square
LSI	Large Scale Integration
NMP	Non-Minimum Phase
MSE	Mean Square Error
MMSE	Minimum Mean Square Error
MP	Minimum Phase
MSI	Medium Scale Integration
MZF	Modified-Zero Forcing
PA	Power Amplifier
PCB	Printed Circuit Board
PN	Pseudo-Noise
PROM	Programable Read Only Memory
QAM	Quadrature Amplitude Modulation
Q-axis	Imaginary axis of complex baseband signal or quadrature phase reference of a bandpass signal
QPRS	Quadrature Partial Response Signaling
RF	Radio Frequency
RSL	Received-Signal Level
SNR	Signal to Noise Ratio
SMA	A type of Sub-Miniature coaxial connector

SRSP	Standard Radio System Plan, from Government of Canada
S100	A standard used in small computer systems
TE	Transversal Equalizer
TTL	Transistor-Transistor Logic
TWT	Traveling Wave Tube
XPD	Cross Polarization Discrimination
ZF	Zero Forcing

CHAPTER 1

INTRODUCTION

1.1 Historical Perspective on Terrestrial Microwave Radio

Microwave radio systems have been employed since the 1940's[1] for the communication of long distance telephone traffic, network television signals, and more recently, high-speed data and computer information. A terrestrial system uses high gain (highly directional) antenna systems and a chain of repeaters, each consisting of a receiver and transmitter to carry signals from point to point along the earth's surface. A typical long distance or "long haul" system consists of a large number of radio repeaters (100 to 200) [2] spaced at an average distance of 45km. Each repeater is allocated a channel bandwidth of between 20 MHz and 40 MHz at some carrier frequency between 2 and 11 GHz, in a wide band frequency allocation. Because the whole frequency allocation is to be used, there are adjacent channels which usually use the opposite antenna polarization to increase adjacent channel discrimination. A specific system usually operates in a set frequency band according to government regulation[3] or international agreement[4], and a typical communications path has the characteristics given[2] in Table 1.1.

TABLE 1.1

TRANS CANADA TELEPHONE SYSTEM REFERENCE CIRCUIT DESCRIPTION

REFERENCE CIRCUIT LENGTH (RADIO ONLY)	6560	KM
NUMBER OF RADIO SECTIONS	8	
SECTION LENGTH	820	KM
NUMBER OF HOPS IN REFERENCE CIRCUIT	144	
NUMBER OF HOPS/SECTION	16	
HOP LENGTH	45.5	KM
NUMBER OF VOICE CHANNELS/RF CHANNEL	1344	
NUMBER OF DS-3 SIGNALS/CHANNEL	2	
RADIO FREQUENCY BAND	8 GHz	PER SRSP 306 ISSUE 2

TABLE 1.2

TRANS CANADA TELEPHONE SYSTEM AVAILABILITY REQUIREMENTS

OVERALL ANNUAL AVAILABILITY INCLUDING OPERATIONS AND "ACTS OF GOD"	99.9%
OVERALL ANNUAL AVAILABILITY OBJECTIVE INCLUDING EQUIPMENT AND PROPAGATION OUTAGES ONLY	99.8%
OVERALL EQUIPMENT OUTAGE CONTRIBUTIONS	0.01%
OVERALL PROPAGATION OUTAGE CONTRIBUTIONS	0.01%
OUTAGE THRESHOLD	BER < 10^{-4}
ONE HOP PROPAGATION OUTAGE OBJECTIVE (REFERENCE HOP RAIN AND MULTIPATH)	.694 x 10^{-4}
ONE SECTION EQUIPMENT OUTAGE INCLUDING 1:N FREQUENCY DIVERSITY PROTECTION SWITCHING OR HOT STANDBY	0.125 x 10^{-4}

The first systems used analog frequency modulation of the radio carrier and carried 240 telephone voice circuits per channel as a frequency division multiplexed signal[1]. Analog FM systems have evolved to the point of carrying 1500 telephone voice circuits in a 20 MHz channel[1]. In the 1970's, the advent of digital switching and the greatly improved technology of time domain switching and multiplexing has favoured a switch to digital modulation methods, even though the digital radio systems are more expensive[5].

1.2 What Is Meant By High Capacity?

When we refer to a microwave radio as having high capacity, it is meant that we are dealing with large channel bandwidths and/or high bit rates. Also, it is assumed that the channel bandwidth is being used as efficiently as is practicable; given the "state of the art" in technology. Typical bit rates for digital radios are presently 90 Mbits/s or 135 Mbits/s for 20 MHz and 30 MHz channels, and typical efficiencies are 4.5 bits/cycle.

1.3 What are the Alternate Technologies?

The main alternatives for high rate communications are satellite-relay microwave systems and lightwave fibre optic cable systems. There are reasons to favour these alternatives over terrestrial microwave radio, in some applications. For example, transoceanic communications and broadcast communications favour the use of satellite systems. Fibre optic light wave systems have larger bandwidths than radio and are immune to interference and propagation problems. Two drawbacks of lightwave systems relative to terrestrial radio, are the need for a "right of way" and system installation costs. Satellite systems require longer time periods for planning and implementation than terrestrial systems. The attractive feature of terrestrial radio systems for telephone communications is the fact that the "microwave routes" consisting of towers, buildings, and antenna systems are already in existence so that the planning and implementation of additional capacity on an existing route can be done in a short time span with a relatively small amount of effort, when only the radio electronics needs to be added.

1.4 System Performance Measures

When a microwave radio system for telephone system use is constructed, the most important consideration is the cost per telephone voice channel per unit distance. In a digital system, an equivalent measure is the cost per unit bit rate per unit distance. The main performance measure is the system availability, which is the percentage of time that the system is operational. Typical system availability requirements are given in Table 1.2. One accepted standard (U.S.A.) for being considered operational is that the bit error rate (BER) be less than 10^{-3}. The standard used in Canada is 10^{-4}. Another way of expressing availability is as the percentage of one second increments of time that are free of errors [1], i.e. error-free seconds. This later type of measure has been derived from considerations of data service quality as opposed to consideration of voice channel performance [1]. End to end availability objectives are typically 99.98% for a BER of 10^{-3} or 99.5% in error-free seconds so that the most difficult systems from an availability point of view are the long haul or multihop systems. The .02% allowed outage is approximately 9 minutes per month. In the case of availability based on a BER threshold of 10^{-3} the 0.02% of allowed outage is divided equally between two sources, namely, outage due to equipment failure and outage due to poor propagation conditions. Equipment outage is controlled by good design practice and by the use of standby equipment or a standby protection channel. Controlling the outage due to propagation is more complex, especially when digital modulation methods are considered. This will be the subject of investigation in the following sections, and indeed throughout this thesis.

1.5 Propagation Outage

Outage due to propagation conditions can be separated into three significant processes[6],[7]. The main source of propagation outage at lower microwave frequencies is atmospheric multipath which causes distortion or loss of the desired signal leading to degradation of the BER to the 10^{-3} threshold. It is usually assumed that the radio hops are designed with antennas and towers positioned so that ground reflections or water reflections are insignificant. The second source which contributes to outage is atmospheric absorption. Atmospheric absorption is primarily due to rain or moisture and is significant primarily only at the higher frequency bands of 8GHz and 11GHz. Atmospheric absorption due to rain is usually referred to as rain fading. The third source of fading is called obstructive fading or "blackout" fading[7]. It is caused by large changes in the refractive index of the atmosphere. These cause a transmitter to receiver path, which is normally line of sight, to be blocked by obstructions on the ground. The occurrence of obstructive fading is rare. With adequate clearance of the line of sight path, with respect to the ground or obstructions, it can usually be ignored. Both rain and multipath can cause flat amplitude versus frequency fading which is referred to as flat fading. Multi-path can also cause fading in which the amplitude varies significantly with frequency. This is referred to as frequency selective or time dispersive fading.

When analog FM radios were used, the degradation due to multipath was determined primarily by the signal attenuation or fade depth toward a noise threshold. The time dispersion effects of the multipath were not considered to be significant. Empirical probability distributions of fade depth were used[8] to predict the probability of outage when the radio hop was designed with a given fade margin. Fade margin is the difference (in dB) between the no-multipath received signal level and the received signal level which would cause the minimum acceptable level of performance. By 1977, it was recognized at Bell Northern Research[6,9] and Bell Labs [10,11,12,13,14], that the probability of outage even for simple, low-level digital modulation methods tended to be dominated by the time dispersion effects of the multipath, and when typical fade margins of 40dB to 50dB were used, the probability of outage for digital systems was much higher than predicted by the fading theory which had been used for FM analog systems. Also, at this time, Bell Northern Research [6,9] first noted the synergistic improvement available from the combined use of a space diversity antenna (two element vertical array) system and a simple adaptive frequency domain equalizer. About the same time, several authors from Bell Labs [10,11,13,15] undertook various approaches to obtain frequency selective fading models which would be useful in predicting multipath outage for digital radios. Since 1978, the fade margin to the thermal noise threshold has been referred to as the "flat fade margin" to differentiate it from an "effective fade margin" obtained in the presence of frequency selective fading.

One very useful model for multipath fading, developed by Rummler[13], is a baseband equivalent model and has a voltage transfer function of the form,

$$H_o(f) = a_o \; (1 - b_o \exp(-j2\pi(f-f_o)\tau)) \qquad (1.1)$$

where the parameter a_o is the direct ray amplitude and the parameter b_o is the relative amplitude of the second ray with respect to the direct ray at a relative time delay of τ. This model has a minimum or notch at a frequency offset of f_o Hz away from zero or midband frequency and has minima or notches which repeat at $1/\tau$ intervals in frequency, although, the only one of interest here is the notch at f_o since Rummler determined the model from measurements taken over a bandwidth of only 26 MHz. The flat fade component due to the parameter a_o can be interpreted as being due to an additional ray or rays which have relative delays too small to produce significant amplitude variation versus frequency and is not usually due to some real flat fading mechanism. In order to find unique sets of values to describe observed fading events, Rummler found it convenient to fix the relative delay parameter τ at 6.3ns and then determine the empirical probability distributions for each of the other model parameters. Since observations were taken in a bandwidth of 26 MHz it is emphasized that the model is valid over approximately that bandwidth. Usually the amplitude fading parameters are referred to in dB as,

$$A_o = -20 \log_{10} a_o \qquad a_o \geq 0 \qquad (1.2)$$

$$B_o = -20 \log_{10} (1-b_o) \qquad 1 \geq b_o \geq 0 \qquad (1.3)$$

where A_o is the flat fade depth due to multipath and B_o is the notch depth due to the frequency selective part of the multipath. To include non-minimum phase fading in Rummler's model the sign of the relative delay τ is switched. In Chapter 4, a physical two-ray model is defined in which the relative amplitude parameter is allowed to be greater than one. The relationship between this model and Rummler's model will also be given in Chapter 4.

Once it became known that the outage of a digital radio could be strongly affected by the time dispersive effects of the multipath, it became common for equipment manufacturers and researchers to present an outage signature which is the locus of values of notch frequency and notch depth for a relative delay of 6.3ns that cause a BER of 10^{-3} at high signal to noise ratio. Normally, an outage signature would contain one curve for minimum phase multipath and one for non-minimum phase multipath.

1.6 Current Trends in Digital Microwave Radio

The first generation of long haul digital radios had spectral efficiencies of between 2 and 2.25 bits/Hz. When expressed in terms of the number of telephone voice channels per unit bandwidth, the first generation digital radios had less than half the efficiency of the analog FM systems they were replacing. This was due in part to the fact that the telephone voice channels are not efficiently source coded and in part to the fact that the high SNR usually found in microwave channels had not been exploited by the use of more complex and efficient modulation methods. Since the usable radio spectrum is a finite resource and the inefficient use of this resource leads to dwindling supply and higher costs for new service, there has been considerable interest in the last few years in improving the capacity of digital microwave radios[16,17,18,19,20]. The second generation[1] of long haul digital microwave radios which have been emerging in the last two years have been designed with capacities of 4.5 bits/cycle. The modulation method used in these implementations has been almost exclusively 64 state quadrature amplitude modulation (64QAM). Quadrature amplitude modulation (QAM) is obtained by summing a sine wave and cosine wave at the carrier frequency, which have each been amplitude modulated by multi-level data streams which are normally independent. Two 8-level data streams are used to obtain 64QAM. A few authors [20,29,30,31] have also studied the use of 49 state quadrature partial response (49QPRS) modulation. This modulation can be obtained from a QAM modulated signal by filtering with a cosine shaped (in frequency) filter. This filter sums every two adjacent symbols and thereby reduces the bandwidth by a factor of two. A 16QAM input siganl to a cosine shaped partial response filter provides a 49QPRS output.

The use of multi-level modulations to improve spectral efficiency, has compounded the already difficult problem of multipath distortion controlled outage, and has introduced a new problem to the design of digital microwave radio systems.

1.7 Transmitter Power Amplifier Linearizaton

In the past, primarily only constant envelope modulation methods were used in both analog and digital microwave systems. The use of constant envelope modulations allowed operation of the transmitter PA at its saturated output power. With multilevel digital modulations, the PA must be operated with the output power reduced by at least 10dB from its saturated output level to maintain the required degree of linearity. This means that a PA with at least ten times larger saturated output power is required to maintain the same transmit power level. Since PA costs seem to rise almost exponentially with their saturated output power capability and since the operating costs also go up linearly, it is important to consider the use of linearization techniques so that costs and performance can be maintained closer to the levels previously experienced in constant envelope systems.

Three previously suggested methods of coping with PA nonlinearities[21] are: predistortion of the PA input signal to obtain an undistorted output, superposed modulation, and feed-forward linearization of the PA.

Predistortion can be done in continuous or discrete time [21,22,23]. Discrete time adaptive predistortion which was invented by Davis and Boyd[23,24] has been used in several applications of 64QAM[22,23]. Adaptive predistortion offers better performance without being concerned about PA parameter variation, however, non-adaptive predistortion control has also been used in several of the latest 64QAM radios [17,18,19].

Superposed modulation [21,25] is the weighted vector addition of two or more constant envelope 4QAM signals to obtain the desired multi-level modulation. The disadvantages of this method are the need for more than one PA and the requirement for precise power balance between them.

Feedforward error control [26,27] linearizes the PA by comparing the input and attenuated output signals. The result is amplified and subtracted from the output to obtain an undistorted output signal. It is a simple and yet effective approach but requires at least two PA's.

In this thesis, one of the oldest methods of adaptive distortion correction in electronic systems will be used to linearize the transmitter power amplifier. This method is feedback [28]. The main problem in using feedback for linearizing a microwave radio PA in the past [26] has been that the commonly used PA's were either travelling wave tubes (TWT) or else klystron tubes. The TWT is a slow wave structure and the klystron is a narrow bandwidth structure. For the signal bandwidths under consideration, both have too high a signal transit time for the stable use of feedback even when action is taken to linearize only the envelope of the RF signal. However, by the use of solid state PA's which can have low transit time and by using feedback action to linearize the modulation envelope only, the use of feedback in this application becomes feasible.

1.8 Adaptive Equalization of Multipath Distortion

In 1977, the first digital microwave radio system with demonstrated performance of long haul availability requirements was introduced by BNR [6,9]. As stated previously, it was shown at that time by Anderson, Barber, and Patel of BNR that combined space diversity and slope-amplitude adaptive equalizers would provide the required availability. Since that time almost every manufacturer of digital radio has included a space diversity combiner and an adaptive frequency domain equalizer as options in the receiver IF subsection. In the second generation of long haul digital radio (4.5 bits/cycle) this same practice has been used along with an additional adaptive transversal equalizer at baseband [16,17,18,19] in order to meet the long haul availability requirements. The outage signatures achieved in the second generation equipment range between 15dB and 20dB for the allowable notch depths for notch frequency offsets ranging up to an absolute value between 8MHz and 12MHz from midband (equivalently zero frequency). From measured field results[19] this outage signature provides the required long haul availability when it is used in conjunction with space diversity.

In this thesis, an adaptive decision feedback equalizer (DFE) with 5 forward and 5 backward taps is developed and implemented in a 4.5bits/cycle digital radio. The objective is to equalize an infinite notch depth for high SNR without the use of space diversity, and thereby, reduce the outage due to multipath fading. This particular application of a DFE has been studied by computer simulation [64,31]. A novel feature of this DFE implementation is the jointly adaptive adjustment of the equalizer tap-weights and the receiver sampling phase (timing recovery). Recently, Dudek et al.[66] have implemented a simpler DFE in a digital radio application, and Leclert et al.[60] have also simulated the application of a DFE in a digital radio applicaton.

The first use [32] of feedback equalization dates back to work by Milnor [33] and MacColl [34]. In this early work, only postcursor inter-symbol interference (ISI) was considered. Later, Austin [35] considered both precursor and post-cursor ISI by using a forward equalizer to equalize the precursor ISI. The first minimum mean square error (MMSE) adjustment algorithm for a DFE was obtained by Monsen[32,36]. Monsen also examined the adjustment and tracking of a DFE in a multipath fading environment (a troposcatter channel)[32,37,49]. George et al.[38] compared the use of a DFE and a linear equalizer in equalizing the channel impulse response using an adaptive control method invented by Lucky[39] to obtain both a MMSE and a zero forcing (ZF) solution to the tap-weight adjustment problem. Lucky's[39] single bit quantized up-down counter method of adaptation is both robust and extremely simple to implement, at a cost of added adaptation time, and is the method used for implementation in this thesis.

Jointly adaptive estimation of carrier phase, timing phase, and equalizer tap-weights in order to minimize the MSE has been considered by Chang [40] and Kobayashi[41]. Qureshi [42] has considered jointly adaptive timing and tap-weight adaptation for partial response systems. Salzberg [43], Gitlin et al. [44], and Sailer [45] have considered MMSE timing recovery methods and Falconer [46] has examined the joint estimation of carrier phase and tap-weights. In this thesis, we will investigate, both theoretically and experimentally, the jointly adaptive MMSE estimation of the carrier phase, timing phase and tap-weights. We note that it was recently found by Niezgoda[64] that timing recovery methods not based on a MSE approach were more than an order of magnitude worse in MSE under multipath fading conditions.

Siller [48] and Monsen [49] have given survey accounts of multipath propagation and countermeasures in microwave channels and troposcatter channels, respectively, while Qureshi [50] has given a tutorial account of the techniques available for the adaptive equalization of telephone voice channels. Many of these techniques are now being applied.

1.9 Scope of Thesis

There are three main objectives in this thesis as follows,

i) Show that feedback can be used from the output of a direct RF modulator and solid state power amplifier in series to linearize the power amplifier. By linearizing the power amplifier, it will be shown that the amplifier may be operated up to its 0.5dB compression point with little or no effect on the BER of a multi-level modulation such as 16QAM.

ii) Show that a Decision Feedback Equalizer (DFE) can be used to obtain greatly improved equipment outage signatures without the use of space diversity or a slope-adaptive frequency domain equalizer. Specifically, it will be shown that a 5 forward plus 5 backward tap DFE employing jointly adaptive sampling phase and tap-weights can equalize an infinite notch depth and can track between the minimum phase (MP) region and the non-minimum phase (NMP) region of a two ray frequency selective multipath channel as characterized by Rummler's model.

iii) Show how to obtain a single matrix recursive equation for the joint adaptation of tap-weights and sampling phase in a form applicable to the method of steepest descent, which by an orthogonal similarity transformation can be expressed as a set of independent first order difference equations. Each difference equation contains an eigenvalue of an adjustment matrix. The eigenvalues so obtained can be used to obtain the adaptive algorithm parameters so as to ensure adaptive system stability and tracking performance.

In order to demonstrate the attaining of the first two objectives, a 4.5 bits/cycle 49 state quadrature partial response (49QPRS) modulated digital radio has been constructed. It operates in the 4GHz band at a bit rate of 90 Mbits/s. In the transmitter, the linearized direct modulator and power amplifier operate to produce a linearized 16 state quadrature amplitude modulation (16QAM) which is then applied to a transmit RF multiplexing or branching filter. The branching filter also provides partial response filtering to obtain the 49QPRS signal and to restrict the transmit spectrum to a 20MHz band as specified by the FCC[51] mask. Figure 2.1 is a block diagram of the transmitter. The receiver contains an RF multiplexing or branching filter, an RF preamp, a downconverter, an IF filter which provides out-of-band signal rejection, an AGC amplifier, a manually adjustable IF transversal equalizer, a demodulator, and the jointly adaptive DFE. Figure 3.1 is a block diagram of the receiver. The DFE tap-weights and sampling phase are all adjusted digitally using the single bit quantized gradient method developed by Lucky[39]. The tap-weight adjustment is decision directed while the sampling phase adjustment is based on a one bit quantized estimate of the derivative of the presampled signal.

Chapters 2 and 3 deal with the designs of the transmitter and the receiver respectively. In Chapter 4, eigenvalues are determined for the joint adjustment of timing and tap-weights via the steepest descent method over a range of parameter values of the two ray multipath channel. Although the implemented system uses a nonlinear method of tap-weight and timing adjustment, it will be seen in Chapter 5, where measured lab results are presented, that the calculated eigenvalues explain the observed lab performance. Chapter 6 provides conclusions and suggestions for future work.

CHAPTER 2

TRANSMITTER DESIGN

2.1 Introduction

The design of the linearized transmitter is considered in three parts as shown in Figure 2.1. The first part is the transmitter interface card which accepts a 90 Mbit/s binary (ECL levels) data input and provides two four level outputs at a rate of 22.5 Mbaud and which are equally likely with a mean value of zero volts provided the input data is sample-to-sample independent and equally likely. The second part is the feedback linearized transmitter, which accepts the two four level data streams and provides a 16QAM modulated output centred at 4050 MHz with a power level of approximately one Watt. The third part is the transmit RF filter which provides partial response filtering to obtain a 49QPR modulation from the 16QAM modulated input.

In order to gain a better understanding of the operation of feedback linearization of a QAM modulator and power amplifier an analytical simulation was performed. The simulation is described in Section 2.2 and the results of the simulation are given in Section 2.3. In Section 2.4 all the details of hardware implementaton of the feedback linearized transmitter are given. In Section 2.5, the design details pertaining to the transmit RF filter are given and

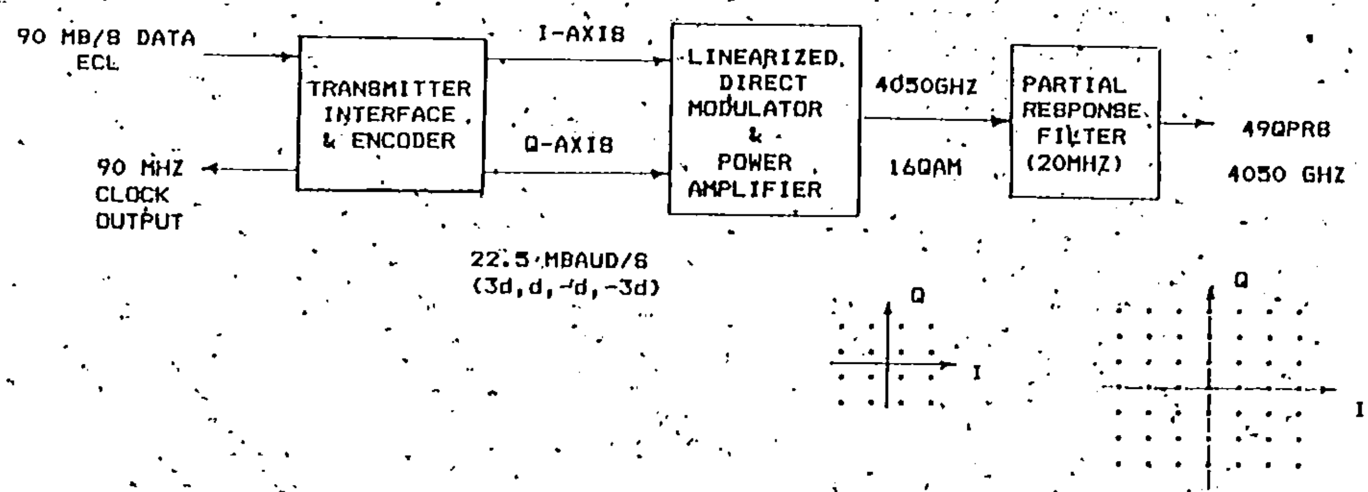

Figure 2.1 Transmitter Subsystems

in Section 2.6 the design of the transmitter interface card is presented.

2.2 Simulation of Feedback Linearized Transmitter

The transmitter section functional block diagram shown in Figure 2.2 is first described. The baseband data sequences are first added to the negative demodulated PA output data sequences to form in-phase and quadrature phase error signals. The input data sequences are quaternary, equally likely, and have zero mean. The error signals are passed through a compensation network. The compensated error signals are applied to a QAM modulator to produce a 16 QAM modulated signal at 4 GHz, which is amplified by a 5 dBW GaAs FET PA. The PA output is split unequally with the small portion being demodulated to obtain the error signal. The other portion is the 16 QAM high power output which is applied to an RF multiplexing filter which provides pulse shaping to obtain the 49QPRS signal. The carrier generator output to the demodulator is phase adjusted to coherently demodulate the PA output in a negative sense to provide negative feedback at the input summer. Critical to the operation of the feedback loop is the use of the GaAs FET PA. A TWT PA or other slow wave device could not be used due to the long transit times. Also critical to the loop operation is minimization of the physical size, to minimize

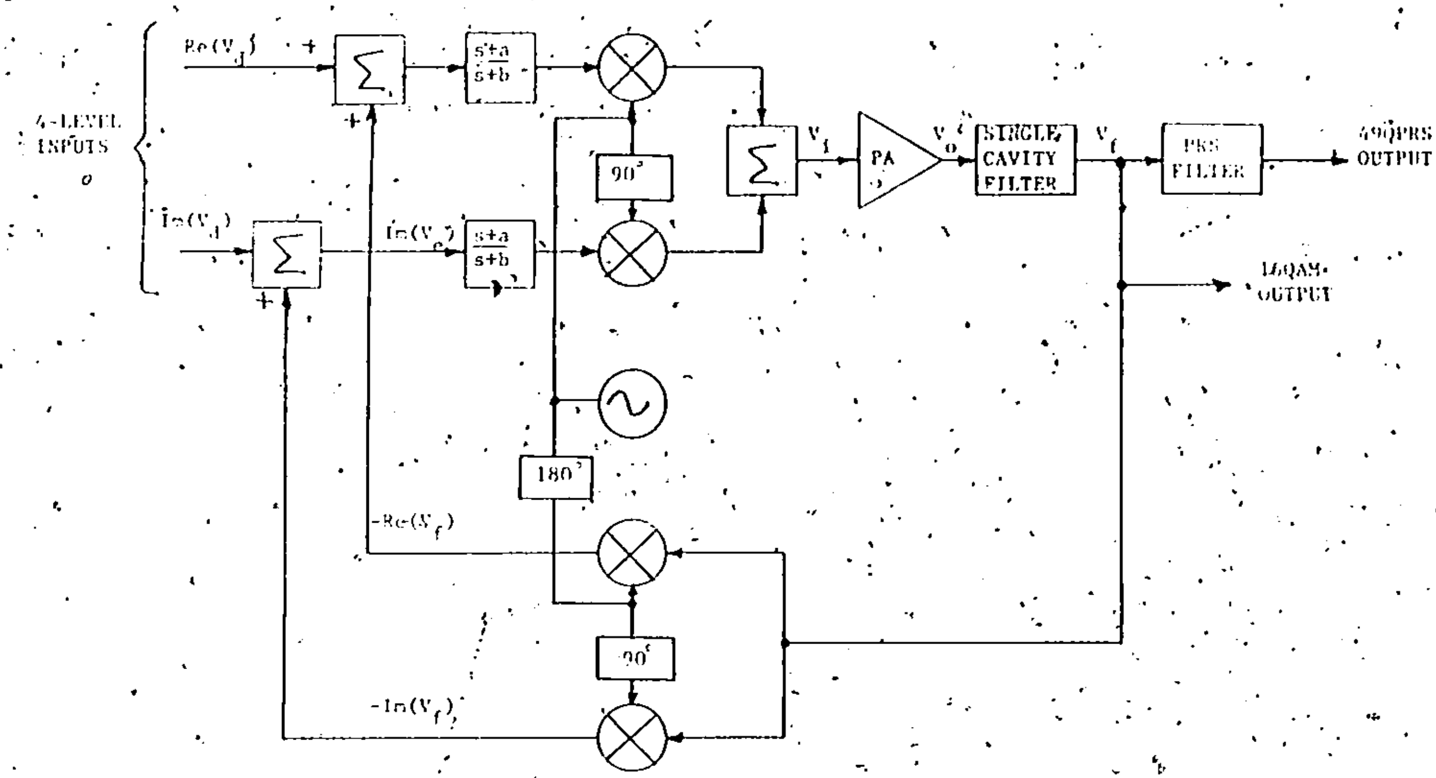

Figure 2.2 Feedback Linearized Transmitter Functional Diagram

loop transit times.

To determine the degree of linearization achieved by the feedback linearized transmitter (FLT) and also to aid in the design and construction of the equipment, a simulation of the FLT response to a data sequence was performed. The model used is exactly as shown in Figure 2.2, except that the baseband pole implied by the "single cavity filter" will not necessarily be due to a filter placed in the loop. It could be caused by the finite bandwidth of any of the loop components. In any case, the compensation network will be adjusted to maximize loop bandwidth consistent with good loop stability.

The data sequences used were a 256 symbol sequence and a 16 symbol sequence. The 256 symbol sequence was formed as follows. A 255 bit PN sequence was repeated four times beginning at a register value of 00000001 (assuming the register is shifted left) to obtain a 1020 bit sequence. One zero is added at the beginning and three zeros are added at the end to form a 1024 bit sequence. The 1024 bit sequence is then taken four bits at a time to obtain a 16-ary 256-symbol sequence which contains every permutation of two with replacement of the possible 16QAM symbols. The 16 symbol sequence is formed in a similar way and has every possible 16QAM symbol.

The output signal is calculated by obtaining the differential equations and nonlinear equation of the PA and solving the set of equations numerically. The equations for the compensation network and the PA output filter are,

$$\dot{V}_i = (\omega_b/\omega_a)\dot{V}_e + \omega_b V_e - \omega_b V_i \qquad (2.1)$$

$$\dot{V}_f = \omega_c V_o - \omega_c V_f \qquad (2.2)$$

where V_i is the complex input voltage

V_e is the complex error voltage

V_o is the complex PA output voltage

V_f is the complex FLT output

$$V_f(s) = \frac{\omega_c}{s+\omega_c} V_o(s) \qquad (2.3)$$

and

$$V_i(s) = \frac{\omega_b}{\omega_a} \left(\frac{s+\omega_a}{s+\omega_b}\right) V_e(s) \qquad (2.4)$$

The FLT loop error signal is given by,

$$V_e(t) = V_d(t) - V_f(t-\tau_d) \qquad (2.5)$$

where V_d is the complex FLT input voltage

τ_d is the loop transit time

The time dependence is assumed in all equations and is explicitly shown in (2.5) to indicate the effect of the transit time τ in the loop model. The GaAs FET PA transfer equation is,

$$V_o = R_o \exp[j\Phi_o] \qquad (2.6)$$

$$R_o = (\arctan[P_r^{3/2}])^{1/3} \qquad (2.7)$$

$$\Phi_o = \arctan[Im(V_i)/Re(V_i)] + \pi/45\ (\ \pi/2 - \arctan[\ (\ (5/2)\log_{10}(P_r)\ )^2\ ]\ )\ ; \tag{2.8}$$

$$P_r = A_v^2\ V_i\ V_i^* . \tag{2.9}$$

where R_o is the PA output voltage magnitude

Φ_o is the PA output phase

P_r is the ideal PA output power

A_v is the PA scalar small signal voltage gain .

This PA model was derived to fit the typical power transfer and phase transfer characteristics of the particular PA (Fujitsu (GB374203-02)) being used. It is important to note the use of the word "typical" to describe the PA transfer characteristic, since the small signal gain and compression characteristic vary significantly with temperature while the saturated output power varies much less than the small signal gain. Figure 2.3 shows the output power versus input power and Figure 2.4 shows phase shift and AM/PM conversion versus input power for the model given.

2.3 Results and Observations from Simulation

Before discussing the results three points should be made. First, none of the simulation parameters had been optimized for performance. Second, all the results presented are with a transit time of 0.1 ns even though the hardware loop has larger transit time. This is not a problem as long as the phase shift due to time delay is not large enough to

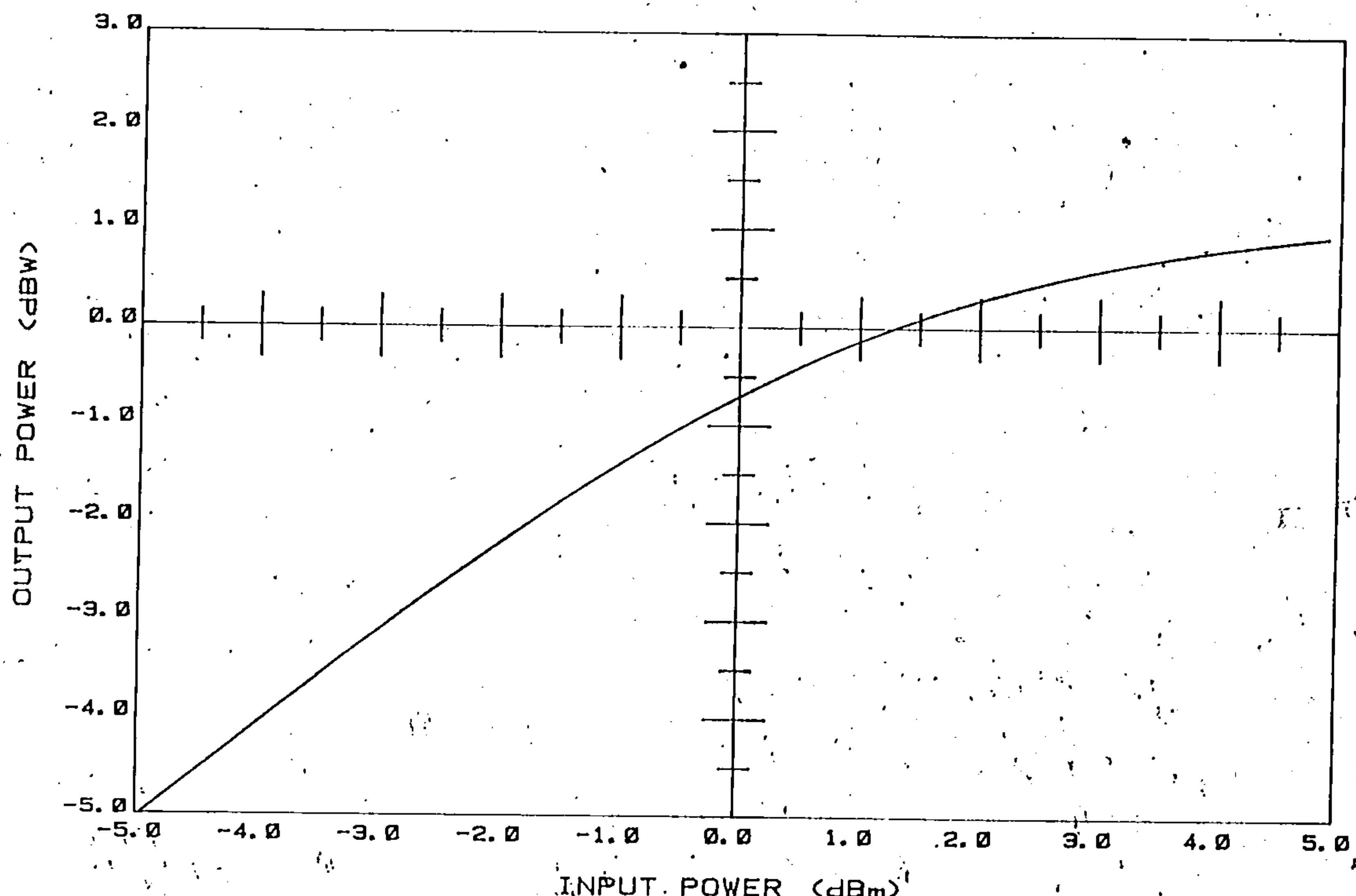

Figure 2.3 Power Amplifier Output versus Input Power Model

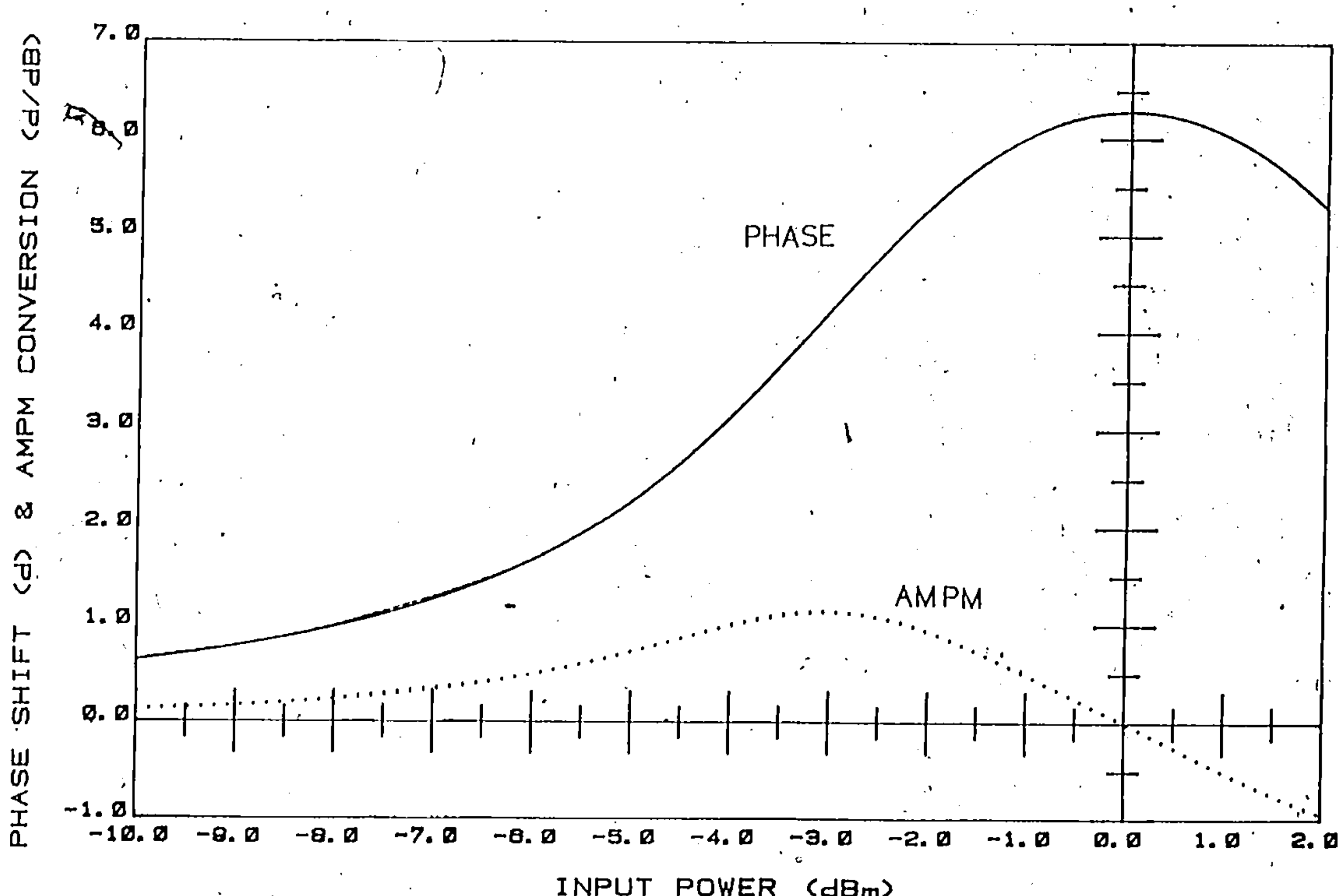

Figure 2.4 Power Amplifier Phase Transfer and AMPM versus Input Power Model

cause instability. Third, the back-offs quoted are input power back-offs relative to the 0 dB input point in Figure 2.3. At the 0 dB input point in Figure 2.3 the amplifier gain is 0.7 dB below the small signal gain. This is also referred to as the 0.7 dB compression point. Also, the input power implied is not the average over all the symbols but is the power of the largest symbol.

Figures 2.5, 2.6, 2.7 and 2.8 show the output signal for the 256 symbol sequence with and without feedback for continuous time and then for samples at mid-symbol. The transmitter small signal bandwidth in either case is about 3.3 times the symbol rate. The "no feedback" case in Figure 2.5 and 2.6 has a single pole model. It is seen that the feedback introduces intersymbol interference (ISI) at the pulse edge. This interference becomes more substantial as the symbol magnitude increases, as is seen in Figure 2.8 where at the sample instant there is noticeable ISI only in the largest signal states. Observed against time, this looks like the "ringing" normally observed in an underdamped linear second order feedback system. As long as the natural frequency is significantly larger than the symbol rate the PRS filter shown in Figure 2.2 should smooth the ringing and make it of little concern. The main observation to be made here, however, is that the feedback does reduce the nonlinearity of the PA.

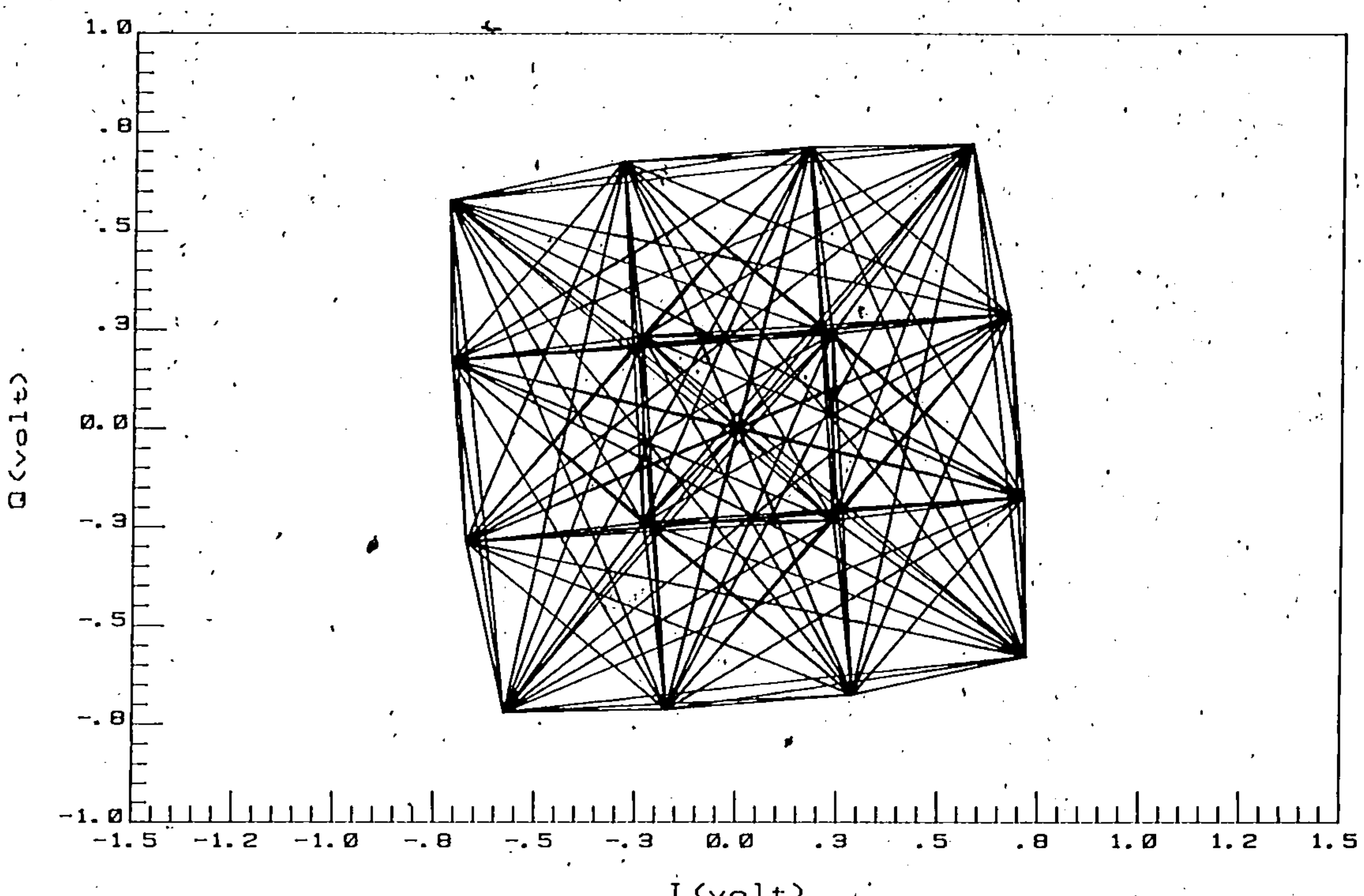

Figure 2.5 I-Q Response to a 256 Symbol Sequence Without Feedback at the 0.7dB Compression Point

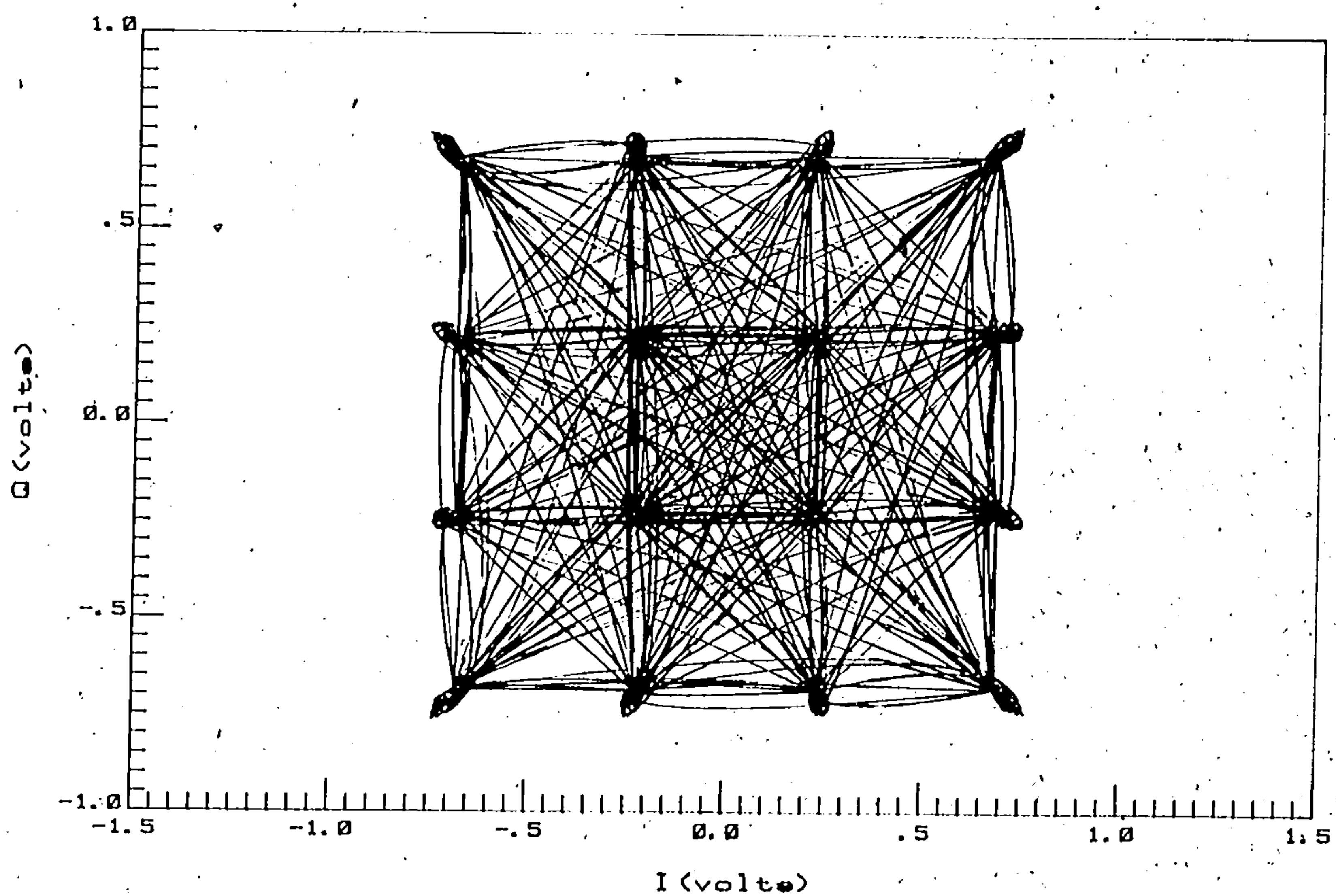

Figure 2.6 I-Q Response to a 256 Symbol Sequence With Feedback at the 0.7dB Compression Point

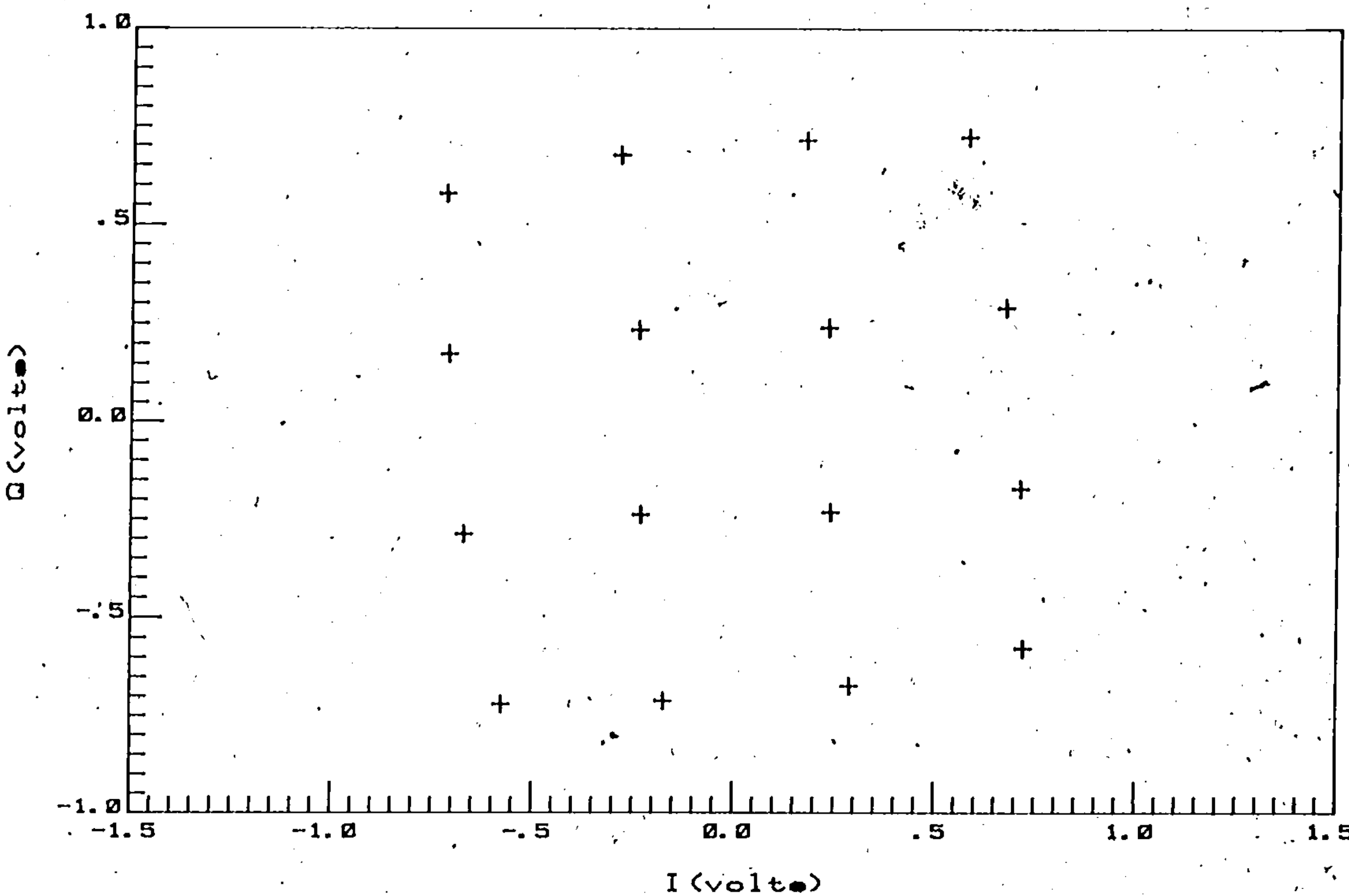

Figure 2.7 Sampled I-Q Response to a 256 Symbol Sequence Without Feedback at the 0.7dB Compression Point

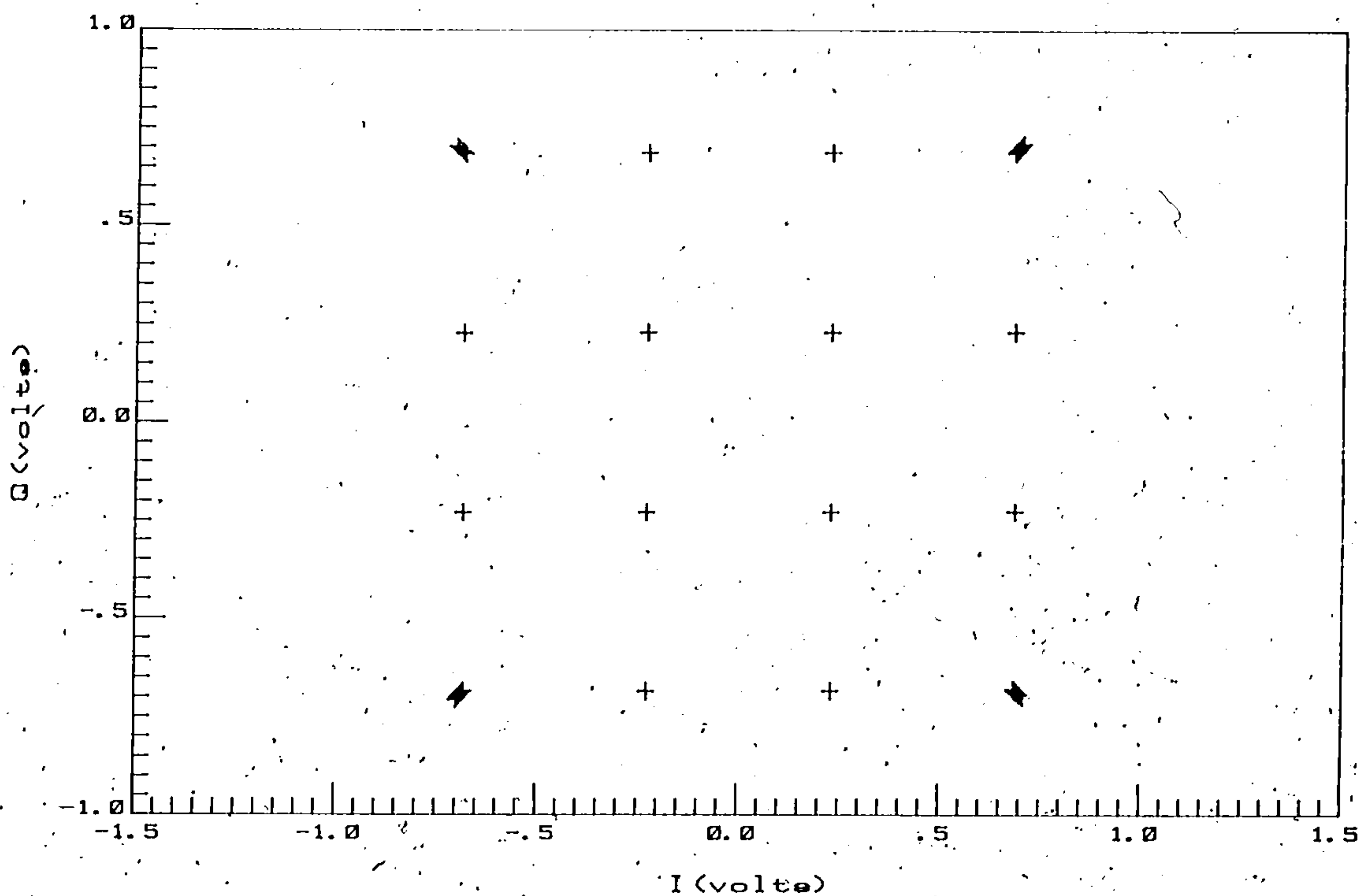

Figure 2.8 Sampled I-Q Response to a 256 Symbol Sequence With Feedback at the 0.7dB Compression Point

In order to quantify the improvement in performance, the peak eye closure is used (see Lucky, Salz and Weldon [52]) as a measure of performance. The peak eye closure at a particular sampling phase is defined as the maximum distance of perturbation of an ideal signal state toward any decision threshold, expressed as a fraction of the ideal distance. To do this the output was multiplied by a complex constant which minimized the mean square error between the input and output signals at the sampling instant over the data sequence, and then searched for the largest eye closure. Figure 2.9 shows the linear percentage peak eye closure versus input power for open loop, and 10 dB and 30 dB loop gains. Figure 2.10 shows the same results with logarithmic peak eye closure. The results in Figures 2.9 and 2.10 are all for loop bandwidths 3.3 times the symbol rate. Figure 2.11 shows some simulations at a lower loop bandwidth. By using feedback the peak eye closure due to the PA nonlinearity is reduced significantly. The peak eye closure is divided by approximately 10 and 40 for 10 dB and 30 dB loop gains respectively, when the PA input level (assuming ideal PA) is below the 0.7 dB compression point. Above the 0.7 dB compression point the 30 dB loop "crashes" while the 10 dB loop still maintains peak eye closure 5 times better than with no feedback.

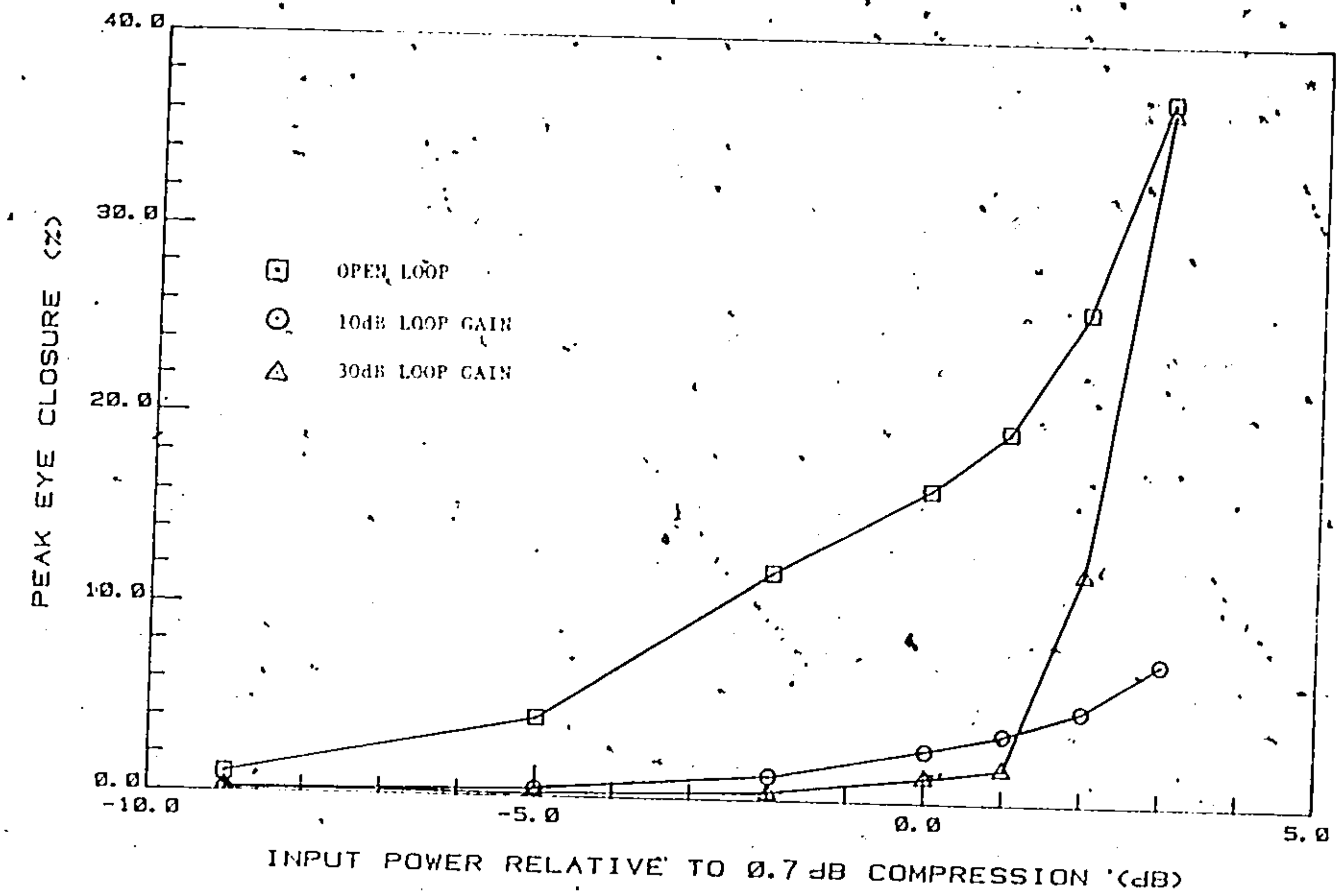

Figure 2.9 Peak Eye Closure versus Input Power for various Loop Gains

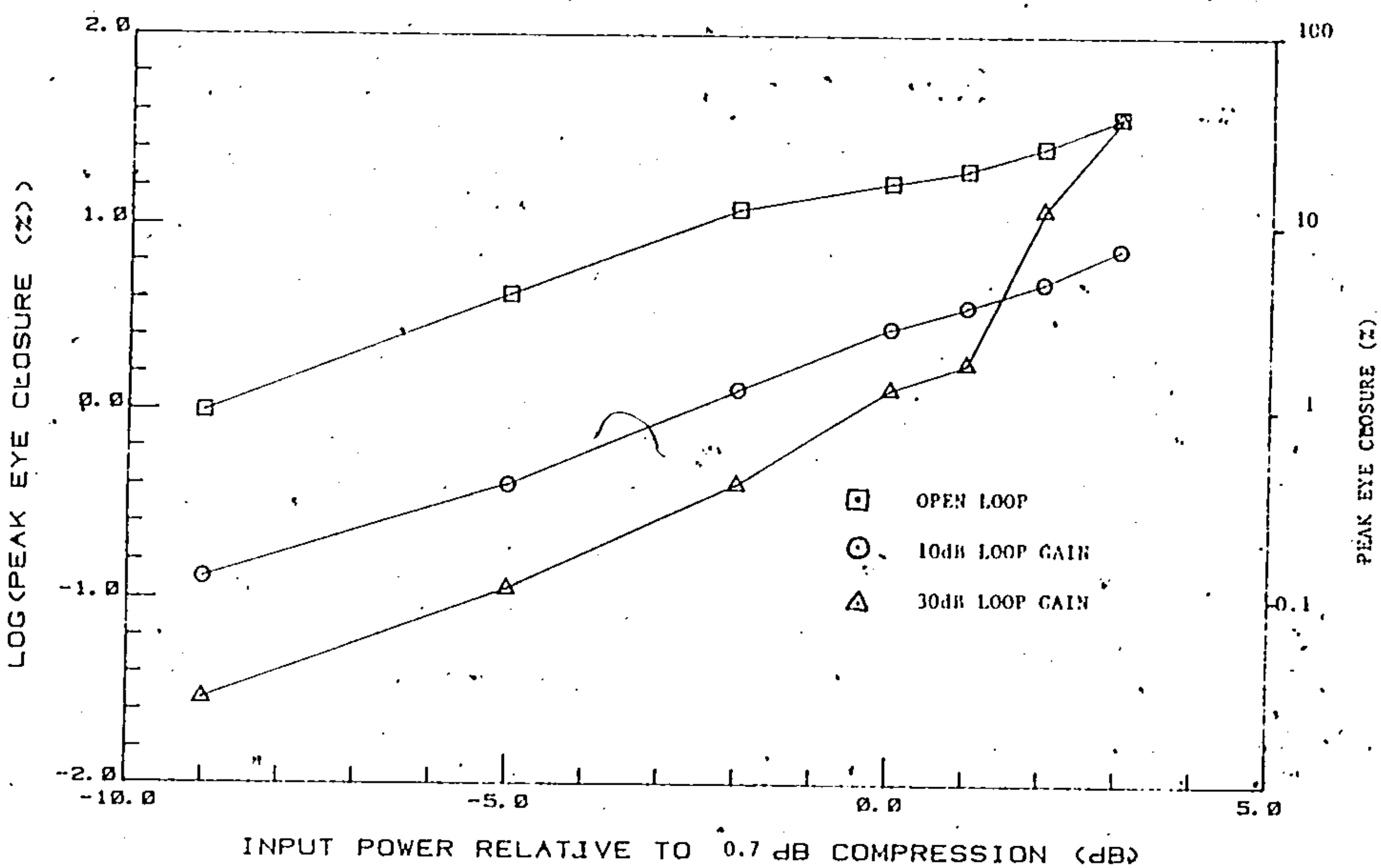

Figure 2.10 Logarithm of Peak Eye Closure versus Input Power for various Loop Gains

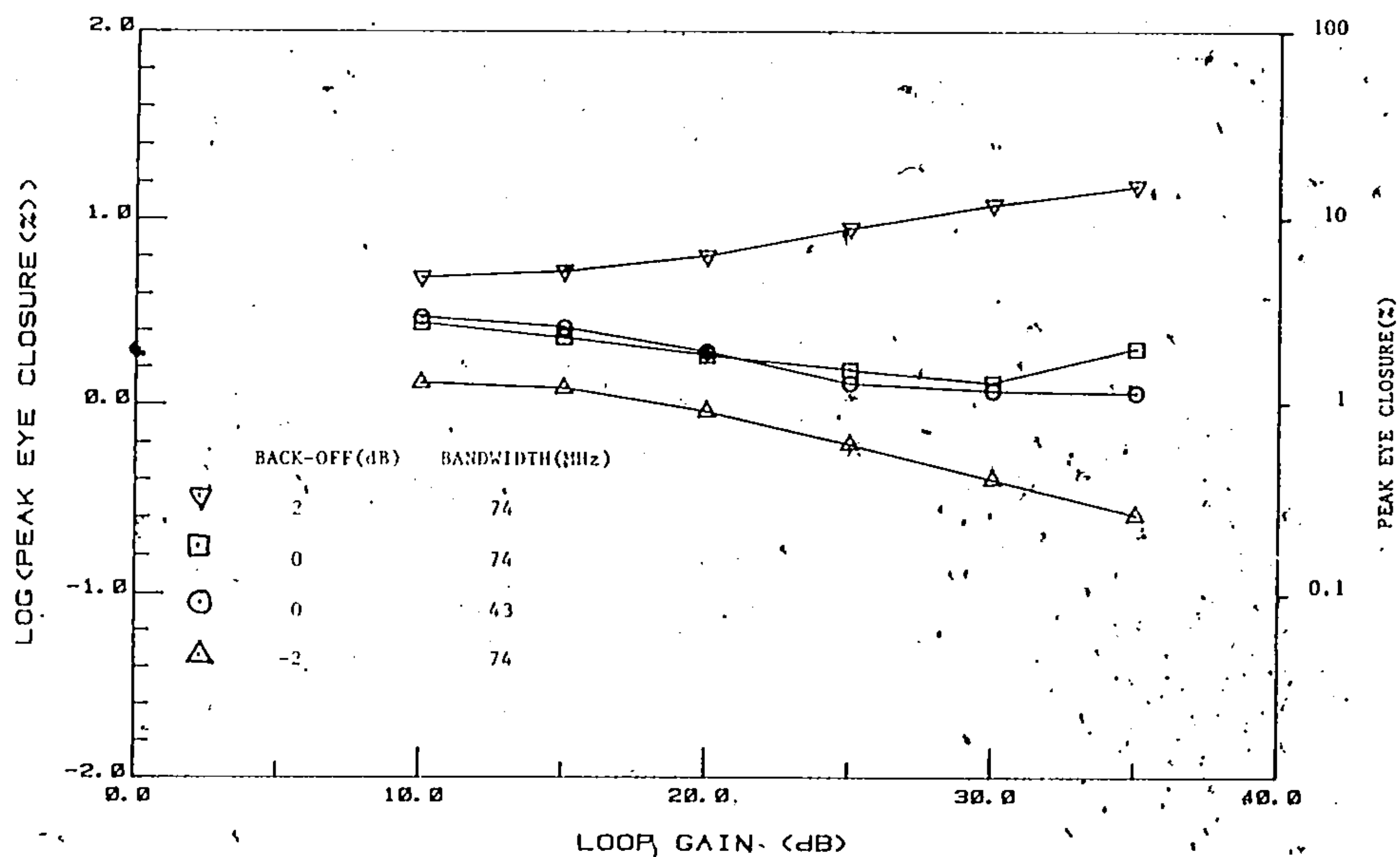

Figure 2.11 Logarithm of Peak Eye Closure versus Loop Gain

2.4 Implementation of the Feedback Linearized Transmitter

Figure 2.12 is the implemented version of the FLT. The implemented version is the same in function as the functional block diagram in Figure 2.2 except that the single cavity filter included in the functional block diagram is not implemented. As this first attempt at constructing the FLT is experimental, it was assembled using discrete connectorized components. Each block in Figure 2.12 represents a discrete SMA connectorized unit. All interconnections were done using semi-rigid coaxial cable. By using a discrete component realization, the physical size of the feedback loop was much larger than it could be, if it was constructed as one stripline or microstrip unit. The consequence of using discrete components is that the delay time for the loop was longer than desired. In addition, it was neccessary to use a second RF amplifier which had more gain than desired, and therefore, an attenuator was also required (10dB) to then reduce the gain. The resulting net loop delay time is 6.9 ns of which approximately half is due to the physical length of the loop.

This large loop delay limited the loop bandwidth to less than 30MHz and the loop gain to approximately 10dB to maintain loop stability. The schematic of the summer and compensation network is given in Figure 2.13. The matched pole-zero network in the compensation unit provides the

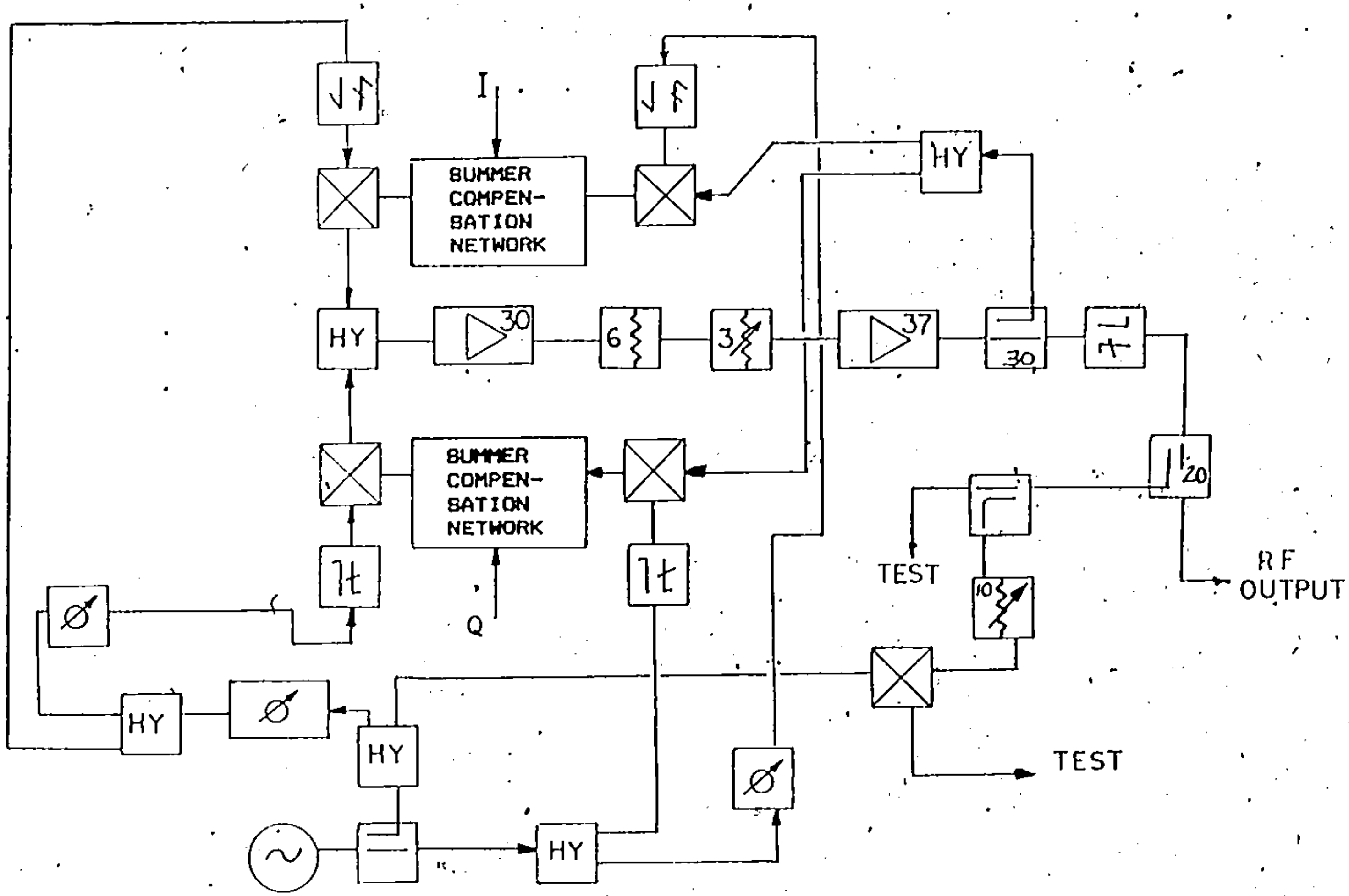

Figure 2.12 Implemented Feedback Linearized Transmitter Block Diagram

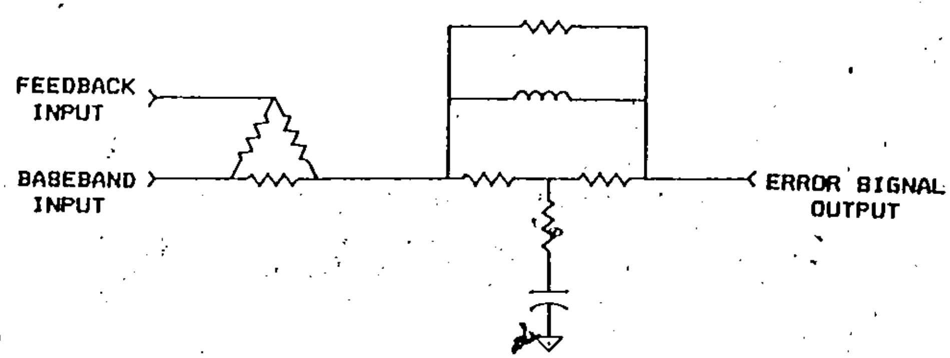

Figure 2.13 Compensation Network Schematic

transfer function of Equation (2.4) with the pole ω_b at a frequency of 6.3MHz and the zero ω_a at a frequency of 35MHz. The DC voltage offset network in the compensation network is set to minimize the unmodulated carrier oscillator component which escapes through the QAM modulator. Since the compensation network is not adjustable the 3dB variable attenuator seen in Figure 2.12 after the RF intermediate power amplifier (IPA) is used to adjust the loop gain between 9dB and 12dB. As loop gain is adjusted towards 12dB a large resonance peak in the frequency response of the loop begins to appear around 28MHz. As the loop gain is adjusted towards 9dB, the loop frequency response begins to drop significantly around 20MHz so the open loop gain was left set at 10dB as a best compromise.

2.5 Transmit Filter Design

The transmit RF filter has five separate functions. These functions are:

i) frequency domain multiplexing of the transmit signal with a number of other transmit signals;

ii) spectral containment to conform with government regulation;

iii) spectral containment to ensure that the adjacent channel interference is controlled to a sufficient degree;

iv) pulse shaping to minimize ISI;

v) matching of the transmit spectrum to the receiver amplitude response to maximize the receiver signal to noise ratio before detection.

The first requirement is fairly straightforward. It is easily achieved in all microwave radio systems by the fact that the microwave coupled cavity filters typically used will reflect other transmitted signals in the multiplex network back through a multiplexing circulator and on to the shared antenna system as seen in Figure 2.14.

All the other requirements are conflicting and an additional complication arises from the third requirement. It has been determined [19] that the most difficult situation with respect to adjacent channel interference is the case of a digital modulation interfering into an adjacent analog FM channel. It is outside the scope of this thesis to consider this case. It is mentioned here to emphasize the fact that meeting the second requirement stated above does not guarantee that the adjacent channel will not be degraded. This is especially important when outage performance under multipath conditions is considered. Adjacent channels operate on the opposite polarization (in the 4GHz band) and it has been observed [56,9] that the cross-polarization discrimination (XPD) of the antenna can be degraded during multipath conditions.

The other three requirements relating to the transmit filter were studied for this particular application

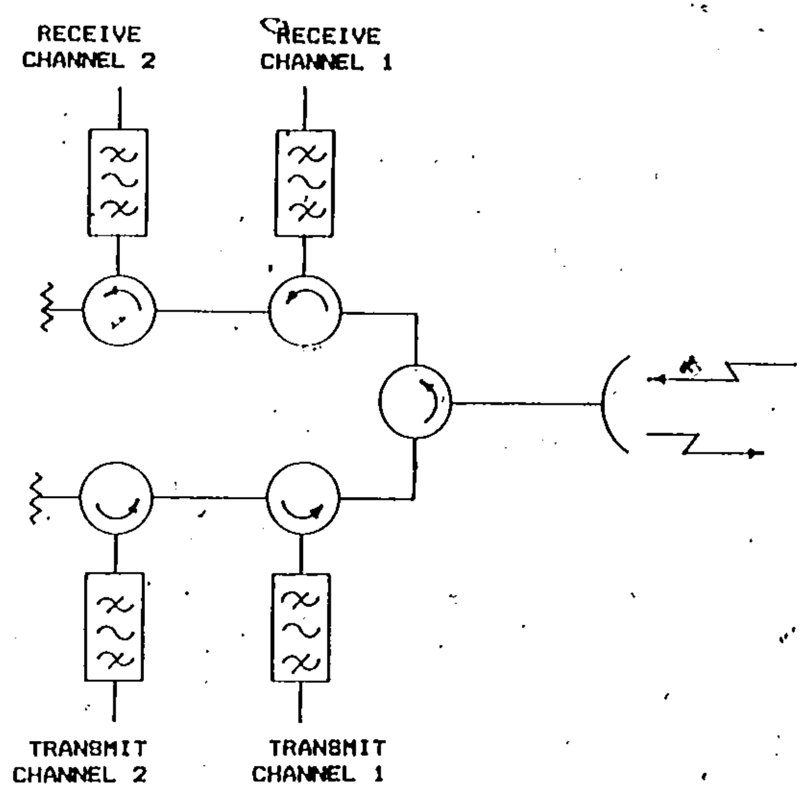

Figure 2.14 RF Multiplexing of Receiving and Transmitting Channels

by McMillen[57]. The fourth and fifth requirements above involve both the transmitter filter and the receiver filter. For 49QPR modulation at a data rate of 90Mbits/s, the ideal transmitter power spectrum, assuming matched filtering and zero ISI, occupies an RF bandwidth of 22.5MHz. This power spectrum does not fit within the FCC mask which we are using as a spectral emission limit. A solution to this difficulty is to overfilter the transmit spectrum to just meet the FCC mask and then filter the received signal to obtain a zero-ISI signal i.e. the desired QPR spectrum. This approach allows us to meet all the requirements except the noise matching one. McMillen has calculated the noise mismatch loss assuming that the receiver amplitude response is adjusted for zero-ISI and the transmit spectrum meets the FCC mask by 0.5dB at the band edge for various practical filters [57]. He also examined the interfering power in the desired channel due to an adjacent channel with the same transmitter for these same filters. His results show that the noise mismatch loss and the interfering power due to an adjacent channel vary insignificantly for four through to seven cavity Chebychev type filters that meet the FCC mask by 0.5dB. The transmit filter model selected was a Chebychev type bandpass filter with 5 poles, a 12.8MHz equal ripple bandwidth, and a .01dB ripple in the amplitude response. This was decided on the basis of the noise mismatch loss, the adjacent channel interfering power and the ease of realization of the transmit filter and the receiver amplitude response. For the case selected the mismatch loss was 0.6dB and the interfering power due to an adjacent channel with the same transmitter spectrum was -23dB relative to the desired channel received power. This amount of interfering power seems large, however, in any system application, the adjacent channel is using the opposite polarization, so that the total rejection of the adjacent channel is approximately 50dB.

The transmit filter assembly which included two waveguide circulators and the waveguide filter was constructed by Comdev Ltd.

2.6 Transmitter Interface Card

Figure 2.15 is a block diagram which shows the operation of the transmitter interface card. The interface card performs three functions which are:

i) conversion of one binary 90Mbit/s data stream into two quaternary 22.5Mbaud/s data streams;

ii) it provides a clock frequency reference of one part in 10^8 stability or accepts an external clock frequency reference;

iii) it provides differential encoding so that phase ambiguities in the receiver may be resolved.

Because of the four-way symmetry of the 49QPRS signal space and the 16QAM signal space, the receiver cannot distinguish between the correct one out of four phases. This problem exists in any two-dimensional signal set with 4-quadrant symmetry[58]. One solution to this problem is to use differential encoding to remove this ambiguity. With 16QAM the differential encoding only needs to be applied to the most significant in-phase (I) bit and the most significant quadrature-phase (Q) bit and this is enough to determine the phase or quadrant of the signal. The remaining bits are Gray coded within each quadrant. This method of coding the data to remove phase ambiguity without unnecessarily increasing the error rate due to differential encoding of other than the most significant I and Q bits was suggested by Weber [58]. This encoding method is implemented in the interface card using a PROM look-up table method. The PROM used is the 256x4 ECL MCM10149.

The remainder of the interface unit is relatively straight forward. The 90MHz clock oscillator was supplied by Vectron Laboratories Inc. and the digital to analog (D/A) convertor used was an MC10318 which had about an 8ns rise time. Rise time is more important for the D/A than settling time because of the amount of filtering done by the transmit filter and other filters in the system. The other functions were performed by standard ECL series devices.

Figure 2.16 is a schematic showing the D/A output portion of the interface card. It is seen that the D/A output to the FLT portion of the transmitter is alternating current (AC) coupled. This capacitor is chosen so that the power of the blocked low frequency component is more than 60dB below the total power in the signal.

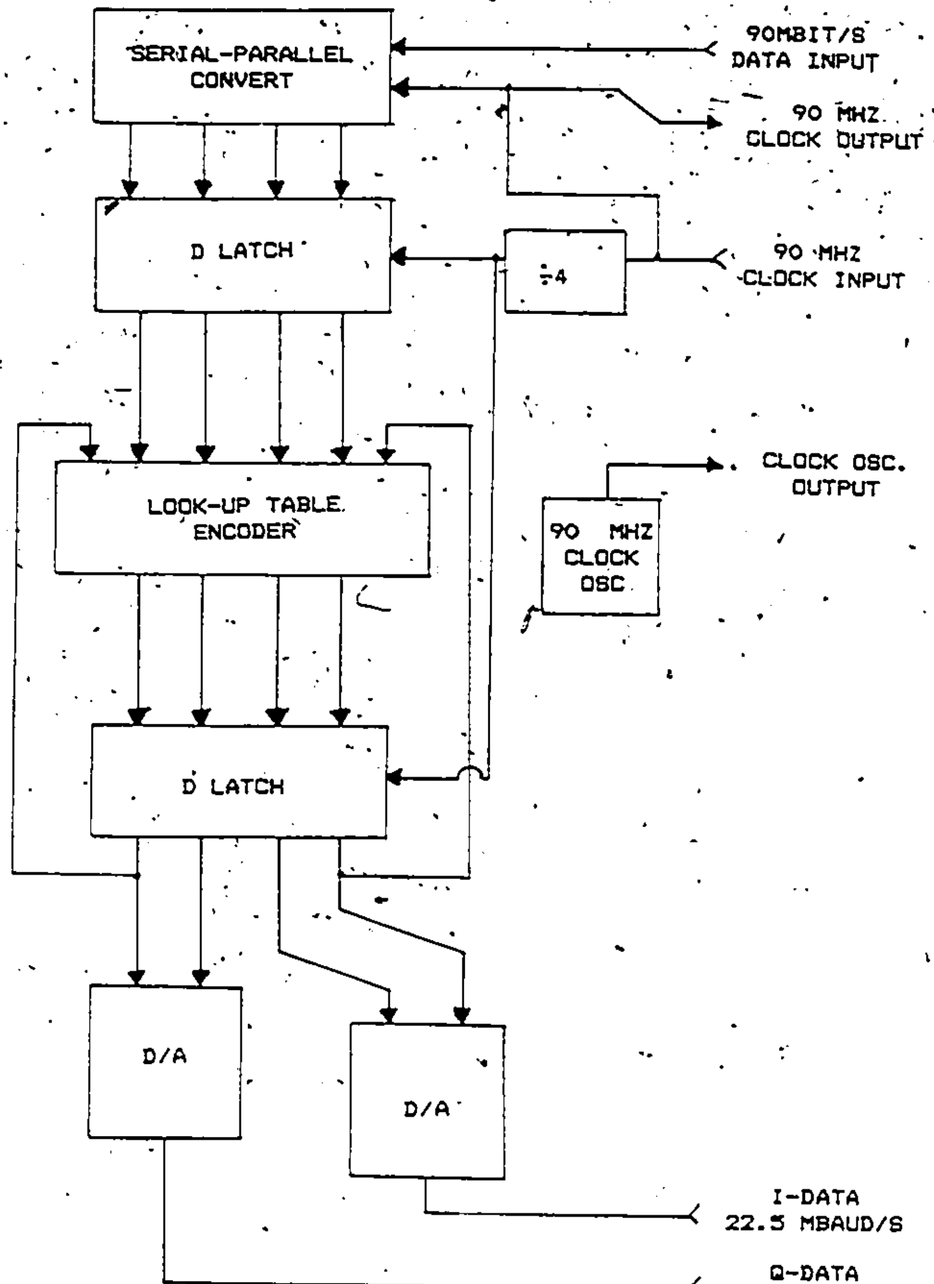

Figure 2.15 Data Encoder Block Diagram

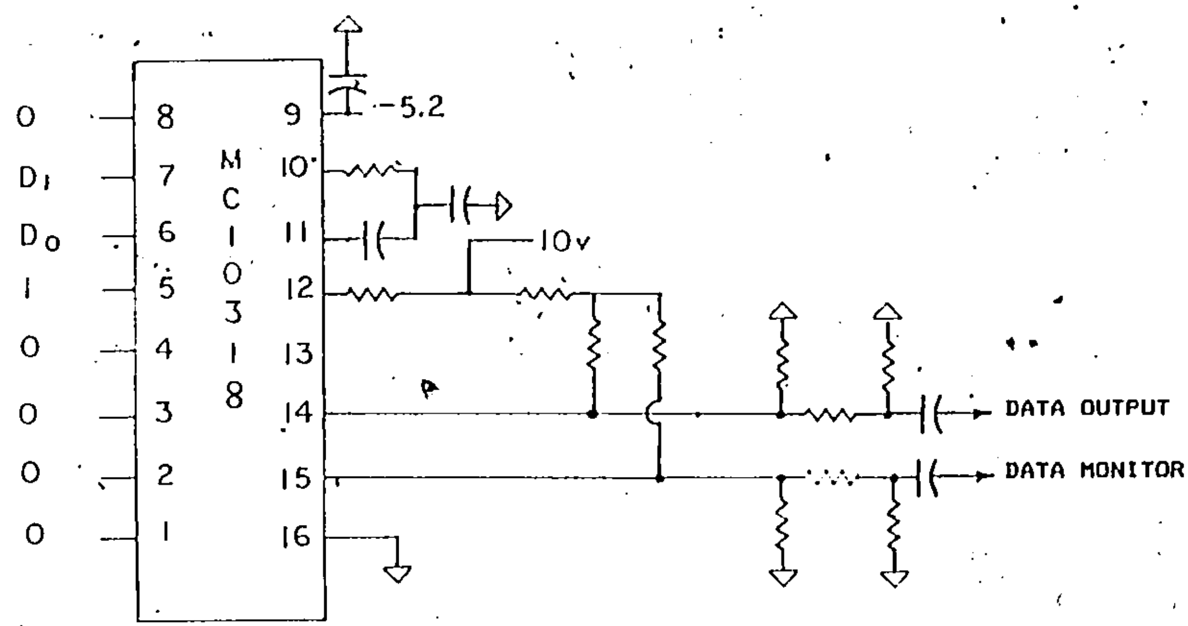

Figure 2.16 Multilevel Modulator Partial Schematic

CHAPTER 3

IMPLEMENTATION OF THE 49QPRS RECEIVER

3.1 Introduction

In Figure 3.1 the receiver block diagram is given. The RF filter, the RF amplifier, the downconverter, the IF filter, and the IF AGC amplifier are all typical of recent microwave radios with the exception being that there are no phase equalizers included anywhere in these components. Since there is nothing new in these components and since they were obtained from outside the university, little attention will be given to their design. The remainder of the receiver system was designed and built as part of the work of this thesis. The bandpass IF transversal filter is intended to equalize most of the linear amplitude and phase distortion due to the various components of the radio equipment while the adaptive DFE is intended to equalize the small amount of residual equipment distortion, and of course, the time varying distortion due to the multipath channel.

The bandpass transversal filter is implemented in modular form with one complex tap per module so that taps may be easily added or taken away as required for experimental purposes. The DFE is implemented using five synchronous complex forward taps and five complex backward taps. As is noted in Chapter 1, five taps are used in both directions so that a 40dB notch [30] due to multipath fading may be equalized for high SNR's. Also, it is anticipated that in the microwave fading environment an infinite notch can be equalized with this structure.

Before outlining the organization of this chapter a few of the salient features of the DFE will be described. A block diagram of the DFE is shown in Figure 3.4 and the associated synchronization circuitry is shown in Figure 3.13. The DFE's tap-weights and the sampling phase are adjusted to minimize the peak error distortion and the mean square error distortion respectively. The equalizer tap-weights are adjusted digitally using the up-down counter method of Lucky [39] in a decision-directed mode. The sampling phase is also adjusted digitally by the same up-down counter method, but according to the product of the slope of the unsampled equalized data with the decision error, as suggested by Chang[41] and Kobyashi[42]. Both the tap-weights and the timing phase are adjusted according to information obtained from the received signal in every symbol interval, that is every 44ns. In addition to adaptation of the tap-weights and timing phase, the DC value at the quantizer inputs is adaptively adjusted to maintain the summation of the estimation errors at zero. This is also done using Lucky's up-down counter method. One last feature

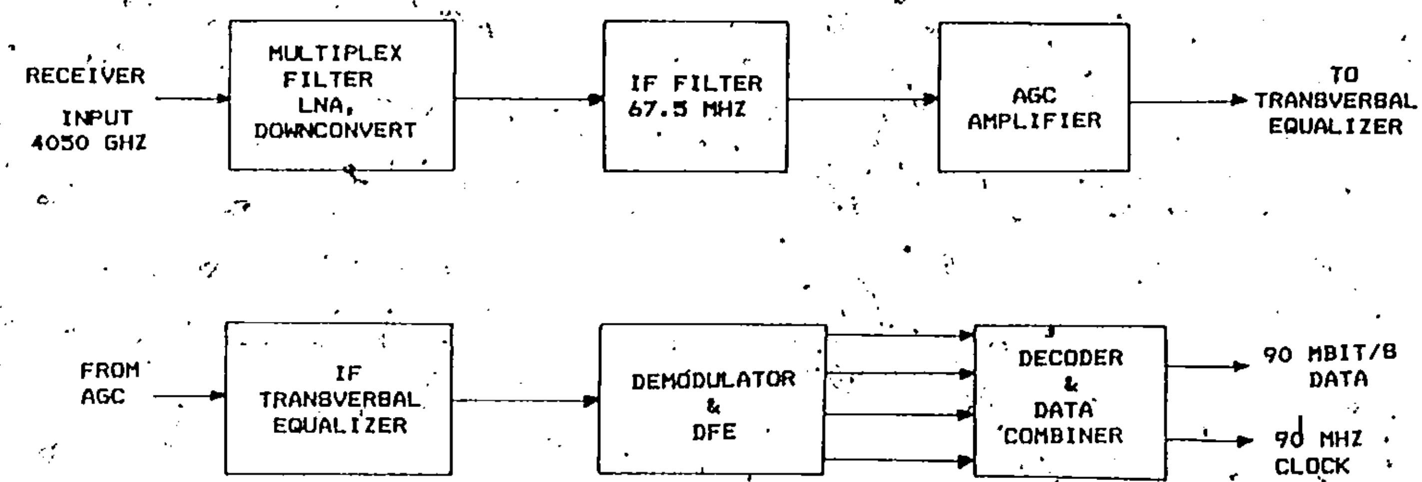

Figure 3.1 Receiver Subsystems

to be mentioned here is the fact that the on-axis and cross-axis tap-weights affecting one axis are adjusted separately from the on-axis and cross-axis tap-weights affecting the other axis, so that a total of 40 tap-weights are being adjusted. In this chapter all references to tap-weights are real valued tap-weights, and an "on-axis" tap-weight refers to the real part of the complex tap-weight used in Chapter 4, and a "cross-axis" tap-weight refers to the imaginary part of the complex tap-weight used in Chapter 4.

In Section 3.2 the first part of the receiver up to the output of the IF AGC amplifier is described. In Section 3.3 the bandpass transversal equalizer and demodulator are described. In Section 3.4 the implementation of the forward equalizer (FE) and backward equalizer (BE) tap-weights and the quantizers are described without concern for the adaptation of the equalizer tap-weights or carrier and clock recovery. In Section 3.5, 3.6, 3.7, and 3.8 the parameter adaptation, sampling phase estimation, carrier phase estimation and differential decoding are described. In Sections 3.4, 3.5, and 3.6 special attention is given to rationales for the design alternatives selected.

3.2 Receiver Front End Implementation

The RF filter, RF AGC amplifier, and downconvertor are constructed as one unit and were obtained from Raytheon

Canada Ltd. The RF filter is a low insertion loss five cavity waveguide filter and contributes little to the in-band frequency response and to the signal pulse shaping. Its main purpose is RF multiplexing and rejection of the receiver image frequency, etc., since it is a super-heterodyne receiver. The RF AGC pre-amplifier provides the receiver with a noise figure of 3.5dB. It has an AGC included mainly to protect against up-fading (increases in receive signal level due to constructive interference of the multipath) which could drive the RF preamplifier into saturation. The downconverter, converts the 4050 GHz received signal to an IF frequency of 67.5MHz. This frequency is non-standard and was chosen because it was the third harmonic of the symbol clock rate which would allow tap-weight adaptation of the IF bandpass transversal equalizer without the complication of having to resolve the on-axis and cross-axis tap-weights with respect to a different phase for each tap of the bandpass transversal equalizer.

The IF filter was not phase equalized, as stated in the introduction. This filter was built by Allen Avionics Inc. The purpose of this filter is to provide rejection of the adjacent channel, and to provide an approximate noise match to the transmitted signal when there is no multipath. As was stated, in discussion of the transmitter filter design, the noise mismatch loss even when the receiver response is designed for zero ISI is only 0.6dB so that by choosing the 3dB bandwidth of this filter to be slightly larger than the transmitted signal's 3dB bandwidth and approximately equal to the zero ISI receive filter 3dB bandwidth the noise mismatch should be approximately 0.6dB and the remaining ISI due to the equipment and not the multipath is left to be equalized by the bandpass transversal equalizer. The measured amplitude response of the filter is shown in Figure 3.2.

The IF AGC amplifier which was obtained from Watkins-Johnson Co. has a 55dB AGC range. It was modified to operate at an output power of -3dBm to obtain better linearity. Its normal output power was 7.5 dBm.

3.3 Bandpass Transversal Equalizer Implementation

A block diagram of the bandpass transversal equalizer is provided in Figure 3.3. The symbol period delay elements were realized by using coaxial cable sections. In order to provide isolation and to maintain signal levels at each tap, integrated circuit amplifiers of about 10dB gain were used with each delay element. The complex tap-weight multipliers were realized by splitting the signal into quadrature components and multiplying using two DC controlled double balanced mixers which are designed specifically for gain control applications. The mixer

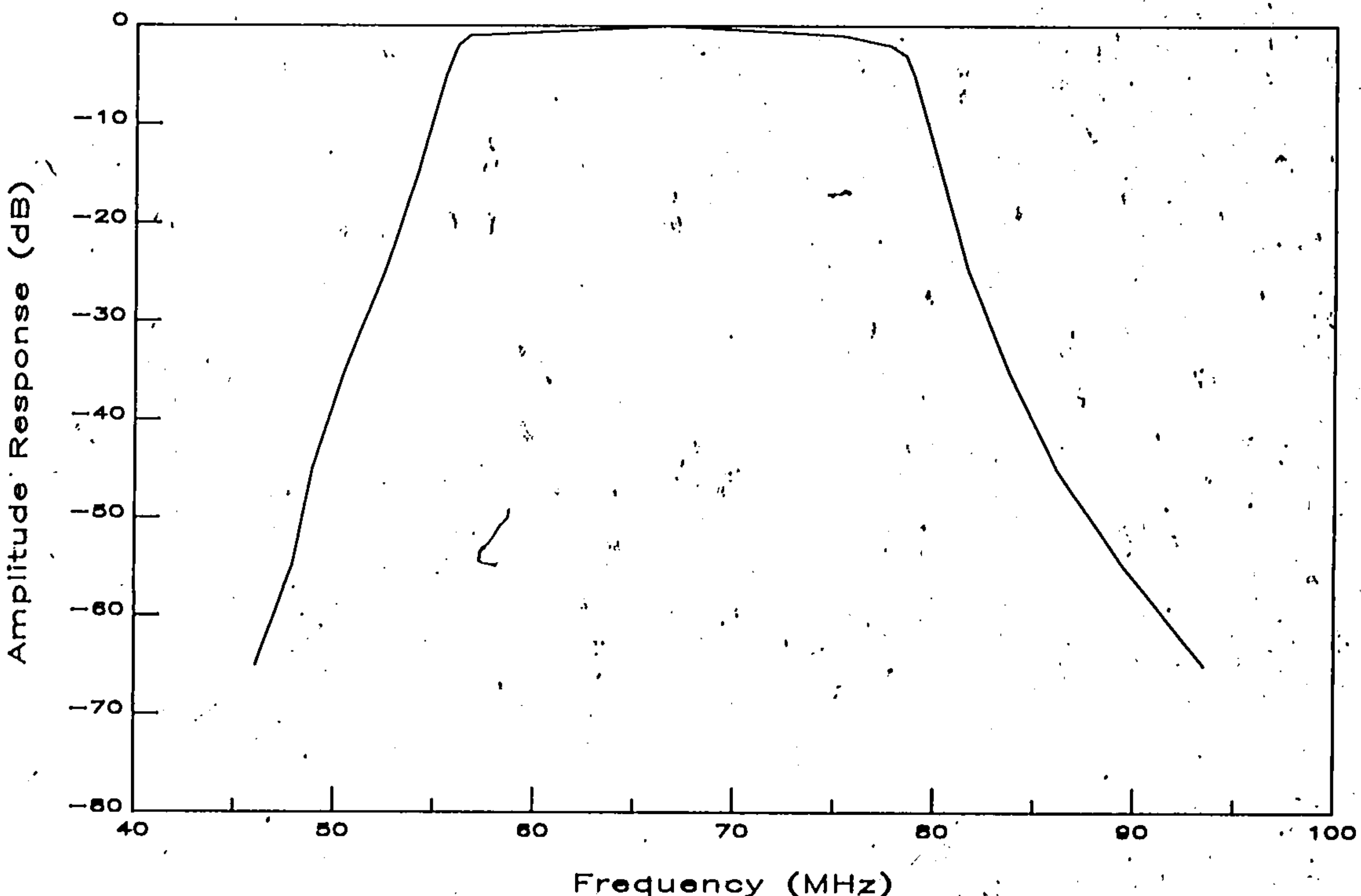

Figure 3.2 Measured IF Filter Amplitude versus Frequency Response

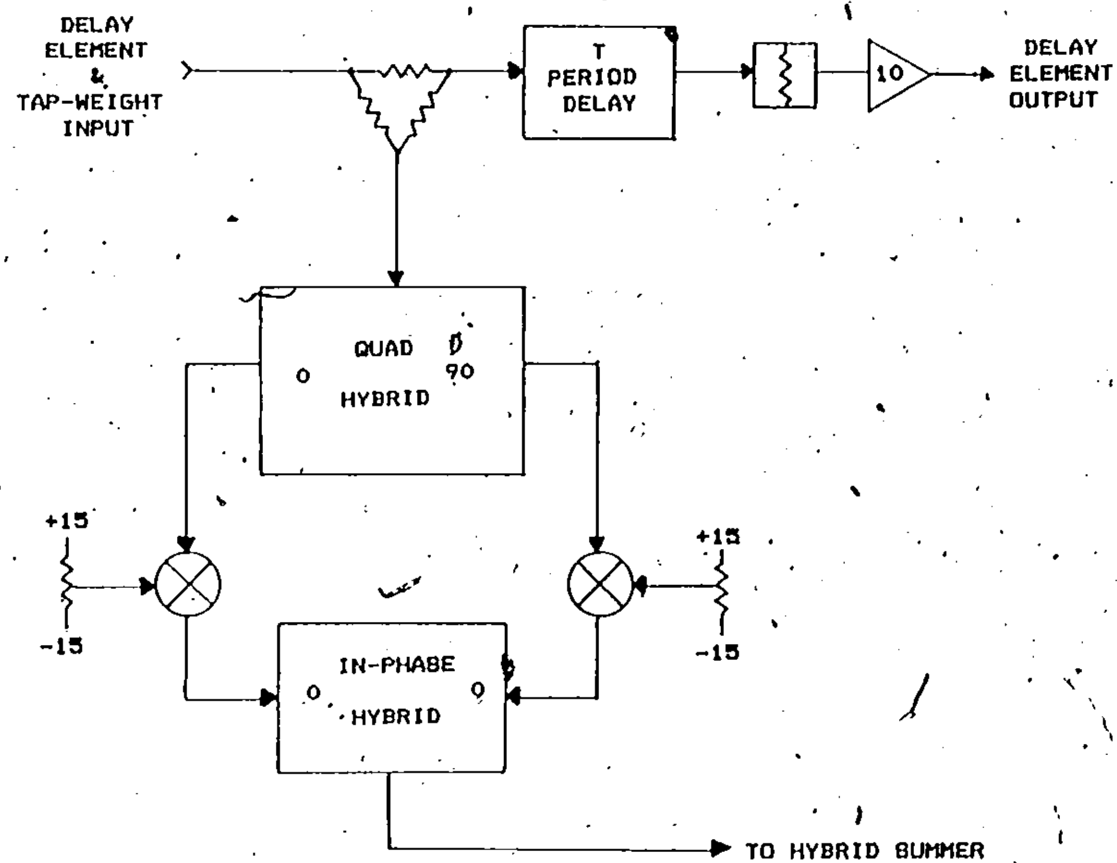

Figure 3.3 Diagram of Tap-Weight Multiplier and Delay Element of the IF Transversal Equalizer

outputs are summed and amplified to provide an adequate power level for the demodulator. The mixer attenuators can also be controlled by an external DC voltage but no use was made of this. Two delay elements and complex tap-weights are built per circuit card so that taps could be added as desired.

3.4 Demodulator, Forward, and Backward Equalizer Implemention

The IF received signal enters the demodulator after having passed through a fixed matched filter(matched to transmitter spectrum), an AGC amplifier and a manually adjustable transversal equalizer. High level mixers used for demodulation are operated more than 10dB below their 1dB compression point to make nonlinear distortion insignificant. A quadrature hybrid which provides coherent frequency references for the mixers is not critical in its phase balance since in the DFE the tap-weights affecting the I-axis and the tap-weights affecting Q-axis operate independently and will correct any phase imbalance in the demodulated signal of less than 10 degrees without significant noise penalty. After demodulation, low pass filters are included only for removal of carrier feedthrough and unwanted mixer products.

A functional block diagram showing the FE structure with two of the five taps , the BE structure with two of the five taps, and the quantizer is given in Figure 3.4. The demodulated 49QPRS signals at the forward equalizer (FE) inputs have a 99% power bandwidth of approximately 11 MHz, a symbol period of 44.4 ns and 7 amplitude levels. Since the partial response signals are confined to the Nyquist bandwidth and since the sampling phase is adjusted to minimize the MSE, fractional tap spacing is not considered and the FE taps are spaced at 44.4 ns intervals. The FE is an analog continuous time implementation. The main reason for being analog is due to the backward equalizer (BE). The delay in the feedback loop has to be less than the 44.4 ns symbol period and the add time for a five tap summation using MSI ECL takes too much of that time to keep the total loop delay under the symbol period. This limitation will likely exist for DFE's with three or more backward taps until suitable LSI GaAs devices become available. To continue with the FE description, the delay elements are realized by the use of miniature 100 ohm transmission lines which are wound inside an epoxy encapsulated cylinder and are printed circuit board (PCB) mountable. The tap delays are realized by using nominal delay elements of 40ns and 5ns and selecting values to get within 0.5ns of 44.4ns. Since all the delay elements for the FE are connected directly without buffering it is critical in attaching the

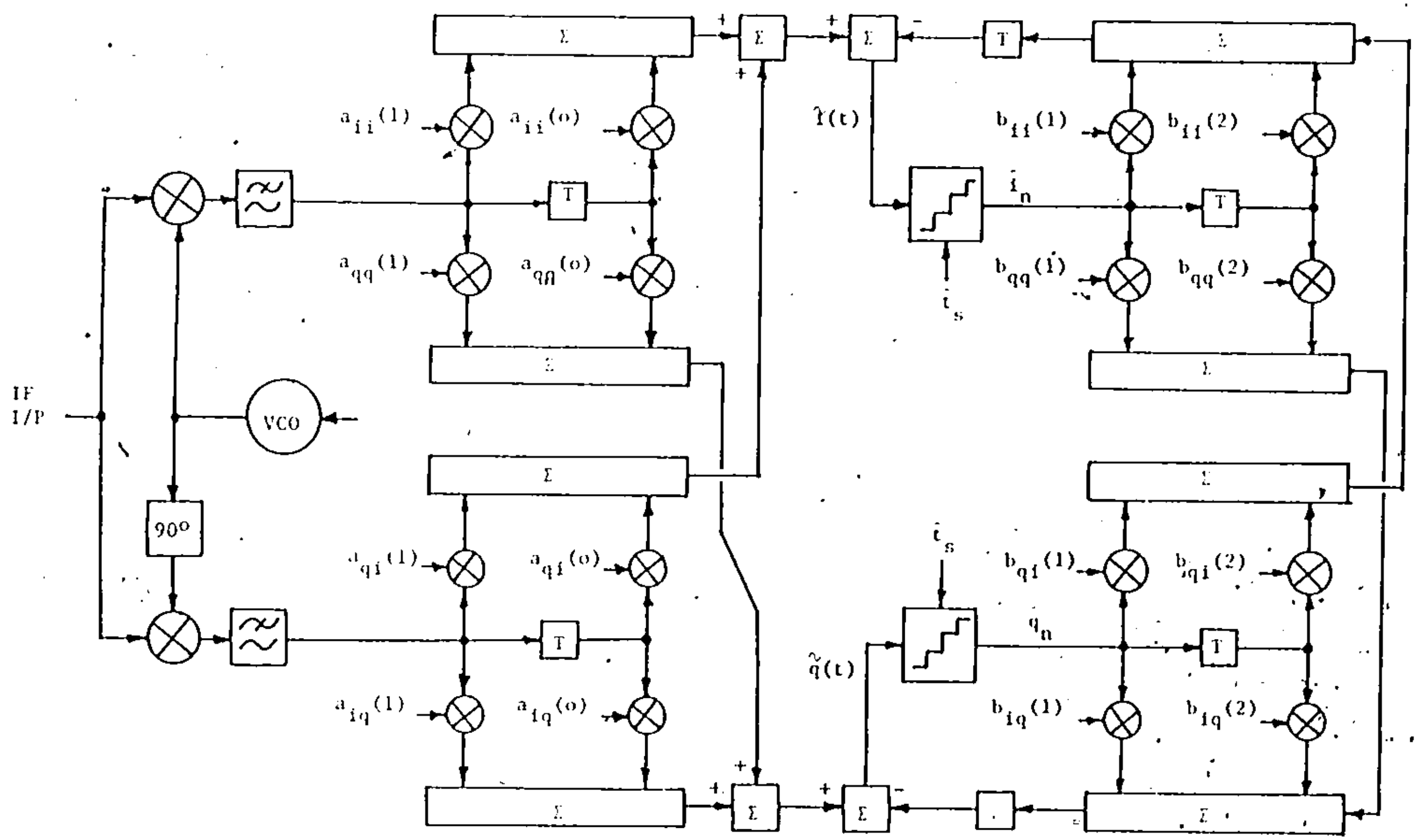

Figure 3.4 Functional Diagram Two Forward and Two Backward Taps of the DFE

multipliers and in terminating the ends of the transmission line not to cause any mismatches. Echoes formed over three quarters or more of the total line length would be outside the range of the DFE and hence could not be equalized by the DFE. The input return loss to the delay line structure was better than 27dB up to 11.25MHz. Single chip linear four quadrant multipliers are used for tap-weight multiplication. Figure 3.5 has a partial schematic of one of the tap-weight multipliers. The coupling capacitor at the multiplier output is chosen so that the power of the blocked low frequency signal is more than 60dB below the total power in the signal. The summing of multiplier outputs is done by passive resistor networks and the resulting signal loss is made up with single chip differential amplifiers. This combining network and amplifier schematic are shown in Figure 3.5. Generally, throughout the DFE, differential inputs and outputs are used to minimize distortion and interference from other signals. A photograph of the circuit board containing the FE is shown in Figure 3.8.

The output of the backward equalizer (BE) is combined with the seven level FE output to produce a four level signal at the quantizer circuit input. As shown in Figures 3.5 and 3.7, the FE and BE outputs are both summations of the in-axis and cross-axis tap-weights. Quantizing and sampling are performed by a four bit A/D converter which is capable of 100 megasample/s rate. A differential amplifier

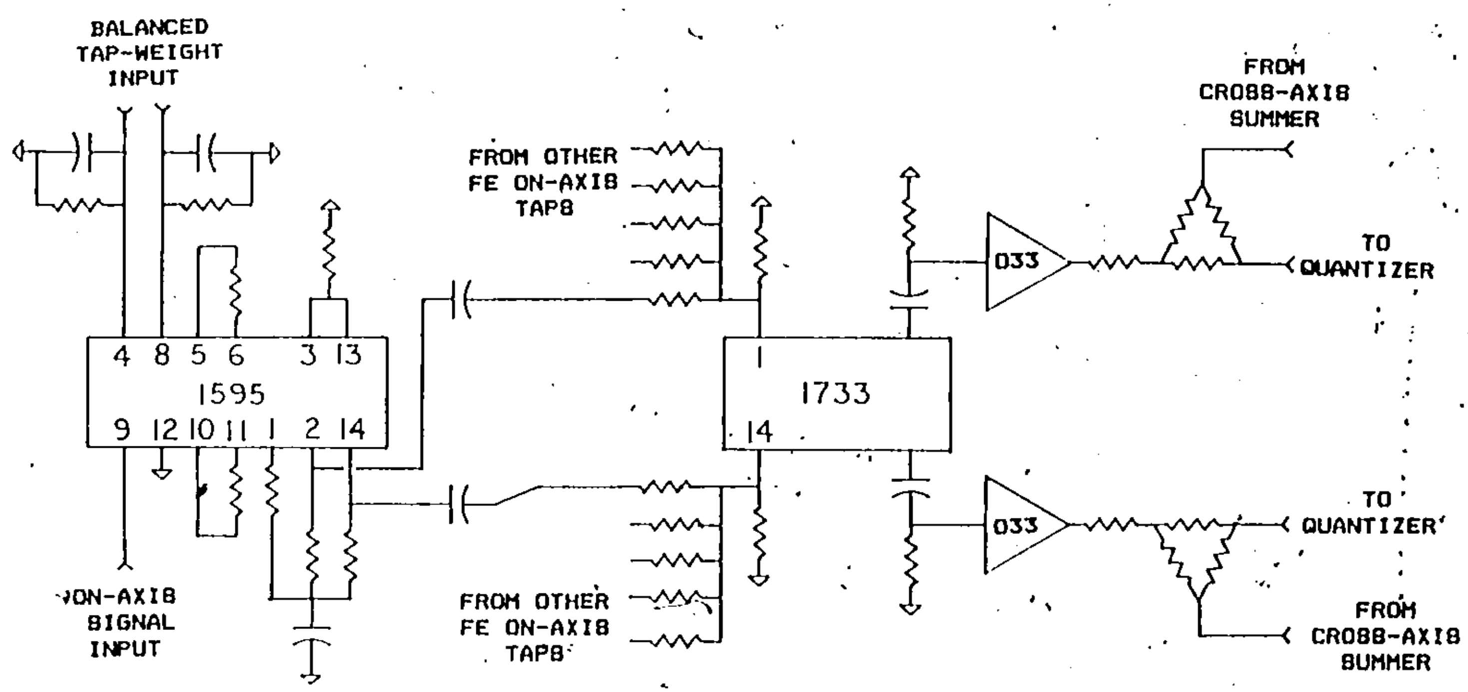

Figure 3.5 Forward Equalizer Tap-Weight Multiplier and Summer Partial Schematic

with a 3dB bandwidth of 90MHz is used preceding the quantizer to obtain a suitable signal amplitude at the quantizer input. The high bandwidth is necessary to obtain a small enough delay time for the feedback data. A schematic of the summer, make-up amplifier and the quantizer is given in Figure 3.6. The two most significant bits represent the decided symbol while the third and fourth most significant bits are the sign and magnitude of the difference between the decided symbol and the equalized symbol.

Several methods of implementing the backward equalizer were considered. As discussed earlier, the propagation delay of the quantizer, the BE, and the summer must be less than the symbol period of 44.4 ns in order that the previous decisions will be available in time at the quantizer input. (The delay element in the feedback path of Figure 3.4 has a delay which is less than 44.4 ns by the amount of the inherent circuit propagation delay in the feedback path.) As stated earlier, the delay requirement made a digital implementation impossible using ECL logic. The main bottleneck in a digital implementation is the summation of the output of ten on-axis and cross-axis tap-weights. Even with the maximum degree of parallelism and pipelining, the four levels of addition necessary to add 10 tap-weight outputs would take almost the whole 44.4ns of the maximum delay time allowed. The remaining alternatives were two. First, a digital to analog converter (D/A) could be used

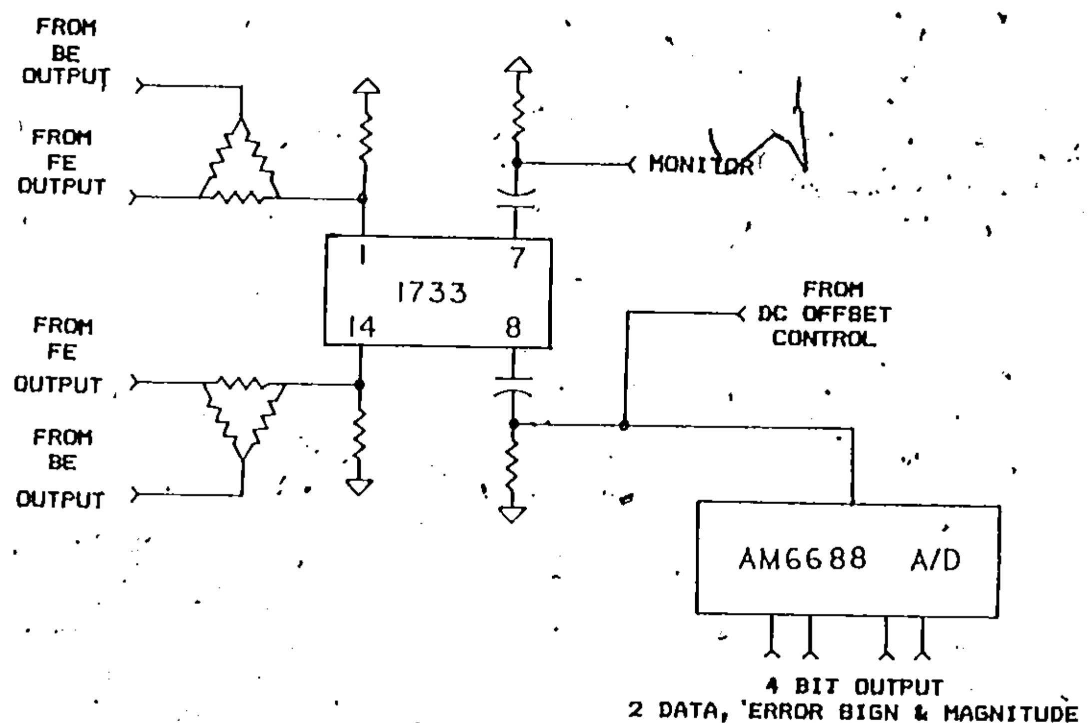

Figure 3.6 Quantizer Input Interface Partial Schematic

immediately after the quantizer and then the FE structure could be used for the backward equalizer (BE). Second, the digital output of the quantizer could be passed through a shift register (to provide the necessary delays) and the tap-weights could be implemented as multiplying D/A's. The first method is less costly since four quadrant multiplying D/A's at this speed are more than four times the cost of the analog four quadrant multipliers used, however, the second method is used because the margin on the delay time requirement is much better. The four quadrant multiplying D/A's are constructed by using two fast D/A's with 10 ns conversion time and one low cost, low speed 8 bit D/A. Figure 3.7 is a schematic of the multiplying D/A used to perform the backward tap-weight multiplication. The low speed D/A converts the tap-weight value which is in 8 bit digital form to two complimentary current sources which are used as the reference currents for the two high speed D/A's. The high speed D/A's each convert the two bit decided symbol values to analog form. By subtracting the two D/A analog outputs, the DC components due to the digital inputs are both removed. This removal of the DC component is important, since the DC component varies from symbol to symbol and the only other way to remove it would be with an op amp which also would have too long a delay time. The outputs of the multiplying D/A's are combined using a resistive combiner, just as in the FE, since again, that is the only way to do

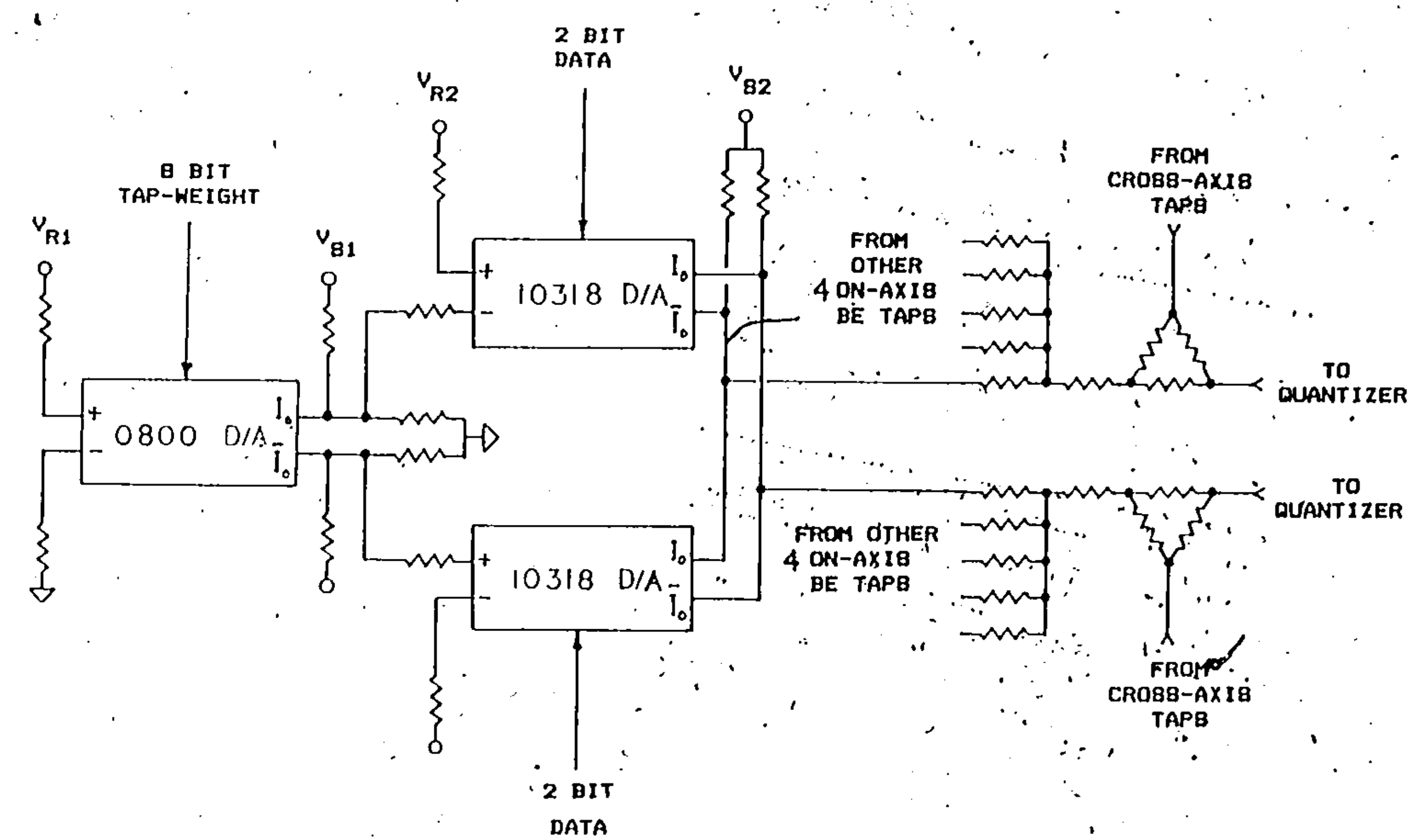

Figure 3.7 Backward Equalizer Tap-Weight Multiplier and Summer Partial Schematic

the summation in a short enough period of time. The total decision feedback loop delay obtained was approximately 27ns. The quantizer A/D took 6ns, the tap-weight multiplier took 8ns, the make-up amplifier driving the quantizer A/D took 8ns, and the physical length of the loop caused 5ns of delay.

The portion of the DFE described so far (shown in Figure 3.4) is contained on six S100 (130mm by 254mm) sized PCB's and one 120mm by 160mm PCB. The smaller board contains the demodulator and low pass filters but not the carrier oscillator. Two S100 sized boards (shown in Figure 3.8) are used for the forward equalizer, two (shown in Figure 3.8) are used for the backward equalizer tap-weights (the multiplying D/A's), and two (shown in Figure 3.8) are used for the quantizers and backward equalizer shift registers. These last two also contain all the gradient calculations for the forward and backward tap-weights and for the clock and carrier recovery loops to be discussed in the next two sections.

3.5 Tap-Weight Adaptation

Adaptive algorithms which have been developed for the adjustment of tap-weights are usually analysed with respect to stationary received data. However, if the rate of change of the channel due to multipath is very slow compared with the symbol rate of the system, then the adaptive

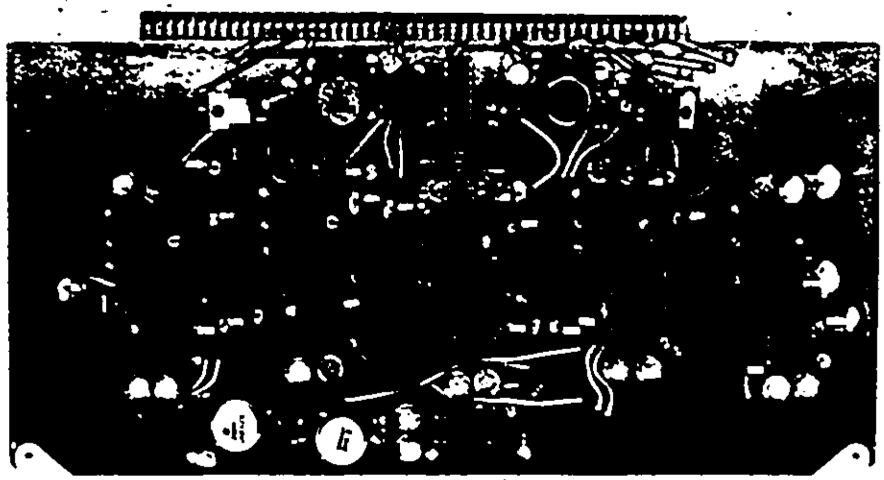

a) Forward Equalizer

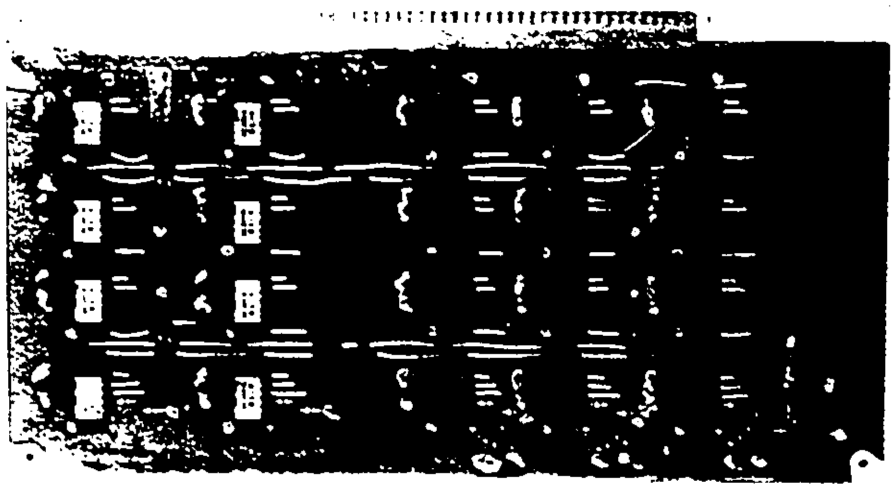

b) Backward Equalizer

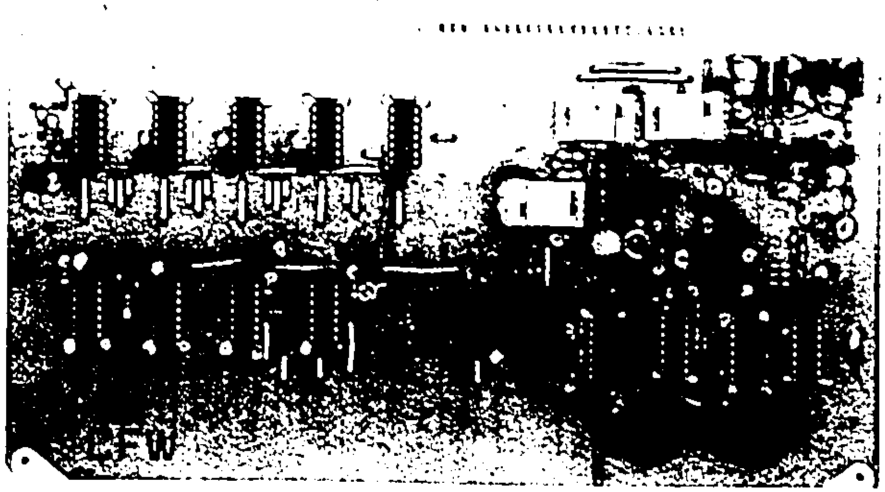

c) Quantizer, Shift Register, Gradient Calculation

Figure 3.8 Photographs of Forward Equalizer, Backward Equalizer, and Quantizer Printed Circuit Boards algorithm can track or "learn" the changing channel characteristics as time progresses. Bello[69] has characterized fading channels by their delay spread and their Doppler spread. Monsen has described the "learning constraint" for a fading channel as follows: In order to successfully track the changing channel conditions, the data symbol rate should be much greater than the Doppler frequency spread due to the multipath. The Doppler frequency spread due to the multipath in a microwave channel has been determined to be in the order of one Hertz[69]. Since the symbol rate of this system is 22.5 MHz the data symbol rate exceeds the Doppler spread by 10^7 times, and there is much more than adequate time to track the changing conditions. This surplus in tracking capability can be used to advantage, by trading off some of the potential tracking speed for a reduced complexity adaptation algorithm. This is important, since with a symbol period of 44.4ns there isn't much time for any degree of complexity at all.

Three different algorithms were considered for adaptation of the tap-weights. These were the Least Mean Squares (LMS), a decision-directed zero forcing (ZF) of Lucky[39] and George, Bowen, and Storey[38] and a modified zero forcing (MZF) of Hirsch and Wolf[70]. The ZF algorithm was invented by Lucky [39], but George et al. [38] were the first to apply it to a DFE. The LMS algorithm is feasible, however, it adds an extra degree of complexity in the area of the FE taps and it would be necessary to use an analog implementation of the algorithm. Lucky's method, to be considered, is the one bit quantized gradient method that is decision-directed and that uses binary up-down counters to accumulate the one bit gradient estimates before adjusting the tap-weight. This method offers extremely simple gradient estimation and the possibility of all digital implementation of the tap-weight adaptation, although the accumulators are more complex than an analog integrator when MSI TTL is used. Hirsch and Wolf considered Lucky's method (the one under consideration here) and found it to be unsatisfactory in their application of a linear equalizer to vestigal sideband data transmision over telephone channels[70]. They derived a modified zero forcing (MZF) algorithm which worked well. Their MZF algorithm could also be viewed as a modified LMS in that it could be obtained from an LMS algorithm by simply applying the signum function to the input data values and estimated error quantities in the estimated gradient calculation and then using an up-down counter accumulator for the one bit gradient as done by Lucky. George, Bowen, and Storey[38] considered the application of both the MZF (using the name applied by Hirsch and Wolf) and the ZF algorithms to a DFE and to a linear equalizer. Their results were opposite to that of Hirsch and Wolf in that the ZF algorithm was faster in acquisition and provided lower MSE in all cases except the low SNR case for the DFE where the

MSE was comparable. Also as one would expect, the DFE was better than the linear equalizer at low or high SNR in both acquisition time and MSE. This difference in results could be due to differences in modulation or to differences in the degree of channel distortion. It has been observed [52] that decision-directed acquisition can have problems when the data eye is initially closed and it has been shown by analysis [71] that a decision-directed acquisition can converge to undesired tap-weights for long but finite periods of time. Thereore, it might be wise to consider the speed advantage reported by George et al.[38] more as a tracking advantage rather than an acquisition advantage, when more severe channel distortions are considered. If more severe channel distortions were to cause problems for tracking of the ZF algorithm, these might be expected to materialize for the linear equalizer and not the DFE since there is no distinction between ZF and MZF with respect to the BE portion of the DFE. For this reason and because decision-directed adaptation is easier to implement than the MZF adaptation, it was decided to use the ZF algorithm. Since the digital radio application typically has high SNR's, and the ZF algorithm and LMS algorithm provide the same performance at high SNR, the ZF algorithm is favoured over the LMS because of its lower complexity and ease of digital implementation.

A simplified diagram of the tap-weight adaptation process is shown in Figure 3.9 for only two forward and two backward taps as in Figure 3.4. This is an implementation of the ZF algorithm using a one bit gradient estimate which is the same as that considered by George et al.[38] with the exceptions that they considered binary baseband transmission and had no carrier recovery and also seemed to have used hard-wired timing.

There is one remaining feature of the tap-weight adaptation to be described. In Figure 3.9, derivation of tap-weights is shown to be dependent only on one or the other of the I-axis or Q-axis error signals instead of the complex error signal which includes both the I-axis and Q-axis error signal. In general, for a complex baseband signal the gradient is a product of the complex data and the complex error signal. Knowledge of the sign of the real and imaginary parts of the complex error signal is not sufficient to determine the sign of the real and imaginary parts of the complex gradient. To avoid this problem, and for another reason to be discussed next, two sets of tap-weights are derived; of which, one set is dependent only on the I-axis error and the other set is dependent only on the Q-axis error as shown in Figure 3.9. The tap-weights which are adjusted according to the I(Q)-axis error signal affect the I(Q)-axis equalized data. The big advantage of doing this lies in the ability of this implementation to correct any small amount of gain or phase imbalance introduced by modulation or demodulation or to correct for linear distortions occurring in the baseband portions of the system including the equalizer itself. For five forward and five backward taps this doubles the number of correlators required from twenty to forty.

The circuit implementation is now described. Referring to Figure 3.9, the quantizer outputs two bits for each data symbol and two bits which represent the sign and magnitude of the difference between the equalized four level data and the decided data. If the decisions are correct this is the error in the received equalized data with respect to the transmitted data. The sign of the decided symbols is shifted through a shift register. The sign of the error is delayed so that the first and second taps are the future and present data and the third and fourth are the past data with respect to the error. The sign bits are then multiplied using exclusive-or gates to obtain the gradient for each tap-weight. A gradient is calculated each symbol period. The gradient information is then accumulated using the up-down counter method of Lucky, which will now be described. The up-down counter is initially set to C. If it counts to 2C or to 0, an 8 bit tap-weight register is incremented or decremented and the counter is reinitialized to C.

The action of the up-down counters is as follows. Assume a small positive error ε in a tap-weight. The

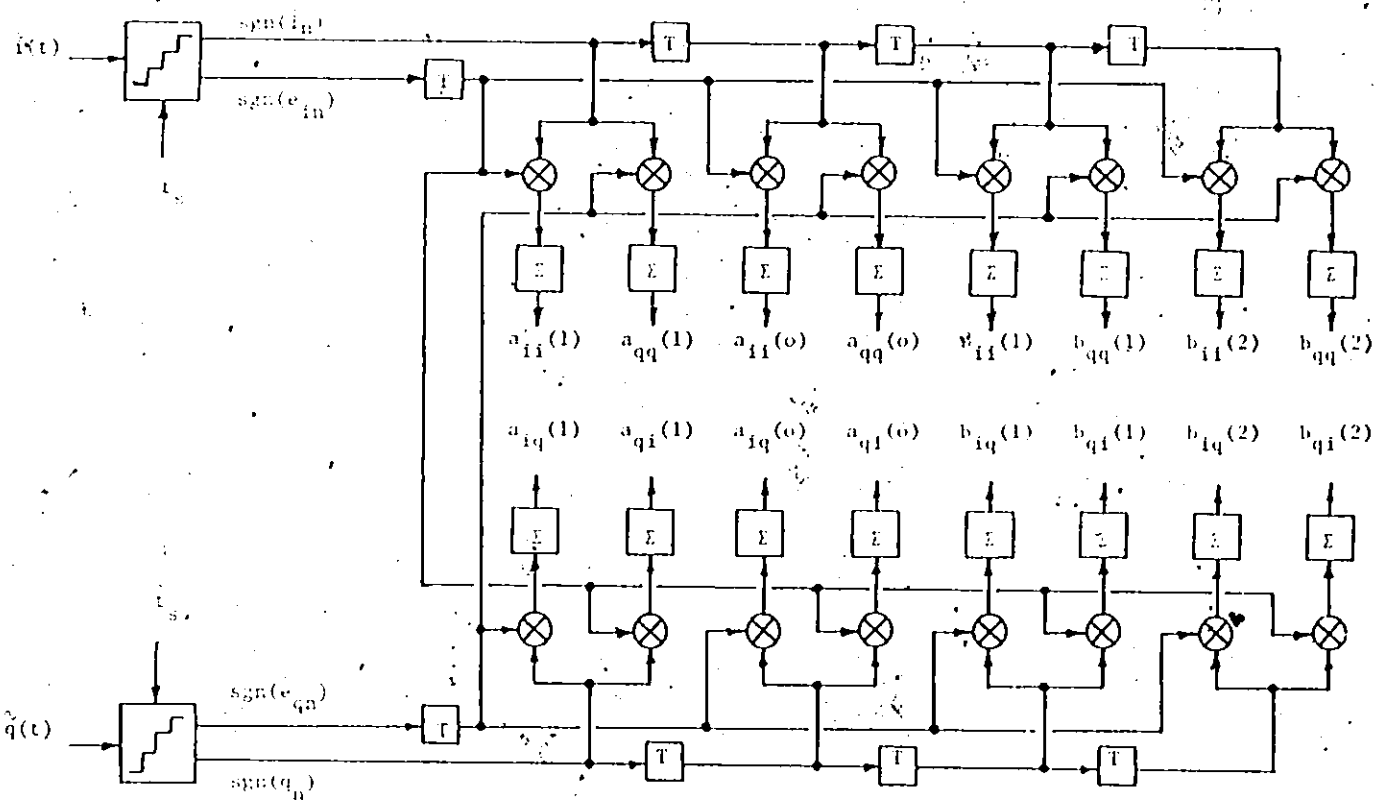

Figure 3.9 Functional Diagram of Decision-Directed Tap-Weight Adjustment Algorithm

probability P_g of a correct gradient indication corresponding to that tap-weight may be only slightly greater than 0.5 due to thermal noise, residual ISI, and misadjustment noise. If the value of C is large enough then the probability of a correct adjustment P_c of the equalizer tap approaches very closely to one and the tap-weight adjustment noise is reduced. Of course, as the value of C is increased the average time between adjustments is longer and the algorithm tracking speed is decreased. Lucky [39] obtained approximate expressions for these relationships. The probability P_g of a correct gradient indication is,

$$P_g \simeq 0.5 + \frac{2d\epsilon}{\sqrt{2\pi\sigma^2}} \qquad P_e < 0.01 \tag{3.1}$$

where 2d is the distance between signal states

ϵ is a small tap-weight error

σ^2 is the variance of the thermal noise, and residual ISI at the decision circuit input which is assummed to be Gaussian with zero mean

P_e is the probability of symbol detection error

The probability P_c that the tap-weight is adjusted in the correct direction is [39],

$$P_c \simeq 1 - ((1-P_g)/P_g)^C \tag{3.2}$$

for P_c close to one. The mean number of counts (baud intervals) $\bar{K}$ between tap-weight adjustments is[39],

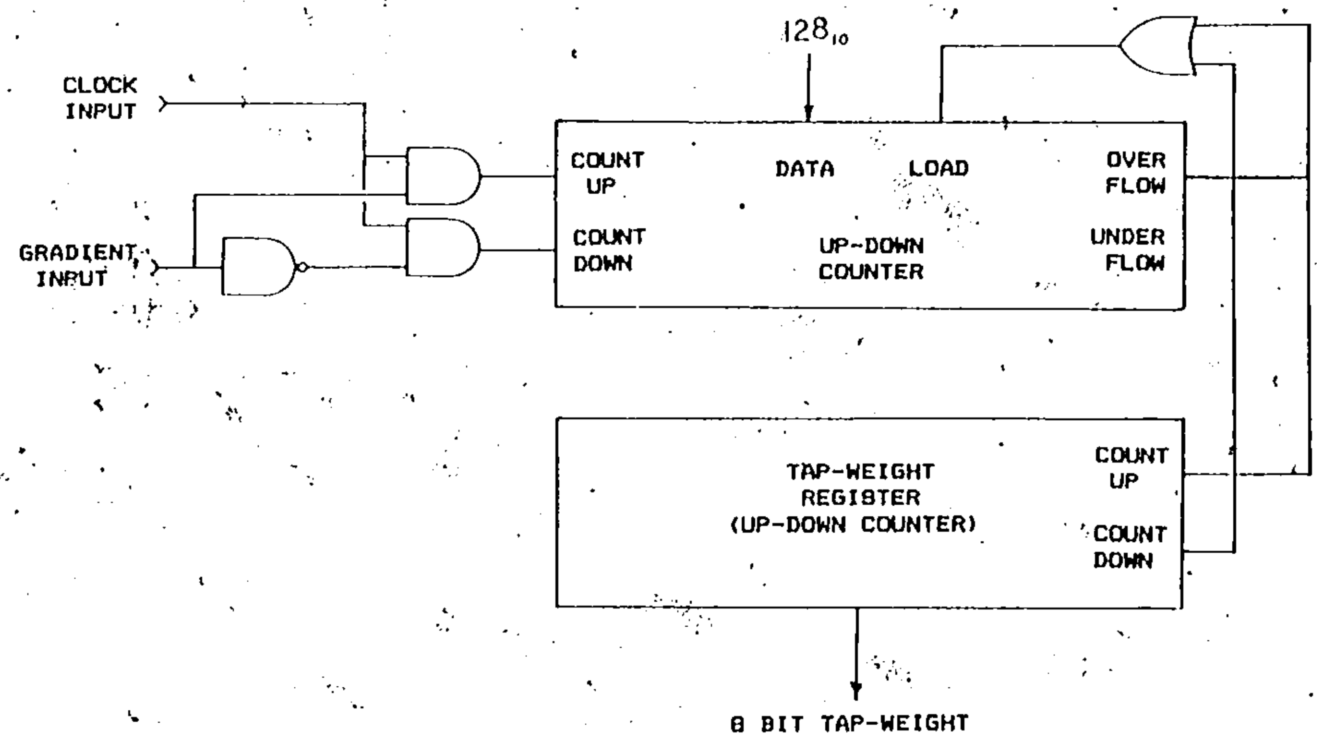

Figure 3.10 Functional Diagram of Up-Down Counter

$$\overline{K} \simeq \frac{C\sqrt{2\pi\sigma^2}}{4d\varepsilon} \qquad (3.3)$$

for P_C close to one. As the tap-weight error gets large the probability of the gradient sign being correct goes to one, provided that the BER is less than approximately 0.01, and the mean number of counts between tap-weight adjustments goes to C. As the tap-weight error goes to zero, the mean number of baud intervals between tap-weight adjustments goes to C^2. For an approximate worst case SNR of around 20dB and tap-weight error of 0.005, to achieve a probability of correct tap-weight adjustment of 0.95 a value of C equal to 60 would be required. For convenience, a value of 128 was used. For larger tap-weight errors at the high SNR typical of a microwave channel, the mean number of baud intervals between tap-weight adjustments would be 128 and a tap-weight could hypothetically track over its full range in 2×128^2 baud intervals which is about 1.4ms which is more than adequate, considering the Doppler spread of the channel. The counter is designed so that the value of C can also be easily set to 8, if desired.

It was decided to use 8 bit quantization for the tap-weights for two reasons. George et al. [38] found in their simulation of an adaptive DFE for a cable channnel at low SNR that when the signal was quantized to 8 bits, 8 bit quantized tap-weight values were just sufficient, but when the signal was quantized to 10 bits the resulting

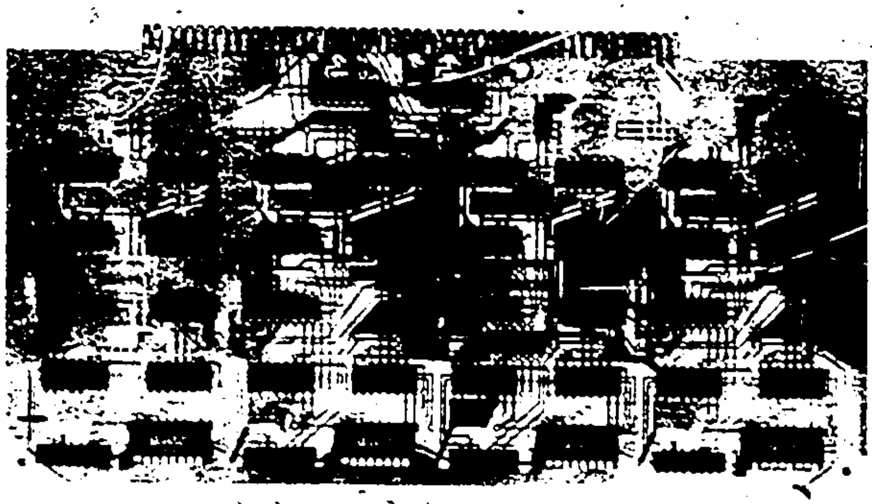

a) Accumulator

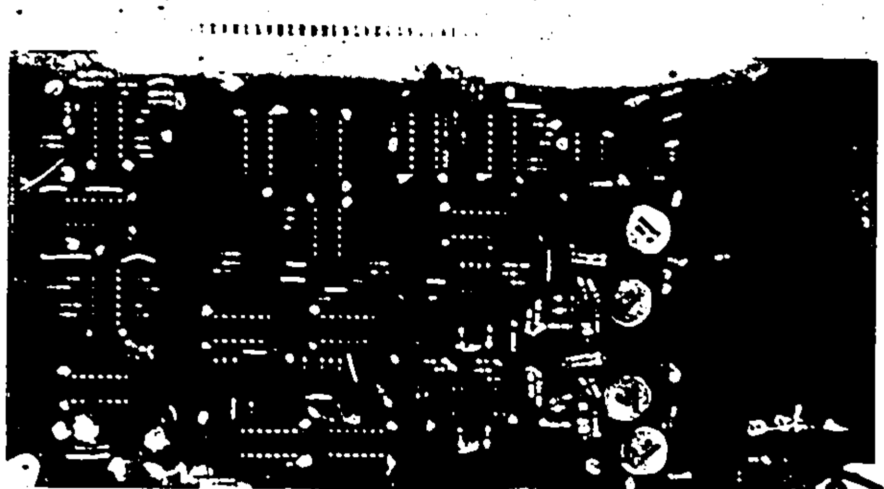

b) Carrier and Clock Recovery, Clock Distribution, Combiner

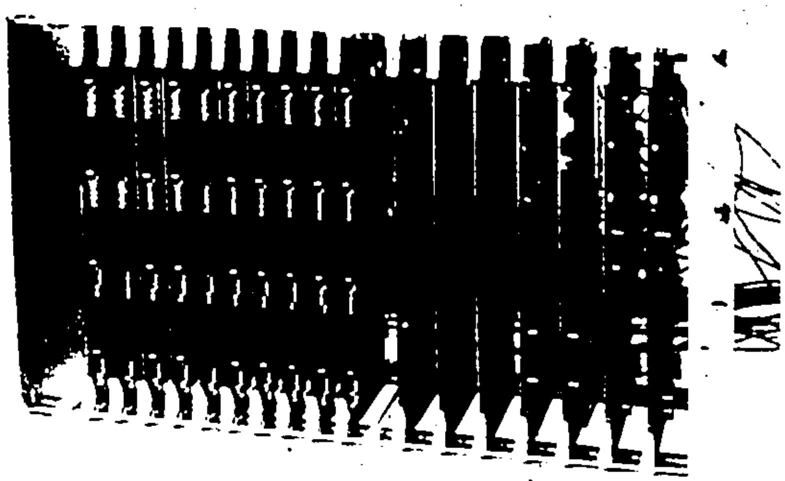

c) Baseband Portion of Receiver (DFE and Data Combiner)

Figure 3.11 Photographs of Up-Down Counter Board, Data Combiner and Clock Distribution Board, and the DFE.

quantization required for the tap-weights was only 6 bits. Since we are considering an analog representation of the signal, it seems then that 8 bits should be sufficient. Then, because of the convenience in digital implementation, 8 bit quantization was used for the tap-weights. The 8 bit tap-weight is converted to analog form for tap-weight multiplication using a D/A as shown in Figure 3.7 for a BE tap-weight.

The forty correlators are implemented using ECL and TTL logic. The accumulator portions are built on ten S100 sized boards as shown in Figure 3.11a. The gradient portions of the adaptation circuitry are included in the two quantizer boards shown in Figure 3.8b. Obviously, the bulk of the components are in the accumulators.

3.6 Carrier and Clock Recovery

The approach taken in carrier and clock recovery is to jointly obtain a minimum mean squared error in the DFE output with respect to the carrier phase, the clock phase and a minimum mean peak error (because of zero forcing) with respect to the DFE tap-weights. The MMSE approach is taken because Niezgoda[64] determined that Mueller's "A" algorithm [76] degraded the MSE by more than an order of magnitude for some cases of multipath fading relative to the MMSE determined clock phase. Niezgoda [64] also demonstrated by simulation that an LMS based joint clock phase and tap-weight adaptive DFE with five forward and five backward taps could track in either direction between minimum phase and non-minimum phase regions of the multipath model. To use the LMS algorithm, it is necessary to derive a gradient of the MSE with respect to the carrier phase error and clock phase error. This is done with a method similar to those of Chang[41], Kobayashi[42], Sailer[45], and Falconer[46].

Two timing recovery methods are shown in Figure 3.12 and Figure 3.13. These methods are similar except that in the first case the gradients are used from both I and Q-axis and the gradients are filtered by an analog low pass filter. In the second case, gradient information from only one axis is used and is accumulated by an up-down counter method, which is the same as that used for the tap-weight adaptation. Both these methods were tried on the laboratory system and the digital method was found to be superior. More will be said about the performance of each loop in Chapter 5 of this thesis.

Now, the details of the clock recovery implementation will be given. A one bit slope detector for clock recovery is obtained by using a high speed comparator to compare the unsampled equalized signal 5ns before and 5ns after the sampling instant. A one bit error estimate is obtained using the third most significant bit of the four bit A/D used as a quantizer. The gradient as formed by the exclusive-or operation on the slope and error bits and the

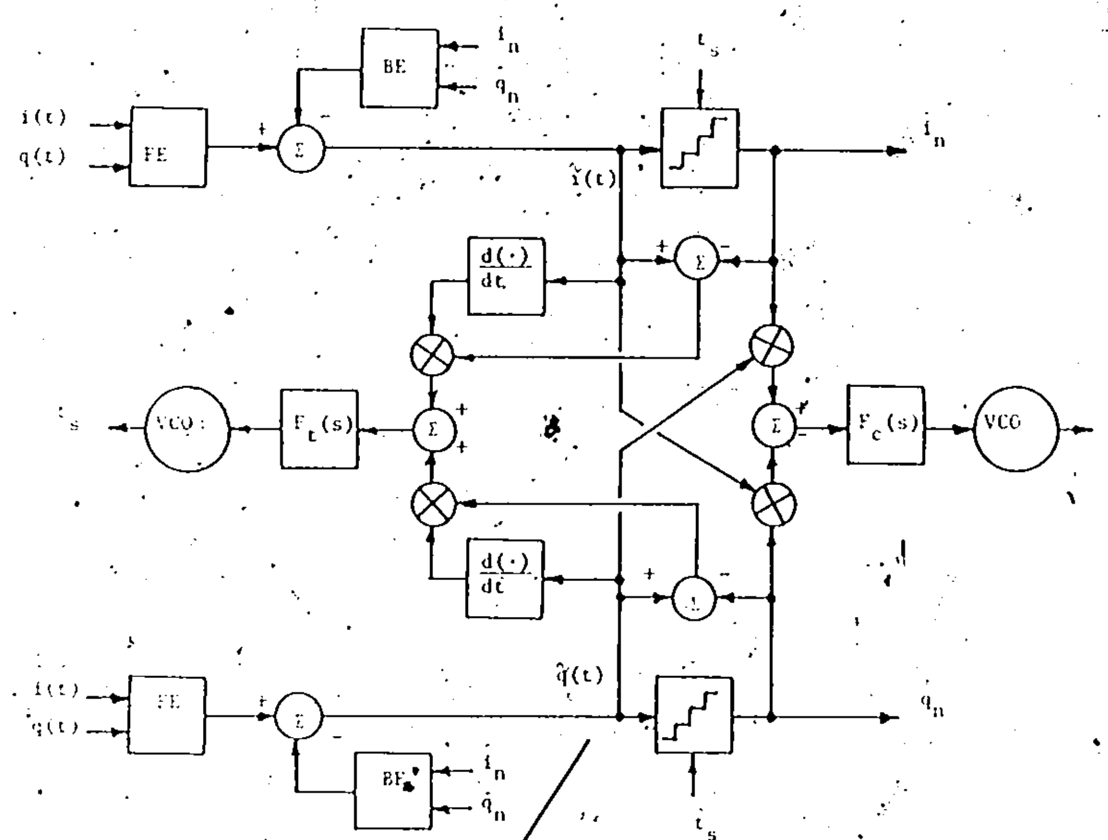

Figure 3.12 Functional Diagram of Analog Clock and Carrier Recovery System (only considered for implementation)

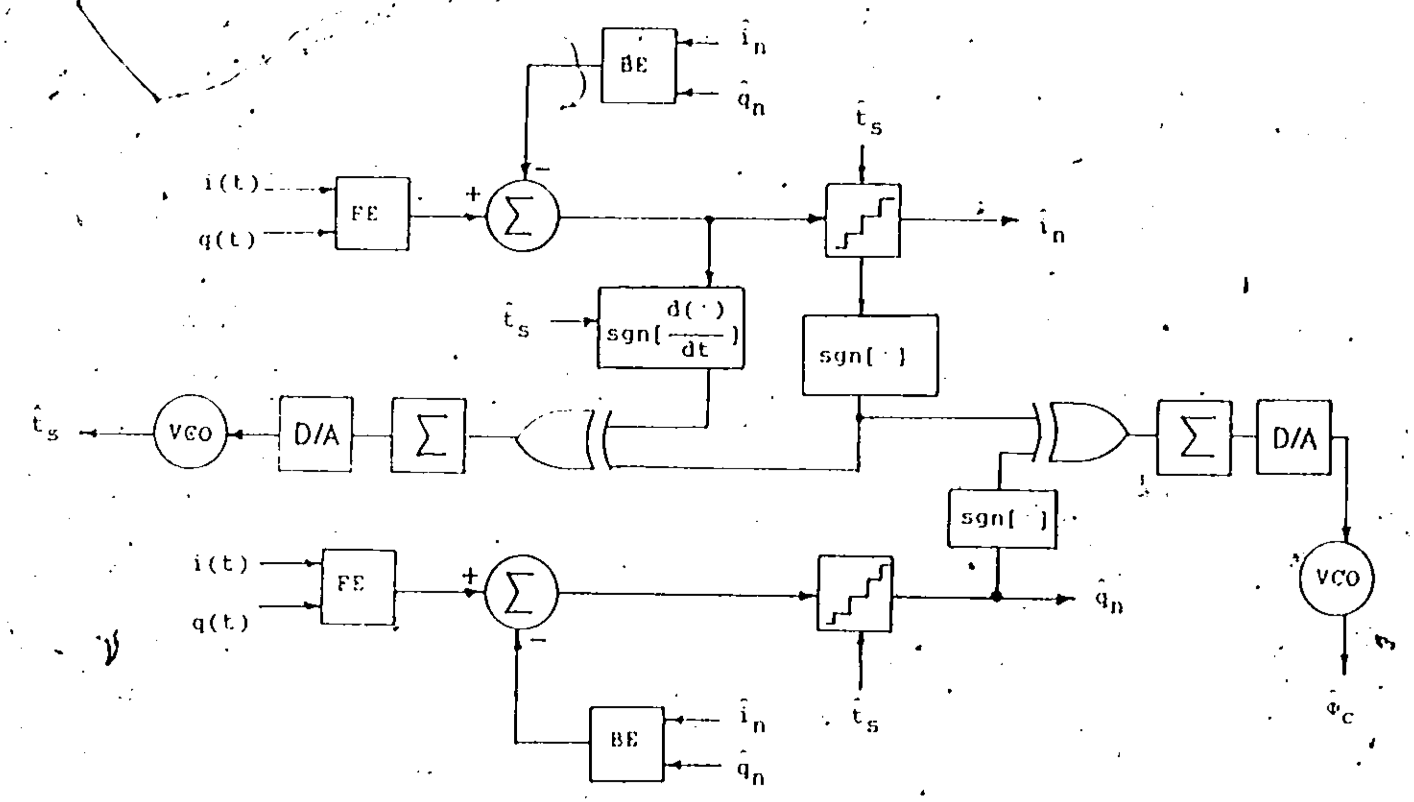

Figure 3.13 Functional Diagram of Implemented Clock Recovery System and Proposed Carrier Recovery System

one bit gradient is accumulated using the same up-down counter technique as used for the tap-weights, with the value of C equal to 128. An 8 bit register is used to hold the estimate of the clock frequency. A D/A is used to control a crystal controlled clock VCO through an approximate differentiator network. This network responds to a step change in the D/A output to cause a short term adjustment of the clock phase and a long term adjustment of the clock frequency. The D/A interface to the VCO is shown in Figure 3.14.

The gradient for the timing recovery loop is obtained on the quantizer circuit board shown in Figure 3.8b where all other gradients are calculated. The gradient is accumulated in the same type of accumulator circuit board as was used for the tap-weights and is shown in Figure 3.11a. The clock VCO is contained on the circuit board shown in Figure 3.11b which also contains all the clock distribution circuitry, the differential decoder, and the four bit parallel to serial combiner which recombines the data into a 90 Mb/s data stream. The complete baseband system is shown in Figure 3.11c. Contained in the S100 card box is everything from the demodulator mixer outputs to the 90 Mb/s data output.

3.7 Carrier Recovery

Two methods are proposed for implementation of carrier recovery and are shown in Figures 3.12 and 3.13. These methods are proposed since carrier recovery has not been implemented yet, for a number of reasons. Since carrier recovery is only required for frequency estimation of the carrier (this is explained shortly) and not carrier phase, the logical course of implementation and debugging of the laboratory system was to get the clock recovery and tap-weight adaptation operational using a arbitrary phase hard-wired carrier. At the point that this was accomplished, it was apparent that there were several hardware implementation problems existing which would limit the possibility of successfully operating the carrier recovery system without considerable hardware modifications. Due to these problems, and because the results obtained with the hardwired carrier were significant, it was decided to write this thesis on the basis of a system which is fully implemented with the exception of carrier recovery. The carrier recovery method in Figure 3.12 is a traditional decision-feedback type. The differences between the two methods are: first, in Figure 3.13 the present decided Q-axis data is correlated with the present I-axis error instead of the present estimated I-axis data; second, in Figure 3.13 there is only half the traditional structure; and third, in Figure 3.13 the gradient information is averaged digitally, by the up-down counter method. For the first difference noted, the two methods are equivalent in the sense that the correlation estimates are the same. This can be seen by observing that the decided I-axis data is uncorrelated with the decided Q-axis data and may be subtracted from the estimated I-axis data without changing the correlation. This means that the gradient for carrier estimation is equivalent to the gradient for the last forward tap cross-axis tap-weight. This is not surprising since any arbitrary phase error in the carrier oscillator can be resolved by the equalizer, provided that tap-weight adaptation can track the difference in frequency between the signal and the oscillator. This causes a a non-unique MMSE solution when the carrier phase is included with the tap-weights and is demonstrated mathematically in Chapter 4 and is discussed by Falconer[46]. Assuming that the magnitude of the last tap complex tap-weight in the FE never goes to zero then the ambiguity can be removed by setting the last tap cross-axis tap-weight in the Q-axis and I-axis sides of the FE to zero. This applies to the structure in Figure 3.12. For Figure 3.13, only the cross-axis tap-weight affecting the I-axis side would be set to zero. With respect to the second difference noted, the reason for using the structure in Figure 3.13 instead of that of Figure 3.12 is the same as discussed in the last section. That is, the carrier phase would be adjusted to minimize the I-axis error, while the cross-axis tap-weight to the Q-axis side minimizes the Q-axis error, and because of this independence of adjustment, gain and phase imbalances in the system can also be removed by the equalizer. The implementation of the carrier recovery loop suggested in Figure 3.13 is favoured because of the experience gained with the clock loop, the advantage of independent I-axis and Q-axis adjustment, and the ease of implementation. However, a definite conclusion on this will have to wait for experimental verification.

3.8 Differential Decoding and Data Combiner Implementation

The differential decoding is the inverse operation to the encoding process done in the transmitter and also combines the parallel data streams back into one serial 90Mbit/s data stream. A significant difference between the transmitter encoding and the receiver decoding is that the encoding operation is a sequential circuit whereas the decoding operation is a combinatorial circuit. Again, a PROM look-up table is used and, not including the timing circuitry, only four chips are used. A functional block diagram of the decoder and data combiner is shown in Figure 3.14 along with the analog portion of the clock recovery loop.

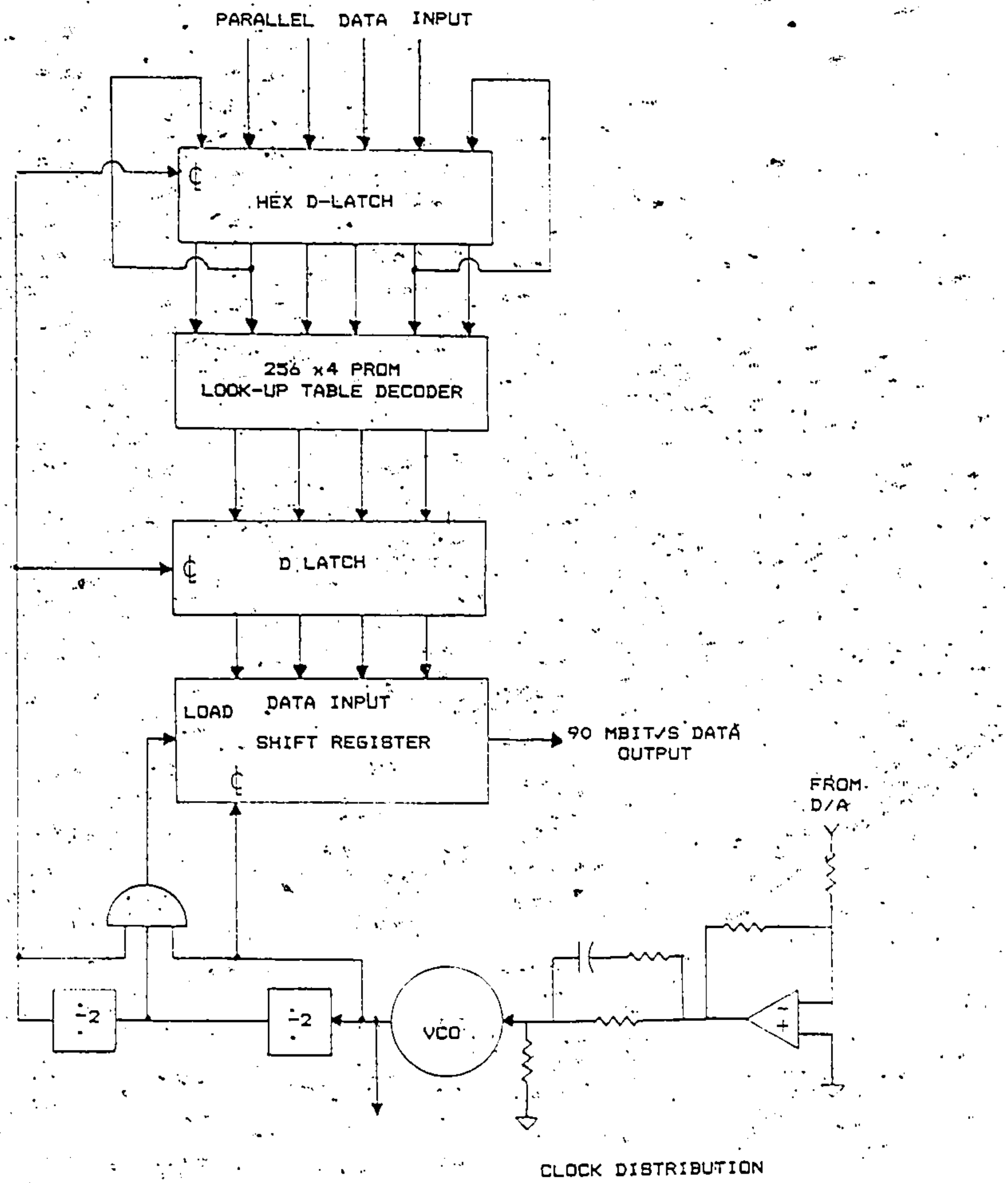

Figure 3.14 Differential Decoder and Data Combiner
Functional Diagram

CHAPTER 4

STABILITY OF THE JOINT ADAPTATION OF TAP-WEIGHTS, SAMPLING PHASE, AND CARRIER PHASE

4.1 Introduction

In digital radio communications systems, three very important functions are carrier recovery, clock recovery, and data equalization. Most high capacity systems use suppressed carrier modulations and have no symbol time reference pilot, so that adaptive carrier phase and timing phase systems are required. The presence of time varying multipath distortion requires the use of adaptive equalization or some other adaptive correction method such as adaptive antenna arrays or even combinations of the two methods. In the "first generation" of digital microwave radio systems, the use of an adaptive antenna array (commonly called 'space diversity') and an adaptive frequency domain equalizer have been favoured over an adaptive time domain equalizer. In the "second generation" of digital microwave radios three have been used[1,19]. As mentioned earlier, it is the intention of this thesis to pursue the exclusive use of time domain equalization for correction of the multipath distortion experienced in microwave radio communications. Without the benefit of space diversity antennas and adaptive frequency domain equalizers, the demands placed on the carrier and clock recovery functions are greater as are, of course, the demands placed on the equalizer itself. For this reason, a clock recovery method which operates jointly with the decision feedback equalizer(DFE) to minimize the mean squared error(MSE) was used in the laboratory experiment. This method was first suggested by Chang [41] and later Kobayashi [42]. Other popular clock recovery methods have been shown [64] to be an order of magnitude worse in MSE than when a joint minimum MSE (MMSE) approach is used. The most difficult problem encountered in the design of the experimental radio was the absence of any theory describing stability conditions for jointly adaptive carrier phase, timing phase, and DFE. This lack of theory has prompted the work in this chapter.

First, in this chapter, we will briefly review the basic theory for MMSE adaptation of a transversal equalizer and then express the operation of the DFE in the same notation so that the results will be applicable to both DFE's and transversal equalizers (TE). Next, we will examine the gradients with respect to tap-weights, sampling phase, and carrier phase and show that minimizing the MSE with respect to tap-weights also minimizes the MSE with respect to the carrier phase for any arbitrary carrier phase and we are then left with two equations to solve for the joint MMSE for the equalizer and the timing recovery. The tap-weight gradient and timing phase gradient are then expanded by use of Taylor's series to express the gradients as a function of tap-weight or weight error vector and timing phase error. This allows us to express the system adaptation as a single matrix equation in the form of the steepest descent algorithm or the expected value of the LMS algorithm. The adjustment matrix of this recursive equation is a non-Toeplitz, real symmetric matrix. The real parameter vector of the equation contains the real and imaginary parts of the tap-weight error vector and the sampling phase error. Knowledge of the eigenvalues of the adjustment matrix, then provides us a method of predicting the stability of the joint adjustment. Algorithms which use instantaneous values or short term time averages as estimates of the gradient are then briefly discussed. Finally, the eigenvalues of the joint adjustment matrix are calculated for an ideal system in the presence of multipath fading, as characterized by Rummler's fading model.

Throughout this chapter the notation used is similar to that used by Haykin[68].

4.2 System Definition

Figure 4.1 shows the system configuration which will be considered. The complex received data signal

$$u(t+(n+M-1)T)\exp(j\Phi)$$

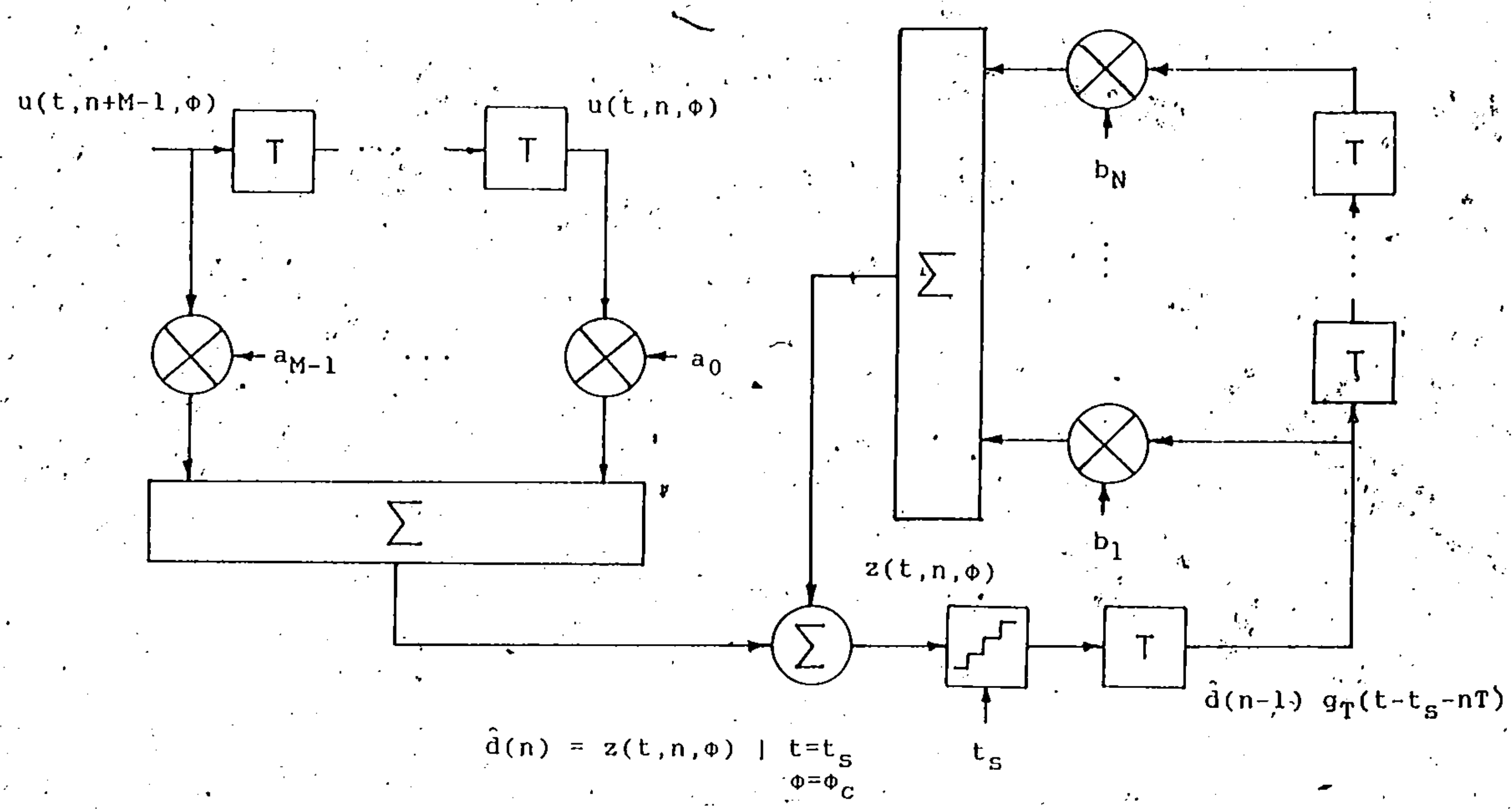

Figure 4.1 Functional Diagram of DFE

enters an M tap transversal equalizer, referred to as the forward equalizer (FE). The FE output is then summed with the output of an N tap transversal equalizer called the backward equalizer (BE) to obtain the quantizer input $z(t,n,\Phi)$ as follows,

$$z(t,n,\Phi) = \sum_{k=0}^{M-1} a_k \, u(t+(n+k)T) \exp(j\Phi) + \sum_{j=1}^{N} b_j \, \tilde{d}(n-j) \, g_T(t-nT-t_s) \tag{4.1}$$

where

$\tilde{d}(n)$ is the complex decided data at time n

a_k is a FE complex tap-weight

b_j is a BE complex tap-weight

$g_T(t) = 1$ for $-T/2 < t < T/2$

$= 0$ elsewhere

It is assumed in this chapter that decisions are made without error and the decided data $\tilde{d}(n)$ is equal to the transmitted data (desired response) $d(n)$, and therefore, I will use the symbol $d(n)$ throughout this chapter to represent the decided data. The complex estimate of the decided data $\hat{d}(n)$ is given by,

$$\hat{d}(n,t_s,\Phi_c) = z(t,n,\Phi) \Big|_{\substack{t=t_s \\ \Phi=\Phi_c}} \tag{4.2}$$

where t_s is the sampling instant

Φ_c is the carrier phase

The quantitizer determines the correct data and also the instantaneous error at n as,

$$e(n,t_s,\phi_c) = \hat{d}(n,t_s,\phi_c) - d(n) \qquad (4.3)$$

The estimate of the data at the quantitizer input can be expressed as,

$$\hat{d}(n,t_s,\phi_c) = \underset{\sim}{u}^T(n,t_s,\phi_c)\,\underset{\sim}{w} \qquad (4.4)$$

where $\underset{\sim}{u}(n,t_s,\phi_c)$ and $\underset{\sim}{w}$ are the sampled data vector and the weight or tap-weight vector at time n defined as,

$$\underset{\sim}{u}(n,t_s,\phi_c) = \left[\begin{array}{l} u(t+(n+m-1)T)\ \exp(j\phi) \\ u(t+(n+m-2)T)\ \exp(j\phi) \\ \vdots \\ u(t+nT)\ \exp(j\phi) \\ d(n-1)\ g_T(t-t_s-nT) \\ \vdots \\ d(n-N)\ g_T(t-t_s-nT) \end{array}\right]_{\substack{t=t_s \\ \phi=\phi_c}} \qquad (4.5)$$

$$\underset{\sim}{w} = \begin{bmatrix} \underset{\sim}{a} \\ \underset{\sim}{b} \end{bmatrix} \qquad (4.6)$$

where

$$\underset{\sim}{a} = \begin{bmatrix} a_{M-1} \\ \vdots \\ a_0 \end{bmatrix} \qquad (4.7)$$

$$\underset{\sim}{b} = \begin{bmatrix} b_1 \\ \cdot \\ \cdot \\ b_N \end{bmatrix} \qquad (4.8)$$

Also the forward and backward data vector are,

$$\underset{\sim}{u}_f(n,t_s,\phi_c) = \begin{bmatrix} u(t+(n+m-1)T)\ \exp(j\phi) \\ \cdot \\ u(t+nT)\ \exp(j\phi) \end{bmatrix}_{\substack{t=t_s \\ \phi=\phi_c}} \qquad (4.9)$$

$$\underset{\sim}{u}_b(n,t_s,\phi_c) = \begin{bmatrix} d(n-1)\ g_T(t-t_s-nT) \\ d(n-2)\ g_T(t-t_s-nT) \\ \cdot \\ d(n-N)\ g_T(t-t_s-nT) \end{bmatrix} \qquad (4.10)$$

If we are discussing a transversal equalizer (TE) at the same time the backward data vector could be defined as,

$$\underset{\sim}{u}_b(n,t_s,\phi_c) = \begin{bmatrix} u(t+(n-1)T)\ \exp(j\phi) \\ \cdot \\ u(t+(n-m)T)\ \exp(j\phi) \end{bmatrix}_{\substack{t=t_s \\ \phi=\phi_c}} \qquad (4.10a)$$

In either case the data vector $\underset{\sim}{u}$ may be written as,

$$\underset{\sim}{u}(n;t_s,\phi_c) = \begin{bmatrix} \underset{\sim}{u}_f(n,t_s,\phi_c) \\ \underset{\sim}{u}_b(n,t_s,\phi_c) \end{bmatrix} \qquad (4.10b)$$

As shown in Equations (4.2) through to Equation (4.10), sampled data vectors can be defined even though the sampling is done at the quantitizer input. The mean square error is expressed as,

$$J(t_s,\Phi_c) = E[\ e^*(n,t_s,\Phi_c)\ e(n,t_s,\Phi_c)\ ]$$

$$= E[\ (\ d^*(n) - \underset{\sim}{w}^H\ \underset{\sim}{u}^*(n,t_s,\Phi_c)\ ).(\ d(n) - \underset{\sim}{u}^T(n,t_s,\Phi_c)\ \underset{\sim}{w}\ )\ ]$$

$$= r_d(0) - \underset{\sim}{r}^H_{du}(t_s,\Phi_c)\ \underset{\sim}{w} - \underset{\sim}{w}^H\ \underset{\sim}{r}_{du}(t_s,\Phi_c) + \underset{\sim}{w}^H\ \underset{\sim}{R}_u(t_s,\Phi_c)\ \underset{\sim}{w} \qquad (4.11)$$

where

$$r_d(0) = E[\ d^*(n)\ d(n)\ ] \qquad (4.12)$$

$$\underset{\sim}{r}_{du}(t_s,\Phi_c) = E[\ d(n)\ \underset{\sim}{u}^*(n,t_s,\Phi_c)\ ] \qquad (4.13)$$

$$\underset{\sim}{R}_u(t_s,\Phi_c) = E[\ \underset{\sim}{u}^*(n,t_s,\Phi_c)\ \underset{\sim}{u}^T(n,t_s,\Phi_c)\ ] \qquad (4.14)$$

where it is assumed that $\underset{\sim}{u}$ and d are jointly stationary and,

$r_d(0)$ is the autocorrelation function of the desired response at zero lag.

$\underset{\sim}{r}_{du}(t_s,\Phi_c)$ is the M+Nx1 cross-correlation vector of the desired response and the matrix

$\underset{\sim}{R}_u(t_s,\Phi_c)$ is the (M+N)x(M+N) autocorrelation matrix of the data vector $\underset{\sim}{u}(n,t_s,\Phi_c)$

$\underset{\sim}{r}^H_{du}(t_s,\Phi_c)$ is the Hermitian transpose of $\underset{\sim}{r}_{du}(t_s,\Phi_c)$

$\underset{\sim}{u}^T(n,t_s,\Phi_c)$ is the transpose of $\underset{\sim}{u}(n,t_s,\Phi_c)$

It should be noted that, for the special case of a transversal equalizer (TE), the autocorrelation matrix is independent of Φ_c. however, since $\underset{\sim}{u}(n,t_s,\Phi_c)$ is not stationary with respect to t_s then,

$$\underset{\sim}{R}_u(t_s) = \underset{\sim}{R}_u(t_s,\Phi_c) \quad \text{(TE only)} \tag{4.15}$$

The autocorrelation matrix and cross-correlation vector can also be expressed as follows,

$$\underset{\sim}{r}_{du}(t_s,\Phi_c) = \begin{bmatrix} \underset{\sim}{r}_{df}(t_s,\Phi_c) \\ \underset{\sim}{r}_{db}(t_s,\Phi_c) \end{bmatrix} \tag{4.16}$$

$$\underset{\sim}{R}_u(t_s,\Phi_c) = \begin{bmatrix} \underset{\sim}{R}_{ff}(t_s) & \underset{\sim}{R}_{fb}(t_s,\Phi_c) \\ \underset{\sim}{R}^H_{fb}(t_s,\Phi_c) & \underset{\sim}{R}_{bb}(t_s) \end{bmatrix} \tag{4.17}$$

where $\underset{\sim}{r}_{df}(t_s,\Phi_c)$ is the Mx1 cross-correlation vector of the desired response and the data vector $u_f(n,t_s,\Phi_c)$

$\underset{\sim}{r}_{db}(t_s,\Phi_c)$ is the Nx1 cross-correlational vector of the desired response and the data $u_b(n,t_s,\Phi_c)$

$\underset{\sim}{R}_{ff}(t_s)$ is the MxM autocorrelation matrix of $\underset{\sim}{u}_f(n,t_s,\Phi_c)$

$\underset{\sim}{R}_{bb}(t_s)$ is the NxN autocorrelation matrix of $\underset{\sim}{u}_b(n,t_s,\Phi_c)$

and $\underset{\sim}{R}_{fb}(t_s,\Phi_c)$ is the MxN cross-correlation matrix of $\underset{\sim}{u}_f(n,t_s,\Phi_c)$ and $\underset{\sim}{u}_b(n,t_s,\Phi_c)$

The definitions of $\underset{\sim}{R}_{ff}$, $\underset{\sim}{R}_{bb}$ and $\underset{\sim}{R}_{fb}$ are obtained from,

$$\underset{\sim}{R}_u(t_s,\Phi_c) = E\left[\begin{bmatrix}\underset{\sim}{u}_f^*(n,t_s,\Phi_c)\\ \underset{\sim}{u}_b^*(n,t_s,\Phi_c)\end{bmatrix}\begin{bmatrix}\underset{\sim}{u}_f^T(n,t_s,\Phi_c) & \underset{\sim}{u}_b^T(n,t_s,\Phi_c)\end{bmatrix}\right]$$

$$= E\begin{bmatrix}\underset{\sim}{u}_f^*(n,t_s,\Phi_c)\,\underset{\sim}{u}_f^T(n,t_s,\Phi_c) & \underset{\sim}{u}_f^*(n,t_s,\Phi_c)\,\underset{\sim}{u}_b^T(n,t_s,\Phi_c)\\ \underset{\sim}{u}_b^*(n,t_s,\Phi_c)\,\underset{\sim}{u}_f^T(n,t_s,\Phi_c) & \underset{\sim}{u}_b^*(n,t_s,\Phi_c)\,\underset{\sim}{u}_b^T(n,t_s,\Phi_c)\end{bmatrix} \tag{4.18}$$

or

$$\underset{\sim}{R}_{ff}(t_s) = E[\,\underset{\sim}{u}_f^*(n,t_s,\Phi_c)\,\underset{\sim}{u}_f^T(n,t_s,\Phi_c)\,] \tag{4.19}$$

$$\underset{\sim}{R}_{bb}(t_s) = E[\,\underset{\sim}{u}_b^*(n,t_s,\Phi_c)\,\underset{\sim}{u}_b^T(n,t_s,\Phi_c)\,] \tag{4.20}$$

$$\underset{\sim}{R}_{fb}(t_s,\Phi_c) = E[\,\underset{\sim}{u}_f^*(n,t_s,\Phi_c)\,\underset{\sim}{u}_b^T(n,t_s,\Phi_c)\,] \tag{4.21}$$

For the TE case there is really nothing to be gained by using the quantities, $\underset{\sim}{r}_{df}$, $\underset{\sim}{r}_{db}$, $\underset{\sim}{R}_{ff}$, $\underset{\sim}{R}_{bb}$, $\underset{\sim}{R}_{bf}$; however, these representations facilitate the discussion of the DFE with an independent (versus n) desired response. When it is assumed that we are dealing with a DFE and that the desired response is sample to sample independent, then,

$$\underset{\sim}{R}_{bb}(t_s) = r_d(0)\underset{\sim}{I} \tag{4.22}$$

$$\underset{\sim}{r}_{db}(t_s,\Phi_c) = \underset{\sim}{0} \tag{4.23}$$

Also all the remaining quantities in Equation (4.16) and (4.17) can be defined in terms of the autocorrelation functions $r_u(k,t_s)$ and $r_{du}(k,t_s,\Phi_c)$.

where,

$$r_u(k,t_s) = E[\, u^*(n,t_s)\; u(n+k,t_s)\,] \tag{4.24}$$

$$-M+1 < k < M-1$$

$$r_{du}(k,t_s,\Phi_c) = E[\, d^*(n)\; u(n+k,t_s,\Phi_c)\,] \tag{4.25}$$

$$-M-N+1 < k < M+N-1$$

For convenience, the dependence of the autocorrelation matricies and the cross-correlation matricies and cross-correlation vectors will not be stated explicitly from here on. We must take care to remember that all the autocorrelation quantities are functions of the sampling instant and that the cross-correlation quantities are functions of both the sampling phase t_s and the carrier phase Φ_c.

4.3 Minimization With Respect To Tap-Weights, Sampling Phase, Carrier Phase

It is desired to find a simultaneous solution to the following three equations,

$$\nabla_{\underset{\sim}{w}} = 0 \tag{4.26}$$

$$\nabla_t = 0 \tag{4.27}$$

$$\nabla_\Phi = 0 \tag{4.28}$$

where $\nabla_{\underset{\sim}{w}}$ is the gradient of the MSE with respect to $\underset{\sim}{w}$,
∇_t is the gradient of the MSE with respect to t_s
∇_Φ is the gradient of the MSE with respect to Φ_c

We shall denote the quantities $\underset{\sim}{w}_o$, t_o and Φ_o as the values of $\underset{\sim}{w}$, t_s, and Φ_c which satisfy Equations (4.26), (4.27), and (4.28). Also, we shall denote $\underset{\sim}{w}_s$ as the weight vector which satisfies Equation (4.26) for arbitrary values of t_s and Φ_c. When the gradient in (4.26) is evaluated [68] the well known Normal Equation or discrete form of the Wiener-Hopf Equation is obtained as,

$$\underset{\sim}{r}_{du} = \underset{\sim}{R}_u \, \underset{\sim}{w}_s \tag{4.29}$$

For the DFE with independent desired response samples, Equation (4.29) may also be expressed as the two equations,

$$\underset{\sim}{r}_{df} = \underset{\sim}{R}_a \, \underset{\sim}{a}_s \tag{4.30}$$

$$\underset{\sim}{b}_s = \frac{-1}{r_d(0)} \, \underset{\sim}{R}_{fb}^H \, \underset{\sim}{a}_s \tag{4.31}$$

where

$$\underset{\sim}{w}_s = \begin{bmatrix} \underset{\sim}{a}_s \\ \underset{\sim}{b}_s \end{bmatrix} \tag{4.32}$$

$$\underset{\sim}{R}_a = \underset{\sim}{R}_{ff} - \frac{1}{r_d(0)} R_{fb} \, R_{fb}^H \tag{4.33}$$

The advantages of using (4.30) and (4.31) over (4.29) are that only one Mth order matrix inversion is required compared with an M+N order inversion, to determine $\mathbf{w}_s$. In addition (4.30) and (4.31), provide more insight into the operation of the DFE. The derivative of the MSE with respect to the sampling phase t_s is given by,

$$\nabla_t = -\dot{\mathbf{r}}_{du}^H \mathbf{w} - \mathbf{w}^H \dot{\mathbf{r}}_{du} + \mathbf{w}^H \dot{\mathbf{R}}_u \mathbf{w} \qquad (4.34)$$

where the derivitives $\dot{\mathbf{r}}_{du}$ and $\dot{\mathbf{R}}_u$ are given by,

$$\dot{\mathbf{r}}_{du} = E[\, d(n)\, \dot{\mathbf{u}}^*(n) \,] \qquad (4.35)$$

$$\dot{\mathbf{R}}_u = E[\, \dot{\mathbf{u}}^*(n)\, \mathbf{u}^T(n) + \mathbf{u}^*(n)\, \dot{\mathbf{u}}^T(n) \,] \qquad (4.36)$$

In DFE form (4.34) is,

$$\nabla_t = -\dot{\mathbf{r}}_{df}^H \mathbf{a} - \mathbf{a}^H \dot{\mathbf{r}}_{df} + \mathbf{a}^H \dot{\mathbf{R}}_{ff} \mathbf{a} + \mathbf{b}^H \dot{\mathbf{R}}_{fb}^H \mathbf{a} + \mathbf{a}^H \dot{\mathbf{R}}_{fb} \mathbf{b} \qquad (4.37)$$

The derivative with respect to the carrier phase Φ_o is for the TE case,

$$\nabla_\Phi = j\, \mathbf{r}_{du}^H \mathbf{w} - j\, \mathbf{w}^H \mathbf{r}_{du} \qquad (4.38)$$

(TE only)

and for the DFE case,

$$\nabla_\Phi = j\, \mathbf{r}_{df}^H \mathbf{a} - j\, \mathbf{a}^H \mathbf{r}_{df} + j\, \mathbf{b}^H \mathbf{R}_{fb}^H \mathbf{a} - j\, \mathbf{a}^H \mathbf{R}_{fb} \mathbf{b}$$

(DFE only) (4.39)

With Equations (4.29) to (4.39) we may now consider the simultaneous solution of the Equations (4.26), (4.27) and (4.28). First, we show that minimizing the MSE with respect to $\underset{\sim}{w}$ also minimizes the MSE with respect to Φ_c. By substituting for $\underset{\sim}{w}_s$ in (4.37) from Equation (4.29) we obtain,

$$\nabla_\Phi = j\, \underset{\sim}{r}_{du}^{H} \underset{\sim}{R}_{u}^{-1} \underset{\sim}{r}_{du} - j\, \underset{\sim}{r}_{du}^{H} \underset{\sim}{R}_{u}^{-1} \underset{\sim}{r}_{du}$$

$$= 0 \qquad \begin{array}{r}(4.40)\\ \text{(TE only)}\end{array}$$

By substituting for $\underset{\sim}{a}_s$, and $\underset{\sim}{b}_s$ in Equation (4.39) we obtain,

$$\nabla_\Phi = j\, \underset{\sim}{r}_{df}^{H} \underset{\sim}{R}_{a}^{-1} \underset{\sim}{r}_{df} - j\, \underset{\sim}{r}_{df}^{H} \underset{\sim}{R}_{a}^{-1} \underset{\sim}{r}_{df}$$

$$= 0 \qquad \begin{array}{r}\text{(DFE only)}\\ (4.41)\end{array}$$

To obtain (4.40) and (4.41) we have used the fact that $\underset{\sim}{R}_a$, $\underset{\sim}{R}_a^{-1}$, $\underset{\sim}{R}_u^{-1}$ are Hermitian. It is not surprising that the Normal Equation (4.26) also satisfies Equation (4.28) since the equalizer taps are complex and can resolve any phase shift. It remains then to substitute the Normal Equation into the gradient equation for sampling phase to obtain the simultaneous solution for $\underset{\sim}{w}_o$ and t_o.

$$-\underset{\sim}{r}_{du}^{H} \underset{\sim}{R}_{u}^{-1} \underset{\sim}{r}_{du} - \underset{\sim}{r}_{du}^{H} \underset{\sim}{R}_{u}^{-1} \underset{\sim}{r}_{du} + \underset{\sim}{r}_{du}^{H} \underset{\sim}{R}_{u}^{-1} \underset{\sim}{R}_{u} \underset{\sim}{R}_{u}^{-1} \underset{\sim}{r}_{du} = 0 \qquad (4.42)$$

For the DFE case we have,

$$\underset{\sim}{r}_{df}^{H} \underset{\sim}{R}_{a}^{-1} \left[\underset{\sim}{R}_{ff} - \frac{1}{r_d(0)} \left(\underset{\sim}{R}_{fb} \underset{\sim}{R}_{fb}^{H} + \underset{\sim}{R}_{fb} \underset{\sim}{R}_{fb}^{H} \right) \right] \underset{\sim}{R}_{a}^{-1} \underset{\sim}{r}_{df}$$

$$- \underset{\sim}{r}_{df}^{H} \underset{\sim}{R}_{a}^{-1} \underset{\sim}{r}_{df} - \underset{\sim}{r}_{df}^{H} \underset{\sim}{R}_{a}^{-1} \underset{\sim}{r}_{df} = 0 \qquad (4.43)$$

Since every quantity except $r_d(0)$ in Equations (4.42) and (4.43) is a function of t_s, a closed form solution of (4.42) or (4.43) is not possible. However, using numerical techniques a fixed step size gradient method was used to determine t_o and $\underset{\sim}{w}_o$ at time n according to the algorithm,

$$t_s(m+1) = t_s(m) + \mu \operatorname{sgn}[\, \nabla_t \mid \underset{\sim}{w}=\underset{\sim}{w}_o \,] \qquad (4.44)$$

where m is a recurrsion index and we assume,

$$t_s(0) = 0 \qquad (4.44a)$$

If we do not wish to evaluate the inverse $\underset{\sim}{R}_a^{-1}$ or $\underset{\sim}{R}_u^{-1}$ on every iteration then we can also use the steepest descent or gradient algorithm to obtain $\underset{\sim}{w}_o$ and t_o as follows,

$$\underset{\sim}{w}(m+1) = \underset{\sim}{w}(m) + \mu \left[\, 2\, \underset{\sim}{r}_{du}(m) - 2\, \underset{\sim}{R}_u(m)\, \underset{\sim}{w}(m) \,\right] \qquad (4.45)$$

$$t_s(m-1) = t_s(m) \qquad (4.46)$$

$$+ \mu \left[\, \underset{\sim}{r}_{du}^{H}(m)\, \underset{\sim}{w}(m) + \underset{\sim}{w}^{H}(m)\, \underset{\sim}{r}_{du}(m) - \underset{\sim}{w}^{H}(m)\, \underset{\sim}{R}_u(m)\, \underset{\sim}{w}(m) \,\right]$$

where $\qquad t_s(0) = 0 \qquad (4.46a)$

$$\underset{\sim}{a}(0) = \begin{bmatrix} (0,0) \\ \vdots \\ (0,0) \\ (1,0) \end{bmatrix} \qquad (4.46b)$$

$$\underset{\sim}{b}(0) = \underset{\sim}{0} \qquad (4.46c)$$

4.4 Stability of the Steepest Descent Algorithm

In order to determine the requirements for stabilty of the steepest descent algorithm we would like to express Equations (4.45) and (4.46) as a single equation in the following form,

$$\begin{aligned} \underset{\sim}{p}(n+1) &= \underset{\sim}{p}(n) - \mu \, \underset{\sim}{\nabla}_p(n) \\ &= \underset{\sim}{p}(n) - \mu \, \underset{\sim}{R}_p \, \underset{\sim}{p}(n) \qquad (4.47) \end{aligned}$$

where

$\underset{\sim}{p}$ is a parameter 2(M+N)+1 vector containing both the weight errors and sampling instant errors

$\underset{\sim}{R}_p$ is a 2(M+N)+1 square real adjustment matrix is similar to a diagonal matrix

and

$\underset{\sim}{\nabla}_p$ is the 2(M+N)+1 gradient vector with respect to $\underset{\sim}{p}$

By a similarity transformation, Equation (4.47) may then be expressed as a set of independent first order difference equations for which the convergence requirements step size μ are easily determined. Since neither $\underset{\sim}{\nabla}_w$ nor ∇_t have any explicit dependence on the sampling instant t_s an obvious approach is to express $\nabla_{\mathbf{w}}(t_s)$ and $\nabla_t(t_s)$ as a Taylor's series about the optimum sampling instant t_o. Let the weight error vector be,

$$\mathbf{c} = \mathbf{w} - \mathbf{w}_o \tag{4.48}$$

and let the sampling error be,

$$t_e = t_s - t_o \tag{4.49}$$

The series expansions of the autocorrelation matricies and cross-correlation vectors are,

$$\mathbf{R}_u = \mathbf{R}_{uo} + t_e \dot{\mathbf{R}}_{uo} + \frac{1}{2!} t_e^2 \ddot{\mathbf{R}}_{uo} + \cdots \tag{4.50}$$

$$\dot{\mathbf{R}}_u = \dot{\mathbf{R}}_{uo} + t_e \ddot{\mathbf{R}}_{uo} + \frac{1}{2!} t_e^2 \dddot{\mathbf{R}}_{uo} + \cdots \tag{4.51}$$

$$\mathbf{r}_{du} = \mathbf{r}_{duo} + t_e \dot{\mathbf{r}}_{duo} + \frac{1}{2!} t_e^2 \ddot{\mathbf{r}}_{duo} + \cdots \tag{4.52}$$

$$\dot{\mathbf{r}}_{du} = \dot{\mathbf{r}}_{du} + t_e \ddot{\mathbf{r}}_{duo} + \cdots \tag{4.53}$$

where $\mathbf{R}_{uo}$ is the autocorrelation matrix evaluated at a sampling instant of t_o then,

$$\begin{aligned}\nabla_{\mathbf{w}}(t_s) = 2 [\, & \mathbf{R}_{uo} \mathbf{c} + \frac{1}{2} t_e \dot{\mathbf{R}}_{uo} \mathbf{c} + \frac{1}{2} \frac{1}{2!} t_e^2 \ddot{\mathbf{R}}_{uo} \mathbf{c} + \cdots \\ & + t_e (-\dot{\mathbf{r}}_{duo} + \frac{1}{2} \dot{\mathbf{R}}_{uo} \mathbf{c} + \dot{\mathbf{R}}_{uo} \mathbf{w}_o) \\ & + \frac{1}{2!} t_e^2 (-\ddot{\mathbf{r}}_{duo} + \frac{1}{2} \ddot{\mathbf{R}}_{uo} \mathbf{c} + \ddot{\mathbf{R}}_{uo} \mathbf{w}_o) + \cdots \,]\end{aligned} \tag{4.54}$$

$$\begin{aligned}\nabla_t(t_s) = {} & (-\underset{\sim}{r}^H_{duo} + \underset{\sim}{w}^H_o \underset{\sim}{R}_{uo} + \tfrac{1}{2} \underset{\sim}{c}^H \underset{\sim}{R}_{uo}) \underset{\sim}{c} \\ & + \underset{\sim}{c}^H (-\underset{\sim}{r}_{duo} + \underset{\sim}{R}_{uo} \underset{\sim}{w}_o + \tfrac{1}{2} \underset{\sim}{R}_{uo} \underset{\sim}{c}) \\ & + t_e \, [\, (-\underset{\sim}{r}^H_{duo} + \underset{\sim}{w}^H_o \underset{\sim}{R}_{uo} + \tfrac{1}{2} \underset{\sim}{c}^H \underset{\sim}{R}_{uo}) \underset{\sim}{c} \\ & \qquad + \underset{\sim}{c}^H (-\underset{\sim}{r}_{duo} + \underset{\sim}{R}_{uo} \underset{\sim}{w}_o + \tfrac{1}{2} \underset{\sim}{R}_{uo} \underset{\sim}{c}) \,] \\ & + t_e \, [-\underset{\sim}{r}^H_{duo} \underset{\sim}{w}_o - \underset{\sim}{w}^H_o \underset{\sim}{r}_{duo} + \underset{\sim}{w}^H_o \underset{\sim}{R}_u \underset{\sim}{w}_o] \\ & + \tfrac{1}{2!} t_e^2 \, [\ldots] + \ldots \end{aligned} \tag{4.55}$$

where we have used the fact that,

$$-\underset{\sim}{r}_{duo} + \underset{\sim}{R}_{uo} \underset{\sim}{w}_o = 0 \tag{4.56}$$

and

$$-\underset{\sim}{r}^H_{duo} \underset{\sim}{w}_o - \underset{\sim}{w}^H_o \underset{\sim}{R}_{uo} + \underset{\sim}{w}^H_o \underset{\sim}{R}_{uo} \underset{\sim}{w}_o = 0 \tag{4.57}$$

in simplifying Equations (4.54) and (4.55).

Equations (4.54) and (4.55) may be rewritten as;

$$\underset{\sim}{\nabla}_w(t_s) = 2 \underset{\sim}{R}_{ui} \underset{\sim}{c} + 2 \underset{\sim}{g}_i t_e \tag{4.58}$$

$$\begin{aligned}\underset{\sim}{\nabla}_t(t_s) &= \underset{\sim}{g}^H \underset{\sim}{c} + \underset{\sim}{c}^H \underset{\sim}{g} + \underset{\sim}{g}_i t_e \\ &= \underset{\sim}{g}^H \underset{\sim}{c} + (\underset{\sim}{g}^H)^* \underset{\sim}{c}^* + f_i t_e \end{aligned} \tag{4.59}$$

where

$$\underset{\sim}{R}_{ui} = \frac{1}{2} \underset{\sim}{R}_{uo} + \frac{1}{2} \underset{\sim}{R}_u \tag{4.60}$$

$$\underset{\sim}{g}_o = -\underset{\sim}{r}_{duo} + \frac{1}{2}\underset{\sim}{R}_{uo}\,\underset{\sim}{c} + \underset{\sim}{R}_{uo}\,\underset{\sim}{w}_o \qquad (4.61)$$

$$f_o = -\underset{\sim}{r}_{duo}^{H}\,\underset{\sim}{w}_o - \underset{\sim}{w}_o^{H}\,\underset{\sim}{r}_{duo} + \underset{\sim}{w}_o^{H}\,\underset{\sim}{R}_{uo}\,\underset{\sim}{w}_o \qquad (4.62)$$

$$\underset{\sim}{g} = \underset{\sim}{g}_o + t_e\,\dot{\underset{\sim}{g}}_o + \frac{1}{2!}t_e^2\,\ddot{\underset{\sim}{g}}_o + \cdots \qquad (4.63)$$

$$\underset{\sim}{g} = -\underset{\sim}{r}_{du} + \frac{1}{2}\underset{\sim}{R}_u\,\underset{\sim}{c} + \underset{\sim}{R}_u\,\underset{\sim}{w}_o \qquad (4.64)$$

$$f_i = f_o + \frac{1}{2!}t_e\,\dot{f}_o + \frac{1}{3!}t_e^2\,\ddot{f}_o + \cdots \qquad (4.65)$$

$$\underset{\sim}{g}_i = \underset{\sim}{g}_o + \frac{1}{2!}t_e\,\dot{\underset{\sim}{g}}_o + \frac{1}{3!}t_e^2\,\ddot{\underset{\sim}{g}}_o + \cdots \qquad (4.66)$$

We may also define another quantity,

$$f = f_o + t_e\,\dot{f}_o + \frac{1}{2!}t_e^2\,\ddot{f}_o + \cdots \qquad (4.67)$$

$$f = \nabla_t(t_s)\,\big|_{\underset{\sim}{c}=0} \qquad (4.68)$$

The convergence of the series in Equations (4.65) and (4.67) can be easily demonstrated computationally. First, the series for the vector $\underset{\sim}{g}$, and the scalar f about t_o (in Equation (4.63) and (4.67)) can be compared to the expressions for $\underset{\sim}{g}$ and f evaluated at t_s (in Equations (4.64) and (4.68)). If the difference in Equation (4.63) and (4.64) for finite number of terms or the difference between Equations (4.67) and (4.68) for finite number of terms is sufficiently small then (4.63) and (4.67) may be said to have converged. Therefore, Equations (4.65) and (4.66) (for f_i and $\underset{\sim}{g}_i$) have converged sufficiently since those series converge more rapidly than Equation (4.63) or (4.67). In

(4.58) and (4.59) we have the gradients as functions of the weight error vector and the sampling error. The only problem is that the weight error vector $\underset{\sim}{c}$ appears twice in (4.59) and cannot be factored. One way of avoiding this problem is to separate the weight gradient vector $\underset{\sim}{\nabla}_w$ into real and imaginary components, so that we obtain a joint gradient vector in matrix form as,

$$\begin{bmatrix} Re[\underset{\sim}{\nabla}_w] \\ Im[\underset{\sim}{\nabla}_w] \\ \nabla_t \end{bmatrix} = \begin{bmatrix} 2Re[\underset{\sim}{R}_{ui}] & -2Im[\underset{\sim}{R}_{ui}] & 2Re[\underset{\sim}{g}_i] \\ 2Im[\underset{\sim}{R}_{ui}] & 2Re[\underset{\sim}{R}_{ui}] & 2Im[\underset{\sim}{g}_i] \\ 2Re[\underset{\sim}{g}^H] & -2Im[\underset{\sim}{g}^H] & f_i \end{bmatrix} \begin{bmatrix} Re[\underset{\sim}{c}] \\ Im[\underset{\sim}{c}] \\ t_e \end{bmatrix} \tag{4.69}$$

Equation (4.69) may be written in the more compact form,

$$\underset{\sim}{\nabla}_p = \underset{\sim}{R}_p \, \underset{\sim}{p} \tag{4.70}$$

where $\underset{\sim}{\nabla}_p$, $\underset{\sim}{R}_p$ and $\underset{\sim}{p}$ are given by the corresponding quantities in Equation (4.69) and also are as defined in Equation (4.47).

The matrix $\underset{\sim}{R}_p$ is a weak function of the weight error vector $\underset{\sim}{c}$ in the off diagonal elements of the last row column, but is a real symmetric matrix over all values of $\underset{\sim}{c}$ for $t_e = 0$. $\underset{\sim}{R}_p$ is a stronger function of t_e as is evident from,

$$\underset{\sim}{R}_p = \underset{\sim}{R}_{ro} + \underset{\sim}{R}_{so} + t_e \underset{\sim}{R}_{so} \underset{\sim}{D}_1 + \frac{1}{2!} t_e^2 \underset{\sim}{R}_{so} \underset{\sim}{D}_2 + \cdots \tag{4.71}$$

where

$$\underset{\sim}{R}_{ro} = \begin{bmatrix} Re[\underset{\sim}{R}_{uo}] & -Im[\underset{\sim}{R}_{uo}] & \underset{\sim}{0} \\ Im[\underset{\sim}{R}_{uo}] & Re[\underset{\sim}{R}_{uo}] & \underset{\sim}{0} \\ \underset{\sim}{0}^T & \underset{\sim}{0}^T & 0 \end{bmatrix} \tag{4.72}$$

$$\underset{\sim}{R}_{so} = \begin{bmatrix} Re[\underset{\sim}{R}_{uo}] & -Im[\underset{\sim}{R}_{uo}] & 2Re[\underset{\sim}{g}_o] \\ Im[\underset{\sim}{R}_{uo}] & Re[\underset{\sim}{R}_{uo}] & 2Im[\underset{\sim}{g}_o] \\ 2Re[\underset{\sim}{g}_o^T] & 2Im[\underset{\sim}{g}_o^T] & f_o \end{bmatrix} \tag{4.73}$$

$$\underset{\sim}{D}_i = \begin{bmatrix} \underset{\sim}{I} & \underset{\sim}{0} \\ \underset{\sim}{0} & \frac{1}{i+1} \end{bmatrix} \tag{4.74}$$

Note that $\underset{\sim}{R}_{ro}$, $\underset{\sim}{R}_{so}$ and all derivatives of $\underset{\sim}{R}_{so}$ are real symmetric matricies. Each term in the series expansion of $\underset{\sim}{R}_p$ of Equation (4.71) associated with powers of t_e greater than zero, (i.e. $\underset{\sim}{R}_{so} \underset{\sim}{D}_1$, $\underset{\sim}{R}_{so} \underset{\sim}{D}_2$, ...) is similar to, by a similarity transformtion, a real symmetric matrix. However, it has not been determined if any use can be made of this fact. Also, we have not analytically determined what range of timing errors ($t_e \neq 0$ in Equation (4.71)) can be used to find algorithm stability requirements, using an approach such as we have taken.

Let us proceed now with further analyses for the case of any weight error vector $\underset{\sim}{c}$ for $t_e=0$. Equation (4.47) can be transformed to,

$$\underset{\sim}{Q}\,\underset{\sim}{p}(k+1) = [\,\underset{\sim}{I} - \mu\,\underset{\sim}{\Lambda}\,]\,\underset{\sim}{Q}\,\underset{\sim}{p}(k) \tag{4.75}$$

where

$$\underset{\sim}{\Lambda} = \underset{\sim}{Q}\,\underset{\sim}{R}_{po}\,\underset{\sim}{Q}^T \tag{4.76}$$

$$\underset{\sim}{R}_{po} = \underset{\sim}{R}_p \mid t_e = 0 \tag{4.77}$$

Λ is a diagonal matrix with diagonal elements being the eigenvalues of $\underset{\sim}{R}_{po}$ and $\underset{\sim}{R}_{ro}$

$\underset{\sim}{Q}$ is an orthogonal matrix (i.e. $\underset{\sim}{Q}\,\underset{\sim}{Q}^T = \underset{\sim}{I}$)

For stability or convergence of the steepest descent algorithm the step size μ must satisfy the following relation [68]:

$$0 < \mu < \frac{2}{\lambda_{max}} \tag{4.78}$$

where λ_{max} is the maximum eigenvalue. Also, the overall time constant (including all tap-weight) of the steepest descent algorithm is given by Griffiths [68] as,

$$\frac{T}{-\ln(1-\mu\lambda_{max})} \le \tau_a \le \frac{T}{-\ln(1-\mu\lambda_{min})} \tag{4.79}$$

where λ_{min} is the smallest eigenvalue

τ_a is the overall time constant

T is the time period of one iteration of the algorithm.

In a subsequent section, Equations (4.78) and (4.79) will be used in a discussion of the eigenvalues calculated for a 5 forward and 5 backward tap DFE with jointly adaptive sampling in the presence of multipath fading.

4.5 LMS and Quantitized Gradient Algorithms

If initially we do not know the autocorrelation matrix and cross-correlation vector, or if the statistics are slowly time varying, then it is desired to base an adaptive system on estimated gradients which are either instantaneous estimates or are time averaged over a short time relative to the time variance of the statistics of the channel.

The Least Mean Squares (LMS) algorithm, first developed by Widrow[68], uses instantaneous estimates of $\underset{\sim}{r}_{du}$ and $\underset{\sim}{R}_u$ in phase of $\underset{\sim}{r}_{du}$ and $\underset{\sim}{R}_u$ in the steepest descent algorithm. The instantaneous tap-weight gradient [68] is given by,

$$\hat{\underset{\sim}{\nabla}}_w(n) = -d(n)\, \underset{\sim}{u}^*(n) + \underset{\sim}{u}^*(n)\, \underset{\sim}{u}^T(n)\, \underset{\sim}{w}(n)$$

$$= \underset{\sim}{u}^*(n)\, e(n) \qquad (4.80)$$

where

$$\underset{\sim}{\nabla}_w = E[\hat{\underset{\sim}{\nabla}}_w(n)] \qquad (4.81)$$

An instantaneous estimate of the sampling gradient is [42],

$$\begin{aligned}
\nabla_t &= -[\, d(n)\, \underset{\sim}{u}^*(n)\,]^H\, \underset{\sim}{w}(n) - \underset{\sim}{w}^H(n)\, [\, d(n)\, \underset{\sim}{u}^*(n)\,] \\
&\quad + \underset{\sim}{w}^H(n)\, [\, \underset{\sim}{u}^*(n)\, \underset{\sim}{u}^T(n) + \underset{\sim}{u}^*(n)\, \underset{\sim}{u}^T(n)\,]\, \underset{\sim}{w}(n) \\
&= -[\, d^*(n) + \underset{\sim}{w}^H(n)\, \underset{\sim}{u}^*(n)\,]\, \underset{\sim}{u}^T(n)\, \underset{\sim}{w}(n) \\
&\quad + [\, \underset{\sim}{u}^T(n)\, \underset{\sim}{w}(n)\,]^*\, [\, -d(n) + \underset{\sim}{u}^T(n)\, \underset{\sim}{w}(n)\,] \\
&= e^*(n)\, z(n) + e(n)\, z^*(n) \\
&= 2\,\mathrm{Re}[\, z^*(n)\, e(n)\,]
\end{aligned} \tag{4.82}$$

where

$$z(n) = \underset{\sim}{u}^T(n)\, \underset{\sim}{w}(n) \tag{4.83}$$

and

$$\nabla_t = E[\hat{\nabla}_t(n)] \tag{4.84}$$

The LMS algorithm is referred to as a stochastic algorithm since the MSE and the tap-weights become non-stationary random variables. However, the stability of the LMS algorithm for tap-weight adjustment has been determined. For $E[w(n)]$ to converge the step size μ is restricted to [68],

$$0 < \mu < \frac{2}{\lambda_{max}} \tag{4.85}$$

For $E[J(n)]$ to converge the step-size μ is restricted to[68],

$$0 < \mu < \frac{2}{\sum_i \lambda_i} \tag{4.86}$$

where λ_i are the eigenvalues of the autocorrelation matrix $\underset{\sim}{R}_u$.

The effort required to extend the stability analysis of the joint tap-weight and sampling phase adaptation from the steepest descent algorithm to the LMS algorithm has not been determined, partly, because the system as implemented does not use the LMS algorithm. Instead, the system implemented uses an extension of a quantized adaptive method first suggested by Lucky[39] which may be expressed for, $j = 1, \ldots, M+N$

$$\mathrm{Re}[w_{x,j}(n_{x,j}+K_{x,j})] = \mathrm{Re}[w_{x,j}(n_{x,j})] - \Delta\, \mathrm{sgn}\Big(\sum_{i=n_{x,j}}^{n_{x,j}+K_{x,j}} \mathrm{sgn}[\mathrm{Re}[u_{d,j}(i-M)]]\ \mathrm{sgn}[\mathrm{Re}[e(i-M)]] \Big) \tag{4.87a}$$

$$\mathrm{Re}[w_{y,j}(n_{y,j}+K_{y,j})] = \mathrm{Re}[w_{y,j}(n_{y,j})] - \Delta\, \mathrm{sgn}\Big(\sum_{i=n_{y,j}}^{n_{y,j}+K_{y,j}} \mathrm{sgn}[\mathrm{Im}[u_{d,j}(i-M)]]\ \mathrm{sgn}[\mathrm{Im}[e(i-M)]] \Big) \tag{4.87b}$$

$$\mathrm{Im}[w_{x,j}(n_{u,j}+K_{u,j})] = \mathrm{Im}[w_{x,j}(n_{u,j})] \tag{4.87c}$$

$$- \Delta \,\mathrm{sgn}\Big(\sum_{i=n_{u,j}}^{n_{u,j}+K_{u,j}} \mathrm{sgn}[\mathrm{Im}[u_{d,j}(i-M)]]\ \mathrm{sgn}[\mathrm{Re}[e(i-M)]] \Big)$$

$$\mathrm{Im}[w_{y,j}(n_{v,j}+K_{v,j})] = \mathrm{Im}[w_{y,j}(n_{v,j})] \tag{4.87d}$$

$$- \Delta \,\mathrm{sgn}\Big(\sum_{i=n_{v,j}}^{n_{v,j}+K_{v,j}} \mathrm{sgn}[-\mathrm{Re}[u_{d,j}(i-M)]]\ \mathrm{sgn}[\mathrm{Im}[e(i-M)]] \Big)$$

$$t_s(n_s+K_s) = t_s(n_s) \tag{4.87e}$$

$$- \Delta_s \,\mathrm{sgn}\Big(\sum_{i=n_s}^{n_s+K_s} \mathrm{sgn}[\mathrm{Re}[z(i)]]\ \mathrm{sgn}[\mathrm{Re}[e(i)]] \Big)$$

where

- $w_{x,j}$ is the j-th element of a complex tap-weight vector $\underset{\sim}{w}_x$
- $w_{y,j}$ is the j-th element of a complex tap-weight vector $\underset{\sim}{w}_y$
- $u_{d,j}$ is the j-th element of the complex data vector defined in Equation (4.92)
- e is the error defined in Equation (4.3)
- Δ is the quantization distance
- $n_{x,j}$ is the sample time of the update of the j-th on-axis tap-weight $\mathrm{Re}[w_{x,j}]$ affecting the I-axis error
- $K_{y,j}$ is the number of samples taken between updates of the j-th on-axis tap-weight $\mathrm{Re}[w_{y,j}]$ affecting the Q-axis error $\mathrm{Im}[e]$

The tap-weight vectors $\underset{\sim}{w}_x$ and $\underset{\sim}{w}_y$ are defined by the tap-weight vector $\underset{\sim}{w}$ for the special case of the modulator, demodulator, and baseband portion of the system being ideal, as follows,

$$\underset{\sim}{w}_x = \underset{\sim}{w} \tag{4.88a}$$

$$\mathrm{Re}[\underset{\sim}{w}_y] = \mathrm{Re}[\underset{\sim}{w}] \tag{4.88b}$$

$$\mathrm{Im}[\underset{\sim}{w}_y] = -\mathrm{Im}[\underset{\sim}{w}] \tag{4.88c}$$

where the number of counts between tap-weight adjustments are defined as

$$K_{x,j} = U_{x,j} + D_{x,j} \tag{4.89a}$$

$$K_{y,j} = U_{y,j} + D_{y,j} \tag{4.89b}$$

$$K_{u,j} = U_{u,j} + D_{u,j} \tag{4.89c}$$

$$K_{v,j} = U_{v,j} + D_{v,j} \tag{4.89d}$$

$$K_s = U_s + D_s \tag{4.89e}$$

such that

$$U_{x,j} - D_{x,j} = \pm C \tag{4.90a}$$

$$U_{y,j} - D_{y,j} = \pm C \tag{4.90b}$$

$$U_{u,j} - D_{u,j} = \pm C \tag{4.90c}$$

$$U_{v,j} - D_{v,j} = \pm C \tag{4.90d}$$

$$U_s - D_s = \pm C \tag{4.90e}$$

where

$U_{u,j}$ is the number of up-counts of an up-down counter between adjustment of the j-th cross-axis tap-weight $\mathrm{Im}[w_{x,j}]$ affecting the I-axis error $\mathrm{Re}[e]$

$D_{y,j}$ is the number of up-counts of an up-down counter between adjustment of the j-th cross-axis tap-weight $Im[w_{y,j}]$ affecting the Q-axis error Im[e]

2C is the up-down counter size as described in Chapter 3

If it is desired to consider a linear tap-weight adaptation which is based on the decisions (quantitizer outputs) but is otherwise the same as the LMS algorithms then we write,

$$\underset{\sim}{w}(n+1) = \underset{\sim}{w}(n) - \mu \, \underset{\sim}{u}_d^*(n-M) \, e(n-M) \tag{4.91}$$

where
$$\underset{\sim}{u}_d(n) = \begin{bmatrix} d(n+M-1) \\ \vdots \\ d(n) \\ \vdots \\ d(n-N) \end{bmatrix}_{N+M\times 1} \tag{4.91a}$$

The delay of M samples is included in Equation (4.91) so that data decisions can be used as estimates of the desired response. We will continue to assume that the data decisions are correct estimates of the desired response. This is necessary in order to ensure that the surface on which adaptation is converging remains convex with respect to tap-weight variation. In practical terms it means that the decisions must be in error no more than 10% of the time[71]. By taking the expectation of Equation (4.91) and assuming independence between the data vector $\underset{\sim}{u}$ and the tap-weight vector $\underset{\sim}{w}$ we have,

$$E[\underset{\sim}{w}(n+1)] = E[\underset{\sim}{w}(n)] - \mu [-\underset{\sim}{r}_{dud} + \underset{\sim}{R}_{dud} E[\underset{\sim}{w}(n)]] \tag{4.92}$$

where
$$\underset{\sim}{r}_{dud} = E[\underset{\sim}{u}_d^*(n)\, d(n)]$$
$$\underset{\sim}{R}_{dud} = E[\underset{\sim}{u}_d^*(n)\, \underset{\sim}{u}^T(n)] \tag{4.93}$$

For the DFE case with independent desired response samples,

$$\underset{\sim}{R}_{dud} = \begin{bmatrix} \underset{\sim}{R}_{dfu} & \underset{\sim}{0} \\ \underset{\sim}{R}_{fb}^H & \underset{\sim}{R}_{bb} \end{bmatrix} \tag{4.94}$$

$$\underset{\sim}{r}_{dud} = \begin{bmatrix} 0 \\ \cdot \\ \cdot \\ 0 \\ r_d(0) \\ 0 \\ \cdot \\ \cdot \\ 0 \end{bmatrix} \tag{4.95}$$

where $\underset{\sim}{R}_{dfu}$ is a Hermitian MxM matrix

$\underset{\sim}{R}_{fb}$ is the same MxN matrix as defined in Equation (4.17)

$\underset{\sim}{R}_{bb}$ is the same NxN matrix as defined in Equation (4.17)

$r_d(0)$ is the M-th non-zero element of $\underset{\sim}{r}_{dud}$

After convergence of the expectation of $\underset{\sim}{w}$ we then have,

$$\underset{\sim}{w}_o = \underset{\sim}{R}^{-1}_{dud}\, \underset{\sim}{r}_{dud} \tag{4.96}$$

or

$$\underset{\sim}{a}_o = \underset{\sim}{R}^{-1}_{dfu}\, \underset{\sim}{r}_{dfu} \tag{4.97}$$

$$\underset{\sim}{b}_o = \frac{-1}{r_d(0)}\, \underset{\sim}{R}^{H}_{fb}\, \underset{\sim}{a}_o \tag{4.98}$$

where $\underset{\sim}{w}_o$ is the expectation of $\underset{\sim}{w}(n)$ after convergence,

and

$$\underset{\sim}{r}_{dud} = \begin{bmatrix} \underset{\sim}{r}_{dfu} \\ \underset{\sim}{r}_{dbu} \end{bmatrix} \tag{4.100}$$

The important result here is that the forward and backward tap-weights are both determined by the cross-correlation function of Equation (4.24) in a simpler form than the LMS algorithm. The additional simplicity is expected to improve adaptation time as demonstrated by Lucky [39] and George [38] but at the expense of MSE performance at low SNR's. This algorithm is referred to as the zero forcing (ZF) algorithm because of the direct dependence of the forward and backward taps on the channel impulse response, such that the algorithm "forces zero's" in the overall equalized impulse response.

At high SNR values, the two algorithms have been shown to be essentially identical [36], and thus in the present analysis we consider the LMS type of algorithm in order to allow a straight-forward determination of system eigenvalues.

Gersho [72] has analysed a quantitized steepest descent (non-stochastic) algorithm of the following type,

$$\underset{\sim}{w}(n+1) = \underset{\sim}{w}(n) - \Delta \, \mathrm{sgn}[\nabla_{\underset{\sim}{w}}] \tag{4.101}$$

where Δ is the distance between quantization levels of $\underset{\sim}{w}$ Gersho proved that the cost function (MSE) converges to some desired region such that,

$$J_{min} < J < J_{min}+\varepsilon_o . \tag{4.101a}$$

if Δ is sufficiently small and bounded by,

$$\Delta_{max} = \frac{1}{3(N+M)} \left(\frac{\lambda_{min}}{\lambda_{max}} \right) \left(\frac{2\,\varepsilon_o}{\lambda_{max}} \right)^{1/2} \tag{4.102}$$

Also from Gersho[72], the mean number of iterations necessary to achieve convergence can be shown to be proportional to

$$\left(\frac{\lambda_{max}}{\lambda_{min}} \right)^2$$

In the next section we will examine the eigenvalues calculated for the joint tap-weight and sampling phase adaptive system. Some of the relations presented in this section will be used to discuss the possible performance of the adaptive system.

4.6 Eigenvalues versus Multipath

The eigenvalues of the joint adjustment matrix $\underset{\sim}{R}_p$ have been calculated as a function of a two ray multipath model for atmospheric multipath. This model can be related to Rummler's model and is,

$$H_p(f) = a\ (\ 1 - b\ \exp(-j2\pi(f-f_o)\tau)\ ) \qquad (4.103)$$

where a is due to a flat fading component of multipath

b is the relative amplitude between two rays and may be greater than one

f_o is the frequency offset of the minimum in $H_p(f)$ from zero frequency as defined in Chapter 1

τ is the relative delay difference between the first and second ray

The main difference between this model and Rummler's model is that the the relative amplitude b in this model is allowed to be greater than one. This is necessary in physical situations to allow for transitions between MP and NMP fades. Now, the relation between the model expressed in Equation 1.03 and Rummler's model expressed in Equation 1.1 is given.

In the region $0 < b < 1$

$$H_p(f) = H_o(f) \qquad (4.103a)$$

$$a_o = a \qquad (4.103b)$$

$$b_o = b \qquad (4.103c)$$

In the region $1 < b$

$$H_p(f) = a\, b\, \left(\frac{1}{b} - \exp(-j2\pi(f-f_o)\tau) \right) \qquad (4.103d)$$

$$= -a\, b\, \left(1 - \frac{1}{b} \exp(+j2\pi(f-f_o)\tau) \right) \exp(-j2\pi(f-f_o)\tau)$$

Now, in the region $1 < b$ if we let

$$b_o = \frac{1}{b} \qquad (4.103e)$$

$$a_o = a\, b \qquad (4.103f)$$

then

$$H_p(f) = -H_o(f) \exp(-j2\pi(f-f_o)\tau) \qquad (4.103g)$$

also

$$B = -20 \log_{10}(1-b) \quad b < 1 \qquad (4.103h)$$

$$B = -20 \log_{10}(b-1) \quad b > 1 \qquad (4.103i)$$

$$D_m = 20 \log_{10}\left(\frac{1+b}{1-b}\right) \quad b < 1 \qquad (4.103j)$$

$$D_m = 20 \log_{10}\left(\frac{b+1}{b-1}\right) \quad b > 1 \qquad (4.103k)$$

$$B_o = -20 \log_{10}(1-b_o) \qquad \text{(repeat of 1.3)}$$

where B is the notch depth below the reference value at

$b = 0$ and $a = 1$

D_m is the peak to peak amplitude ratio

Note that for b greater than two, the notch depth B becomes negative, while the peak to peak amplitude ratio D grows smaller.

Empirical probability distributions have been obtained [73] for a_o, b_o and f_o with the relative delay τ

fixed to a constant of 6.3ns. These distributions are used in estimating the probability of outage (bit error rate less than 10^{-3}) when the outage performance versus the model parameters of the particular equipment being used are known. Since it is primarily desired to examine the adaptive system performance with respect to multipath for the high SNR case, and because we will be dealing with transitions between MP and NMP, the system eigenvalues are examined versus model parameters b and f_o.

The autocorrelation function and cross-correlation functions referred to in Equations (4.24) and (4.25) are calculated from the impulse response of the received signal. The received signal impulse response $h_r(t)$ is,

$$h_r(t) = a\, h_f(t) - a\, b\, h_f(t) \exp(2\pi f_o \tau) \quad (4.104)$$

where

$$h_f(t) = h_t(t) + h_t(t-T) \quad (4.105)$$

$$h_t(t) = \mathrm{sinc}\left(\frac{t}{T}\right) \exp\left(-\left(\frac{\pi t}{\tau_g}\right)^2\right) \quad (4.106)$$

τ_g is the half amplitude time period of the Gaussian pulse

Gaussian weighting of the transmitted impulse response provides an impulse response which is closer to that which could be obtained with practical filters, although no attempt was made to duplicate the response of the implemented system. It was found that the half amplitude pulse width is critical in determining the system performance for off band centre fading (f_o around 10 to 12 MHz and b around 1). This will be discussed further in subsequent paragraphs. Also, a constant level of noise was added to the signal before the signal plus noise was multiplied to obtain a constant signal power level at the equalizer input, just as an ideal AGC amplifier would do, so that the SNR of an ideal channel (no fading) was equal to 67dB. Figure 4.10 shows this ideal AGC gain versus the multipath relative amplitude b. Since this gain in Figure 4.10 is dependent only on the signal level, it is also the relative reduction in SNR versus the multipath relative amplitude b for various frequency notch offsets f_o.

The optimum tap-weight vector and optimum sampling instant t_o were found using the normal Equations (4.30) and (4.31) and the recursive Equation (4.44). In Figure 4.2, which is a plot of optimum sampling instant versus the multipath relative amplitude b, it can be seen that t_o is multi-valued in the region between b=1 and b=2 for frequency offsets of 0, 5, and 10 MHz. This is due to the fact that there are minima of the MSE that are spaced at approximately symbol period intervals in time and the effect of the multipath as b is varied from 0 to 2 (for a system initially acquired at a b of 0) is to cause the sampling phase to track forward by one baud. Similarly, (for a system which has initially acquired at a value of b equal to 2) as b is decreased towards 0 from 2 the sampling phase tracks

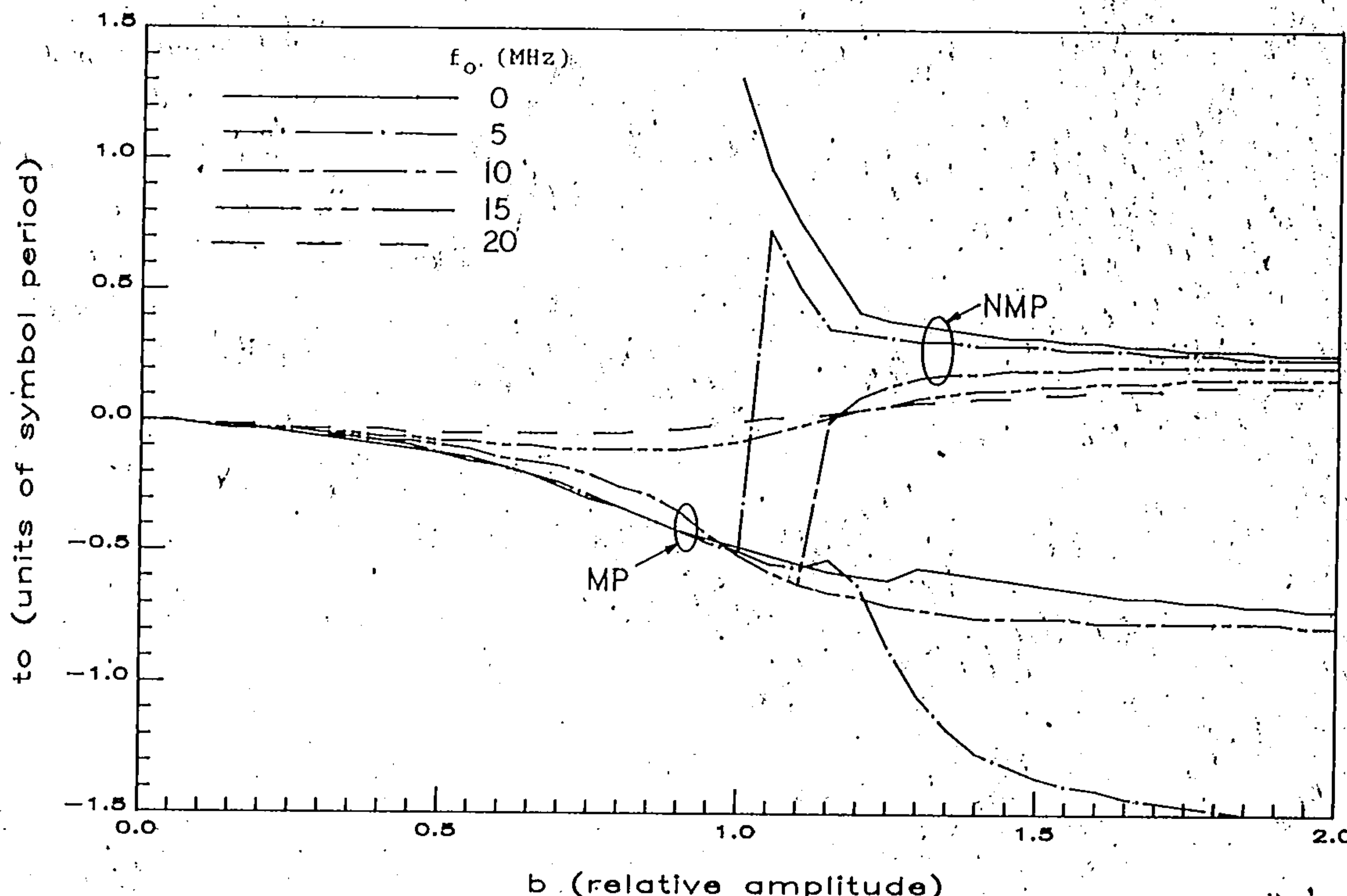

Figure 4.2 Optimum Sampling Instant versus Multipath Relative Amplitude for various Notch Frequency Offsets

backward by one baud. The locus of timing points which minimize the MSE and are obtained from a system initially acquired in the minimum phase (MP) region will be referred to as the MP locus while the locus of points which minimize the MSE and are obtained from a system initially acquired in the non-minimum phase (NMP) region will be referred to as an NMP locus. A minimum phase (MP) curve at a value of f_o in Figure 4.2 was generated as follows. Initially b was set to zero, and an initial value of zero was used for t_s until the recursion converged to t_o. Then b was incremented by .05 and the previous value t_o was used as the new initial value. This was repeated until b equalled 2. A non-minimum phase (NMP) curve for f_o between 0 and 10 MHz was generated in the same way except that b was initially equal to 2 and was decremented to 1 or until the last iteration caused a jump in t_o to the MP curve, as seen in the case for f_o equal to 5 and 10 MHz. These curves describe how the optimum sampling instant should track a variation in b for a steepest descent, LMS or other adaptive algorithm, provided that the adaptation is stable and can track the changes and that the MSE is not so large as to cause an excessive number of decision errors. The theoretical calculations and measured results were done solely with respect to changes in the two ray multipath relative amplitude b, since the changes in the adaptive system are more significant with respect to the multipath relative amplitude than the notch frequency offset. It is important to note that the NMP loci for frequency offsets of 5 and 10MHz connect to the MP loci as b is decreased, but do not connect in the reverse direction. For 0 MHz offsets, the MP sampling phase loci do not connect to the NMP sampling phase loci for b adjusted in either direction. This is explained by the fact that the MSE for the MP locus is always approximately equal to or less than the MSE for the NMP locus for frequency offsets between 0 and 10MHz as can be seen in Figure 4.3, 4.4 and 4.5.

All the results presented in this section have been calculated with the half amplitude width, τ_g of Equation (4.106), set to a value of 8T, where T is the symbol period. As it was stated earlier, the value of τ_g is critical in determining the equalizer performance for off band centre fading. Briefly, the effects of varying τ_g are now described. For τ_g greater than 8T, the MMSE becomes a monotonic increasing function of t_s for t_s in the region of -T to T and f_o in the region of 1/(2T) and b between 0.85 and 1.15. As τ_g increases the monotonic increasing region with respect to t_s widens with respect to f_o, centred about 1/(2T) and at the same time the MMSE increases over all multipath conditions. A minimum does occur in the region of t_s equal to -2T for the conditions just described, however, it is characterized by a maximum to minimum eigenvalue ratio greater than 10^7. As τ_g is decreased below 6T the eigenvalue ratio for an ideal channel (no multipath) begins to increase

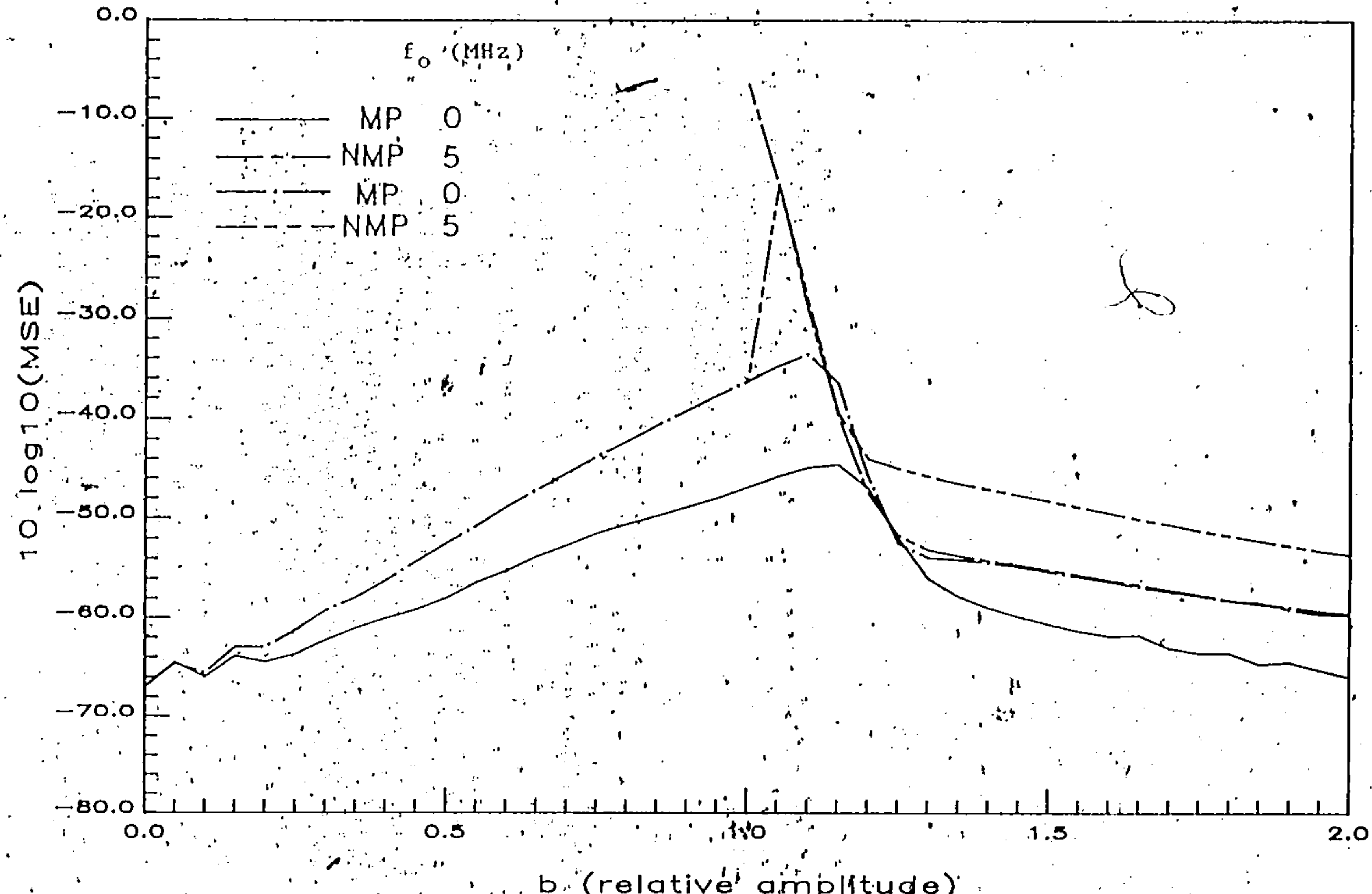

Figure 4.3 MMSE versus Multipath Relative Amplitude for various Notch Frequency Offsets

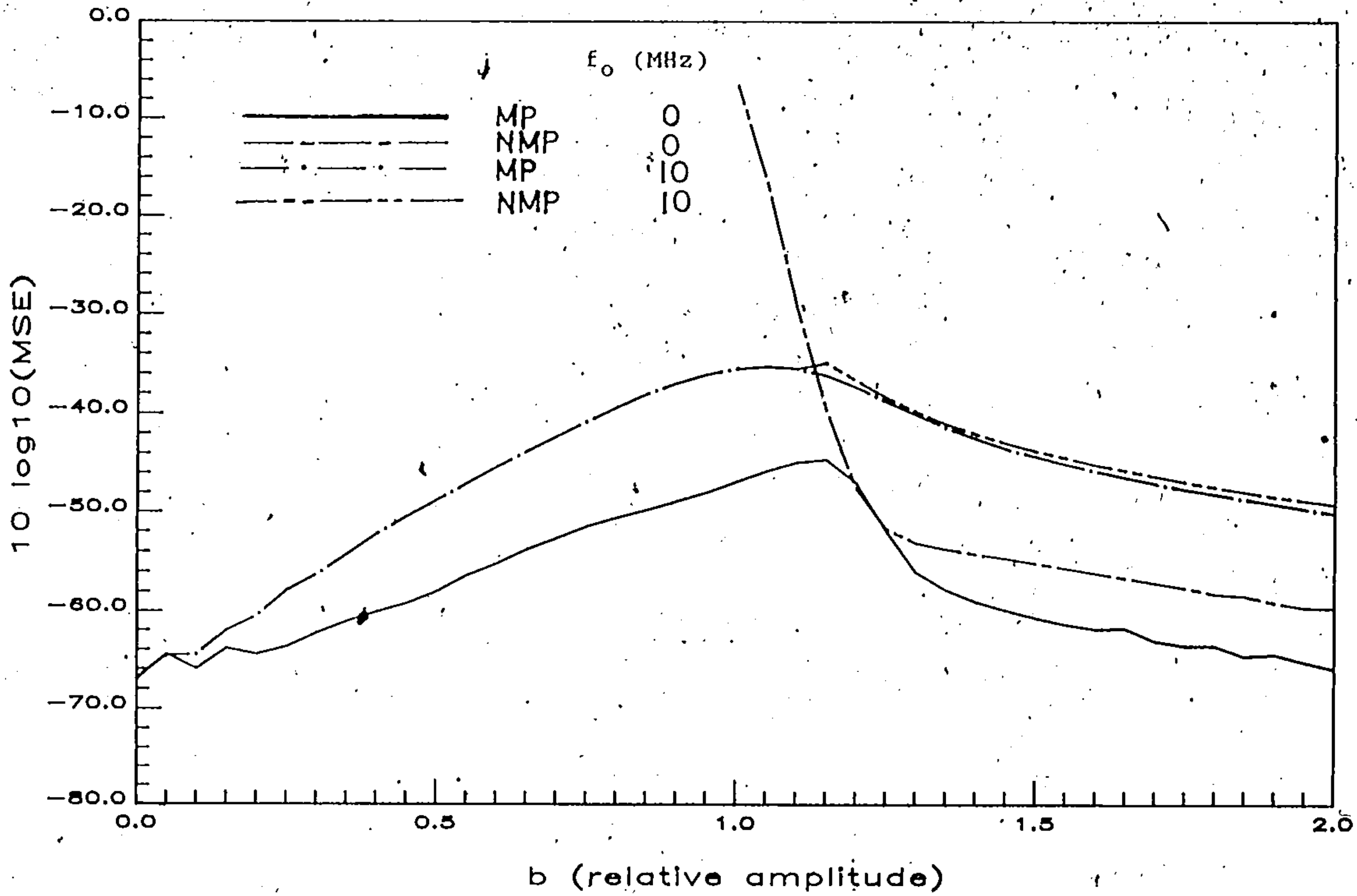

Figure 4.4 MMSE versus Multipath Relative Amplitude for various Notch Frequency Offsets

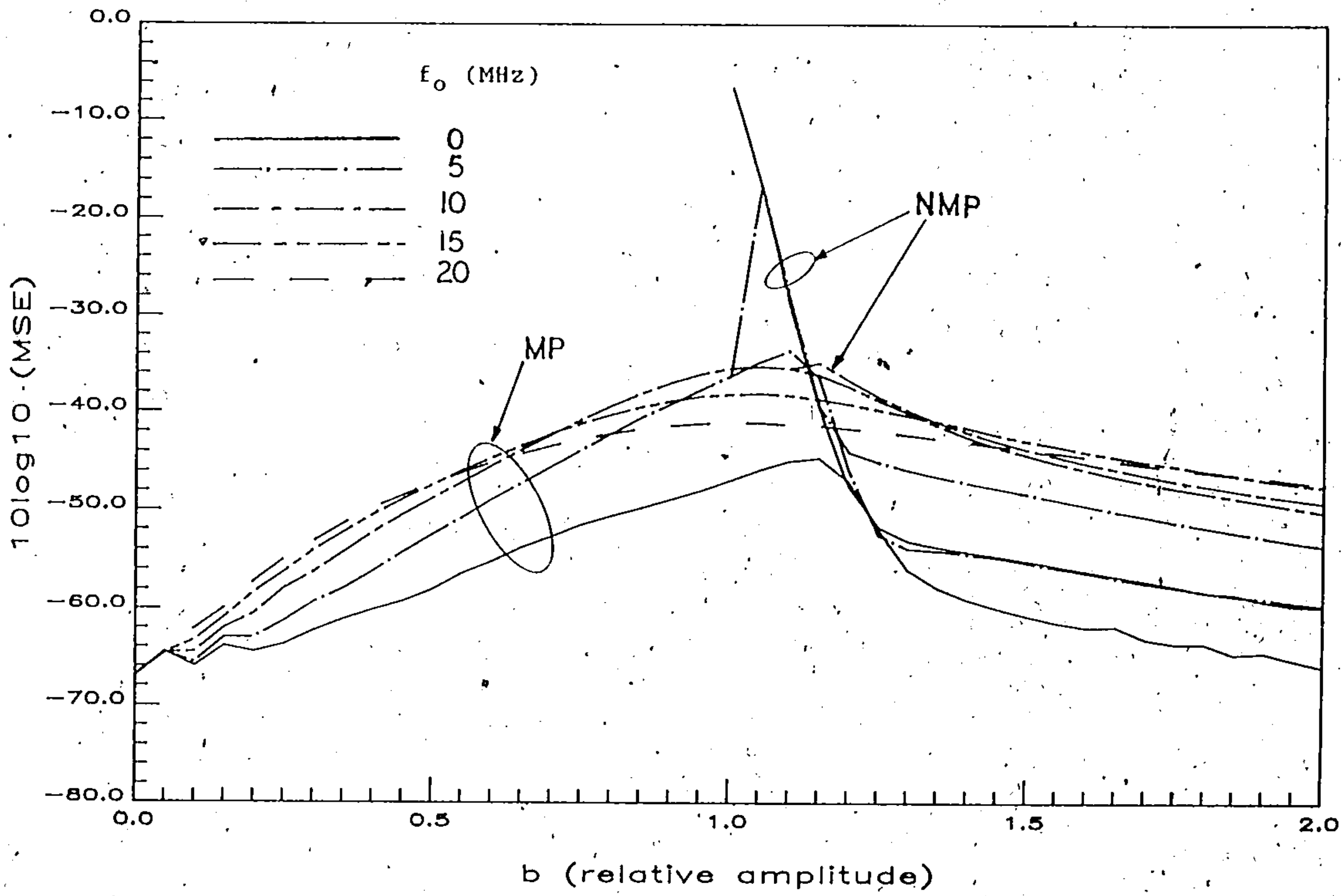

Figure 4.5 MMSE versus Multipath Relative Amplitude for various Notch Frequency Offsets

rapidly. It might be concluded from this that it is important to have an ideal channel impulse response which goes to zero over continuous time as fast as possible for time magnitude greater than the time span of the equalizer. In the frequency domain this translates to minimizing any short period (<1/(5T)) amplitude or group delay ripples and adjusting the band edge amplitude slope to be consistent with the band edge amplitude slope of the Fourier transform of Equation (4.105). This should be the subject of future work, particularly with respect to the realization of practical equipment impulse responses since it may be that the performance of equalizer could be much better with a realizable impulse response than with an impulse response based on a sinc function.

The maximum eigenvalue, the minimum eigenvalue, the ratio of the maximum to minimum eigenvalue, and the determinant of the matrix $\underset{\sim}{R}_a$ which are all calculated in the same manner as the optimum sampling instant in Figure 4.2, are presented in Figures 4.6, 4.7, 4.8, and 4.9. Since the equalizer unsampled signal input power was held constant over the multipath to simulate an AGC the sum of the eigenvalues of the adjustment matrix $\underset{\sim}{R}_p$ ranged between 60 and 100 over all values of b and f_o calculated. The sum of the eigenvalues is plotted in Figure 4.11.

By examining the MSE for the MP and NMP loci in Figures 4.3, 4.4, and 4.5 it could be concluded that only

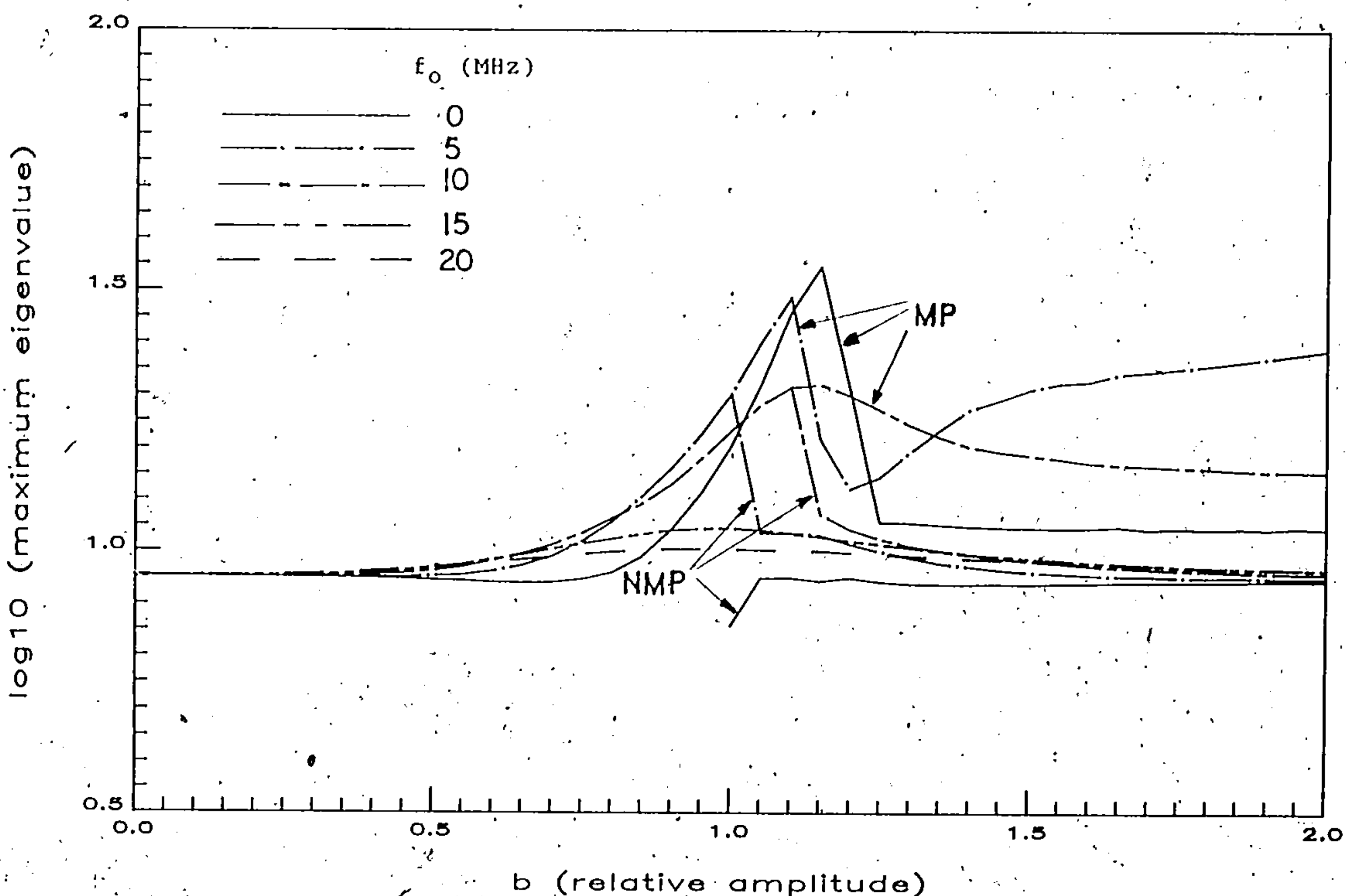

Figure 4.6 Maximum Eigenvalue of Adjustment Matrix versus Multipath Relative Amplitude for various Notch Frequency Offsets

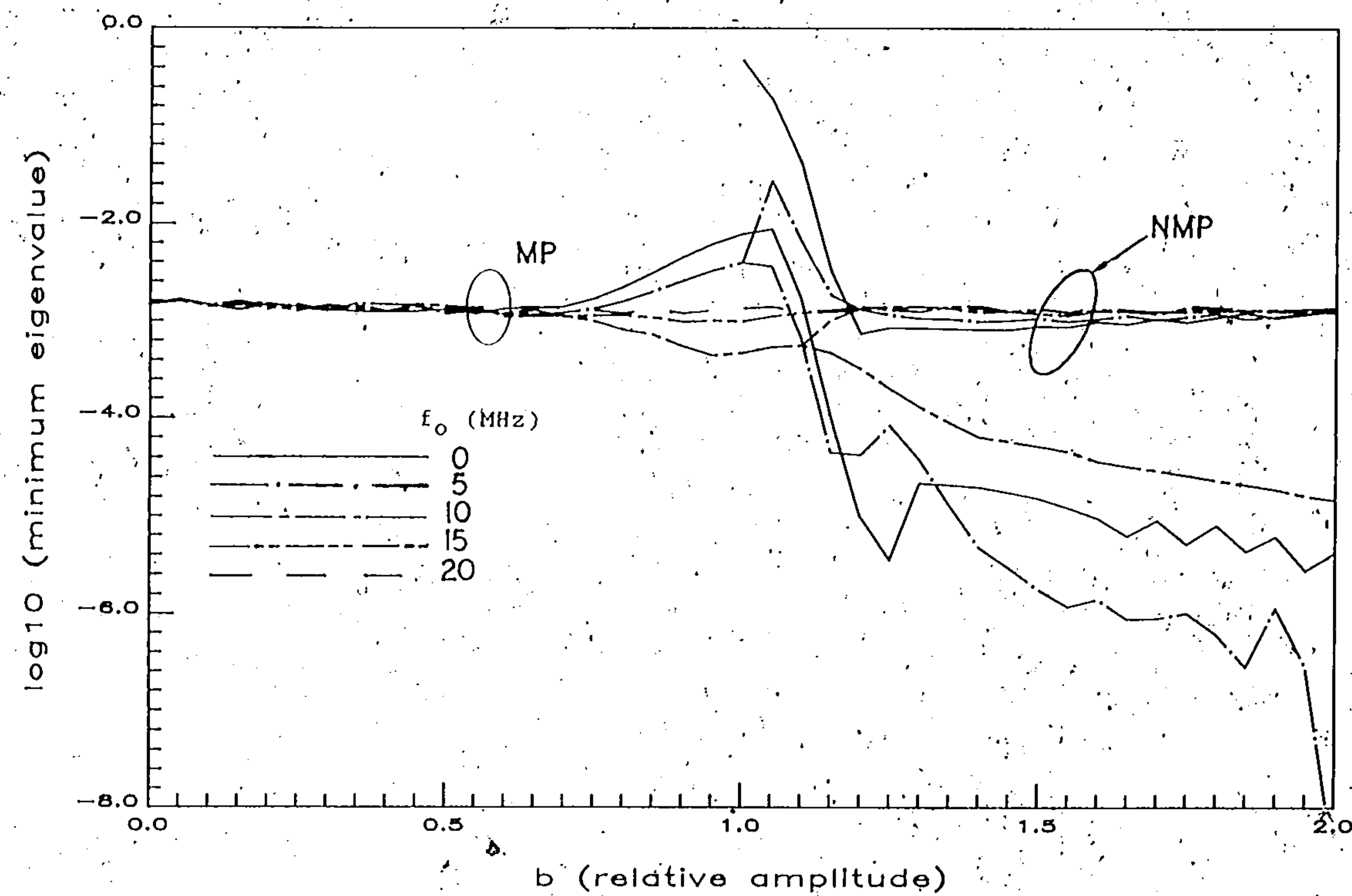

Figure 4.7 Minimum Eigenvalue of Adjustment Matrix versus Multipath Relative Amplitude for various Notch Frequency Offsets

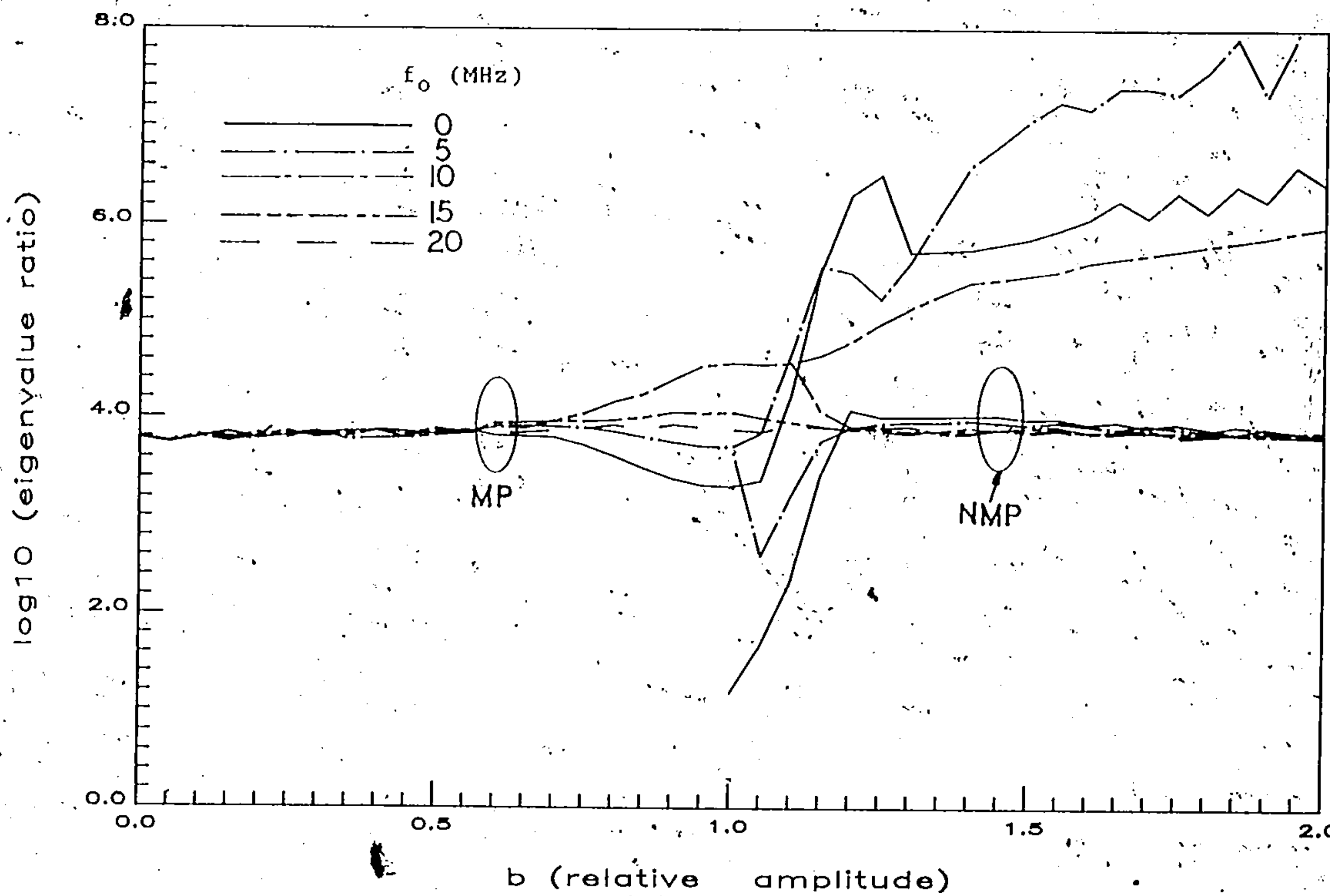

Figure 4.8 Eigenvalue Spread of Adjustment Matrix versus Multipath Relative Amplitude for various Notch Frequency Offsets

the MP loci are desirable because of the lower MSE. Also, the performance while moving from one locus to the other is liable to be poor, and this would favour staying on the MP locus. However, in Figure 4.7 it is seen that for frequency offsets of 0 and 5MHz the logarithm of the smallest eigenvalue decreases very rapidly on the MP loci as b increases above 1.05. The question of how far the various adaptive algorithms can follow the MP loci then arises. In the previous chapter it was established that an appropriate goal for the overall system time constant is approximately 1 ms. Assuming a value of 0.01 for the step size μ would ensure stability of the steepest descent method or the LMS algorithm over all the multipath parameters. Then, using Equation (4.79) gives an estimate of an upper bound on the overall time constant of the joint timing and tap-weight adaptation using the method of steepest descent. Using a value of 1 ms as an upper bound on the overall time constant implies a minimum eigenvalue no less than $10^{-2.3}$. Assuming a minimum eigenvalue of 10^{-5} implies an upper bound of .44s on the overall time constant of the steepest descent method. These results are not too encouraging. If Gersho's condition for stability of a one bit quantized steepest descent method are examined (Equation (4.92)) the results are even less encouraging. Even if 16 bit tap-weight registers were used the degree of quantization would still be too large to satisfy Equation (4.92). It should be remembered, however, that the implementation being used is a decision directed adaptation which would have different eigenvalues and which we know [38] is better in tracking. In the next chapter the calculated eigenvalues are used to qualitatively explain the observed performance of the decision directed joint adaptive system.

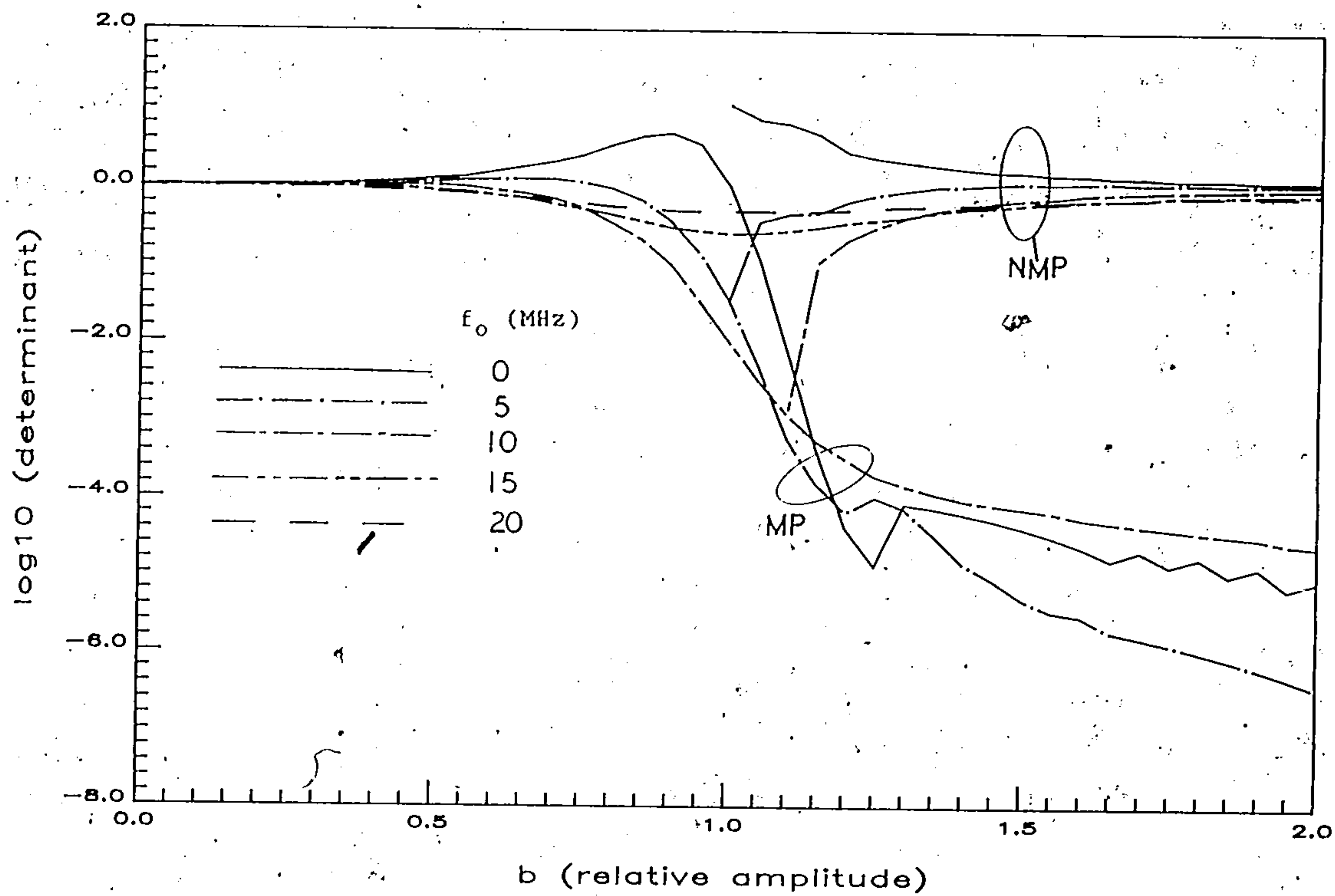

Figure 4.9 Determinant of Matrix R_a versus Multipath Relative Amplitude for various Notch Frequency Offsets

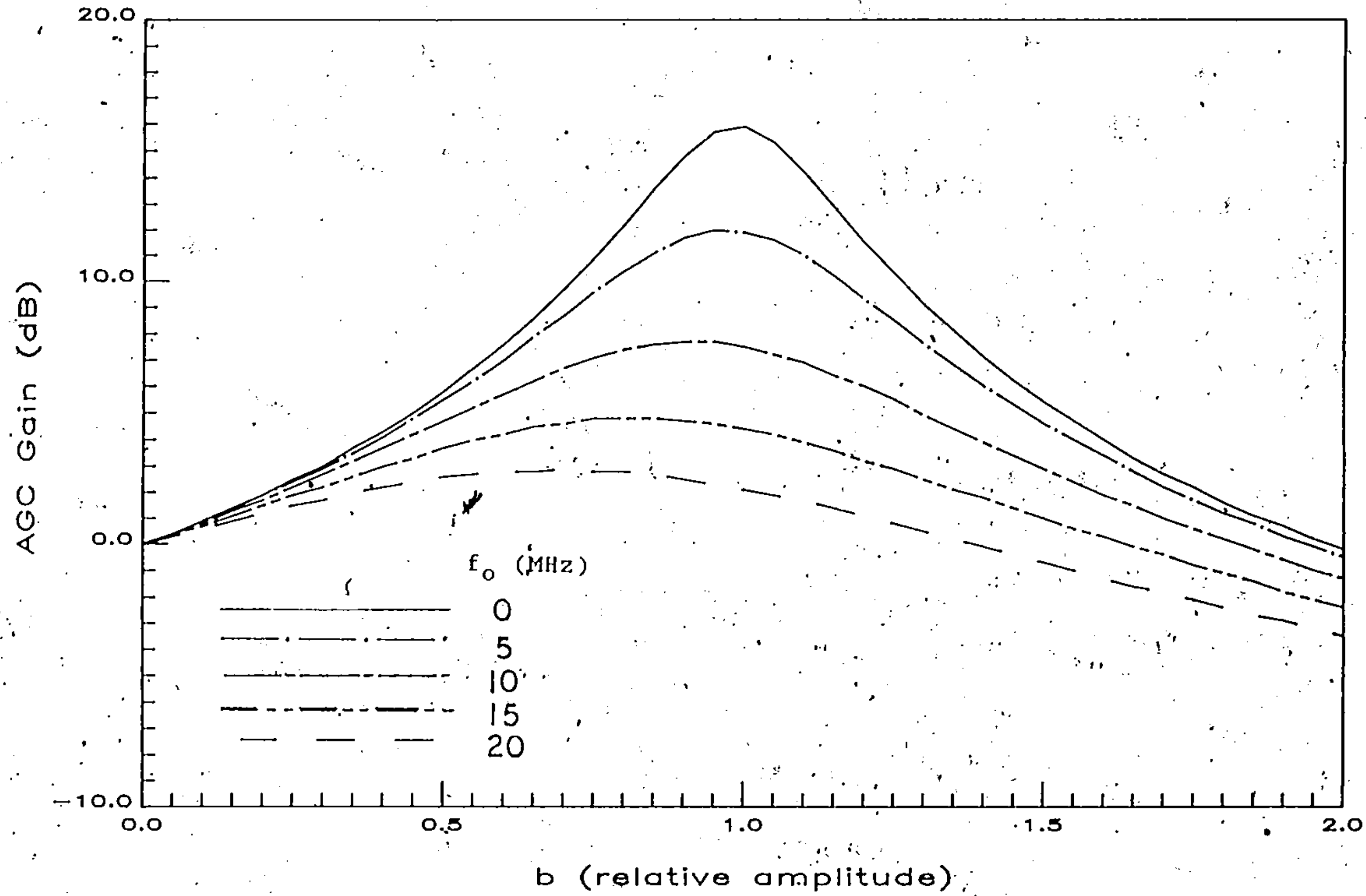

Figure 4.10 AGC Gain versus Multipath Relative Amplitude for various Notch Frequency Offsets

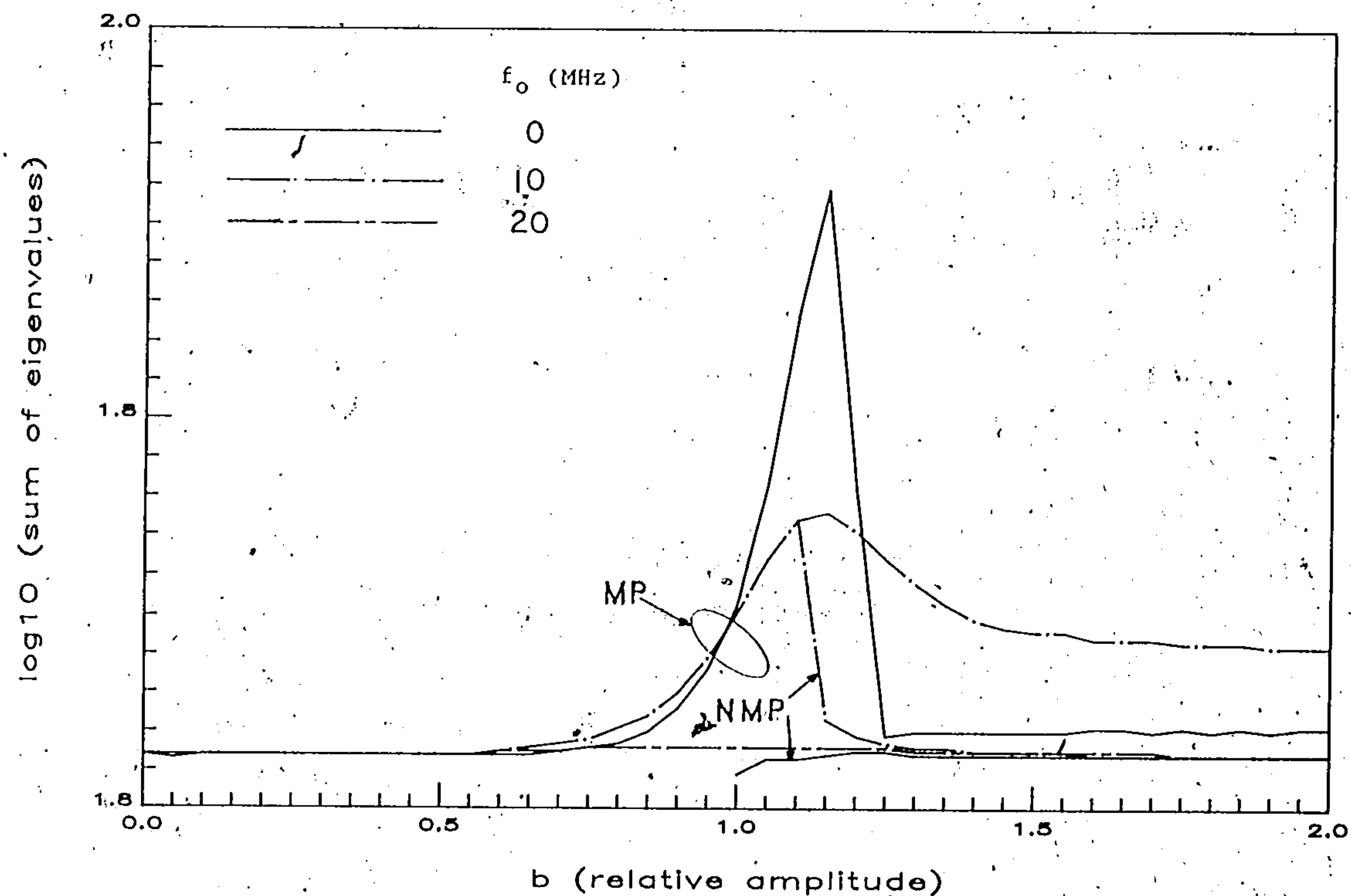

Figure 4.11 Sum of Eigenvalues of the Adjustment Matrix versus Multipath Relative Amplitude for various Notch Frequency Offsets

CHAPTER 5

EXPERIMENTAL AND THEORETICAL PERFORMANCE OF THE 490PRS RADIO SYSTEM

5.1 Introduction

In this Chapter, the following aspects of system performance will be examined:

i) Bit error rate (BER) versus the receiver signal level (RSL) at the RF filter input;

ii) BER versus the transmitter power output level;

iii) BER versus amplitude and phase imbalances in the transmitter;

iv) BER versus the two-ray multipath relative amplitude b for fading notches at mid-band;

v) receiver tracking between the minimum-phase and non-minimum phase regions of a two-ray fading model;

vi) initial acquisition performance of the tap-weights and sampling phase;

vii) examination of the measured and theoretical sampling instant versus the two-ray multipath relative amplitude b for fading notches at mid-band;

viii) comparison of the theoretical and measured outage signatures.

As stated previously, the experimental system is implemented without carrier recovery and uses a "hard-wired" carrier reference, obtained by mixing the transmitter carrier oscillator with the receiver local oscillator. This should not be a big problem with respect to evaluation of the potential performance of the DFE during multipath since it was shown in the last two chapters that the DFE tap-weights can resolve any slowly varying carrier phase error. In a working system, of course, carrier recovery is still required, but only to estimate and track any frequency offset in the received signal. The main consequence of omitting the carrier recovery function is that any performance degradation that may be experienced due to the carrier phase estimation process, is omitted from the measured performance. As mentioned in Chapter 3, there are several problems existing in the current system which will have to be corrected before implementation of the carrier recovery subsystem is completed. These problems will also be discussed in this chapter.

The multipath fading performance of the system will be evaluated using a two-ray multipath simulator which operates in the 4GHz frequency band, according to the transfer function given in Equation (4.103), and which can simulate a flat fade or a frequency selective fade at the RF filter input to the receiver.

In Section 5.2, we begin with the measured values of BER versus the receiver RF input signal level (RSL). These measurements will demonstrate one of the most significant problems existing in the equipment, as presently implemented. In Section 5.3 the transmitter performance is examined and the effect of varying phase and amplitude balance in the transmitter on the system BER is examined in order to demonstrate the advantage of the independent adjustment of tap-weights affecting the I-axis and tap-weights affecting the Q-axis. In Section 5.4 the performance evaluation of the receiver in the presence of two-ray multipath is begun. In this section the measured sampling phase is compared with the theoretical value obtained in Chapter 4, and the measured BER is examined for the two-ray relative amplitude b varying between zero and two for mid-band notches. The ability of the DFE to track between MP and NMP regions of a two-ray multipath model will also be discussed in this section. It is related to the eigenvalues of the adjustment matrix calculated in Chapter 4. Finally, in Section 5.5 the measured outage signature for notch depths between -8MHz and +8MHz from mid-band are given and compared with predicted outage signatures obtained from the results of Chapter 4.

5.2 BER versus Receiver Input Signal Level

In Figure 5.1 the measured BER as a function of the receiver input signal level is compared with the theoretical values for 49QPRS assuming ideal matched filtering. The discrepancy between the measured and the theoretical BER is so large that one might think it neccessary to correct this problem before examining any other aspects of the system performance. However, this problem was initially overlooked due to preoccupation with the debugging and testing of the DFE. The magnitude of this problem was not fully appreciated until well into the process of collecting data and writing this thesis. Under these conditions, however, it is significant that the DFE is capable of equalizing a two-ray multipath fade due to a 40dB notch depth when the unfaded RSL is -34 dBm, since a flat fade causing the same reduction in RSL ($\simeq$16dB) reduces the BER to 8×10^{-6}.

After all the measurements presented in this chapter were taken, it was determined that the cause of the large discrepancy in noise performance versus RSL and the non-linearity were being caused by a failed LNA and mixer assembly in the front end of the receiver. With the failure, there was enough signal "leaking" through at 4 GHz so that the AGC amplifier could make up the loss in signal level. The same failed amplifier stage was likely causing both the degraded thermal noise performance and the non-linearity. By substituting the LNA and mixer assembly with another mixer

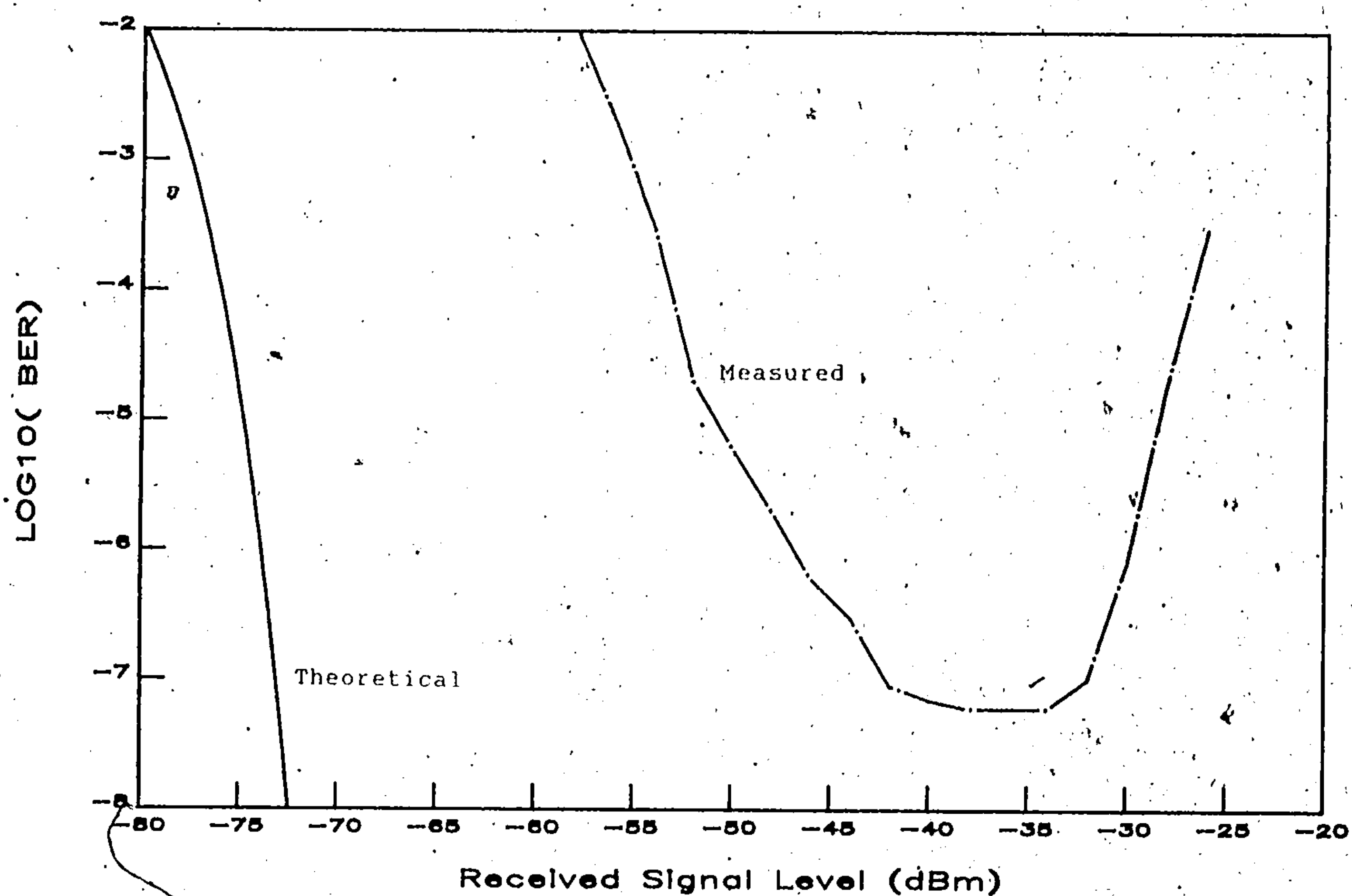

Figure 5.1 Measured BER versus Received Signal Level and Theoretical BER Assuming Gaussian Noise

and an IF LNA which was specified to have a Noise Figure of 13 dB and observing that the "loss-of-lock" threshold improved by 12 dB it was determined that the failed LNA had approximately a Noise Figure of 25 dB within an estimated error of 2 or 3 dB. The poor precision here is due to the fact that before the problem in the receiver front end was identified, the only available BER measuring instrument had a power supply failure and, as was previously stated, the improvement noted with the substituted front end was estimated by the loss-of-lock threshold improvement. By observation of the eye diagram quality with the substituted receiver front end it was also determined that the non-linearity problem at high RSL was due to the failed front end. With a significant delay being anticipated to repair the measuring instrument and since the results demonstrate significant improvements available from the use of the joint sampling phase and tap-weight adaptive DFE even with the failed front end, the results taken with the failed front end are presented. Also, I plan to continue this work in the future so that the full potential of this system will eventually be known.

5.3 Transmitter Performance

In this section, the BER performance versus transmitter output power, BER performance versus transmitter modulator gain and phase unbalance, and the transmitter output spectrum are examined.

In order to determine the effect of the transmitter linearization without being masked by the poor receiver performance with respect to RSL variation, an attenuator was used to maintain the RSL at -34dBm as the transmitter power output was varied. The result of this measurement is not plotted because there isn't much to see. The BER stays constant at $6x10^{-8}$ with respect to power output for all values up to and including 31.5dBm. At 32.5dBm output level the BER is increased by two times to a value of $1x10^{-7}$. A power level of 32.5dBm at the PA output corresponds to its 0.5dB compression point. The 0.5dB compression point is defined as the point in output power or input power level where the output power is 0.5dB less than that predicted by the small signal gain of the power amplifier. The transmitter baseband equipment was not designed to drive the PA output power to any higher output level because of the possibility, when using feedback for linearization, of overdriving the PA input. To elaborate on this, the peak to average value of the power in an ideal rectangular pulse 16QAM is 2.5dB and becomes larger by the use of feedback as can be seen by comparing Figures 2.5 and 2.6. At 32.5dBm average output power, the peak power due to the largest symbol is at least 35dBm. Another 1.5dB of output power would require, by extrapolation, an input level for the largest signal state greater than the maximum input level of 5dBm as can be seen in Figure 5.2. It is not known whether the maximum rated input signal level of the amplifier is for average or peak power, however, a peak power maximum is a safe assumption to make.

It is difficult to compare the performance of the feedback linearized transmitter (FLT) with the results of other linearizers published recently, for several reasons. In most published results, the PA output power is referenced to the saturated output power but an exact saturated power output for the FET amplifier in use could not be determined due to a maximum input power limitation. A value of 36.5dBm is used as the saturated output power and the 1db and 0.5dB compression points for this amplifier are 34.3dBm and 32.7dBm. Also, it is difficult to say what the full potential of the FLT is when it is working with an error-floor of 6×10^{-8}. The majority of the second generation digital radios, which all use 64QAM, also use non-adaptive predistortion, however, only a couple of publications [74,16] give enough details to make comparisons. In one case[74] of fixed predistortion, applied to a TWT, a 10dB output backoff was required to maximize the system gain at a BER of 10^{-6} and by a small extrapolation, approximately 7dB

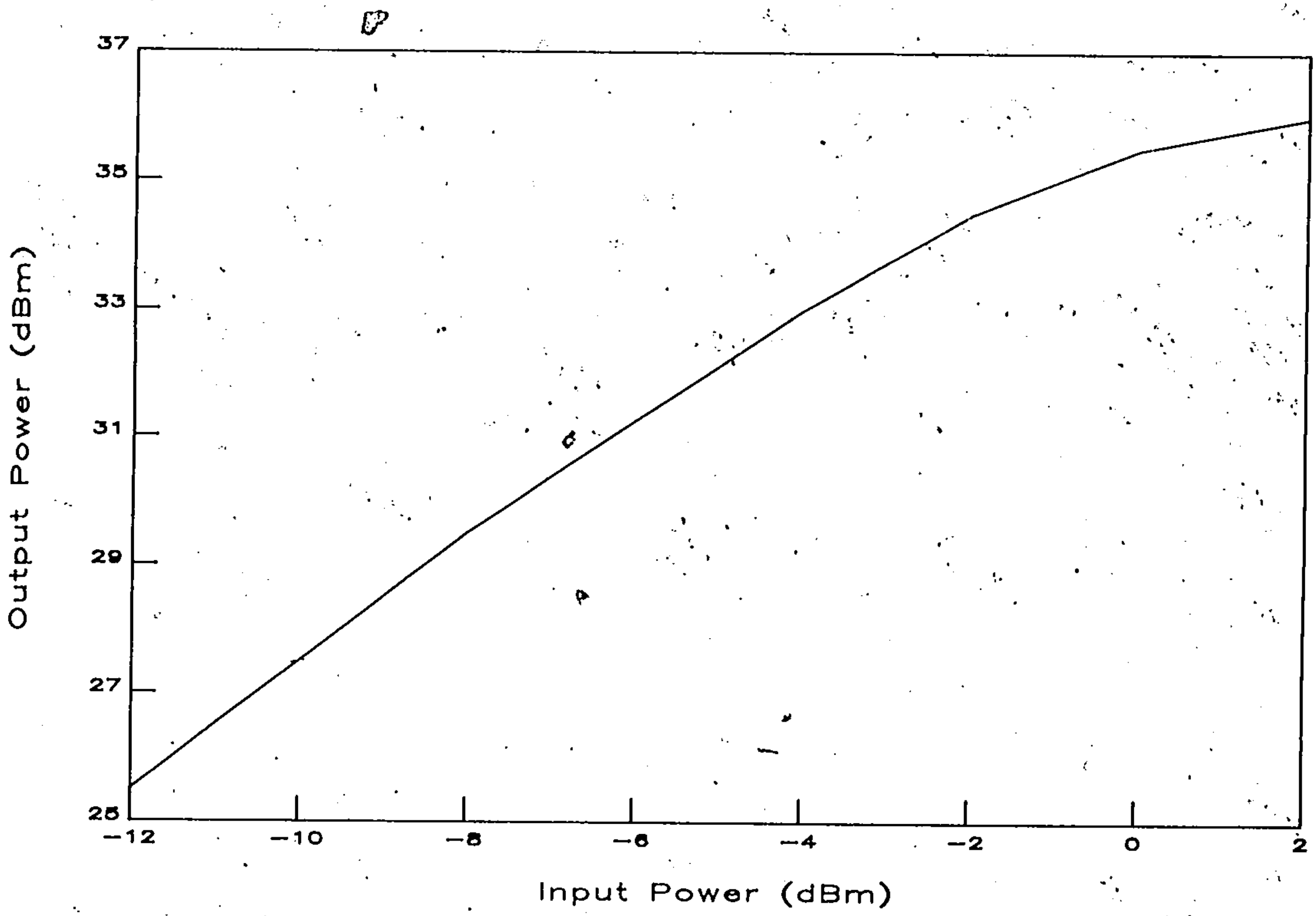

Figure 5.2 Transmitter Power Amplifier Output Power versus Input Power

back-off was required to obtain an open eye. System gain is the difference between the transmitter output power and the receiver threshold for a BER of 10^{-6} in this case. In another case[16] both a TWT and FET amplifier were used with fixed predistortion. They required 11.5dB and 7dB respectively of output back-off to maximize the system gain and approximately 9.5dB and 5dB of output to obtain an open eye. The FLT is providing a BER of 10^{-7} at approximately a 4dB output back-off in the 49QPRS system when the minimum BER achievable at any RSL is $6x10^{-8}$. In the analysis done in Chapter 2, it was seen that to get a 4% peak eye closure in the 16QAM signal set at the PA output the power output must be raised to the 1dB output back-off point. This is approximately the peak eye closure required to increase the BER from $6x10^{-8}$ to $1x10^{-7}$ in the presence of Gaussian noise. The FLT had the same increase in BER at an output back-off of 4 dB.

The system BER performance versus the gain and phase balance of the transmitter modulator is really a confirmation of the DFE's ability to correct completely for the ISI introduced by these distortions, as was explained in Chapter 2. Of course, there is a noise penalty associated with these distortions and in Figure 5.3 and Figure 5.4 where the measured variation in BER versus amplitude and phase unbalance are plotted, the theoretical values with respect to Gaussian noise are also given for comparison. The

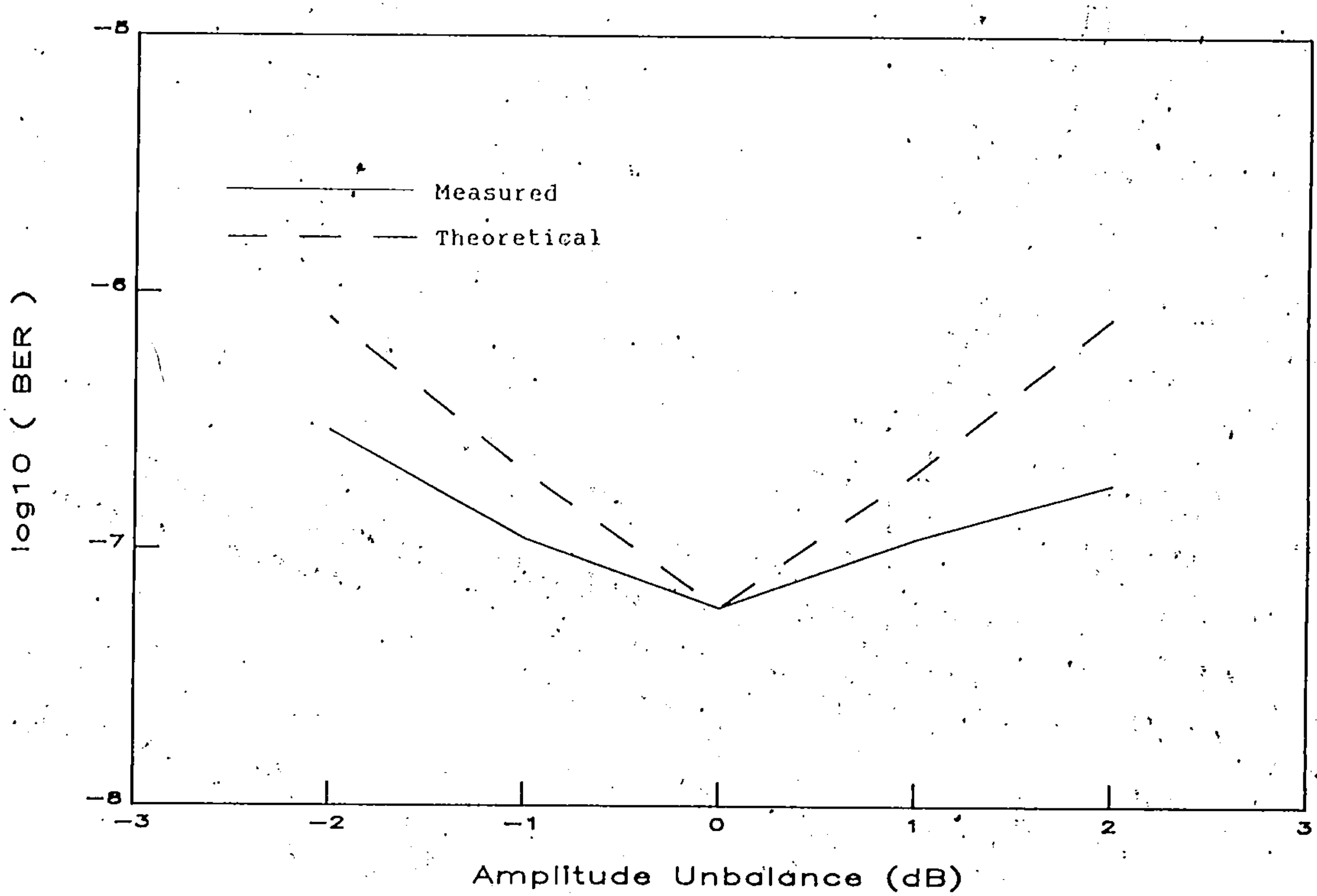

Figure 5.3 Measured BER versus Amplitude Unbalance and Theoretical BER Assuming Independent Adjustment of I-axis and Q-axis Tap-Weights

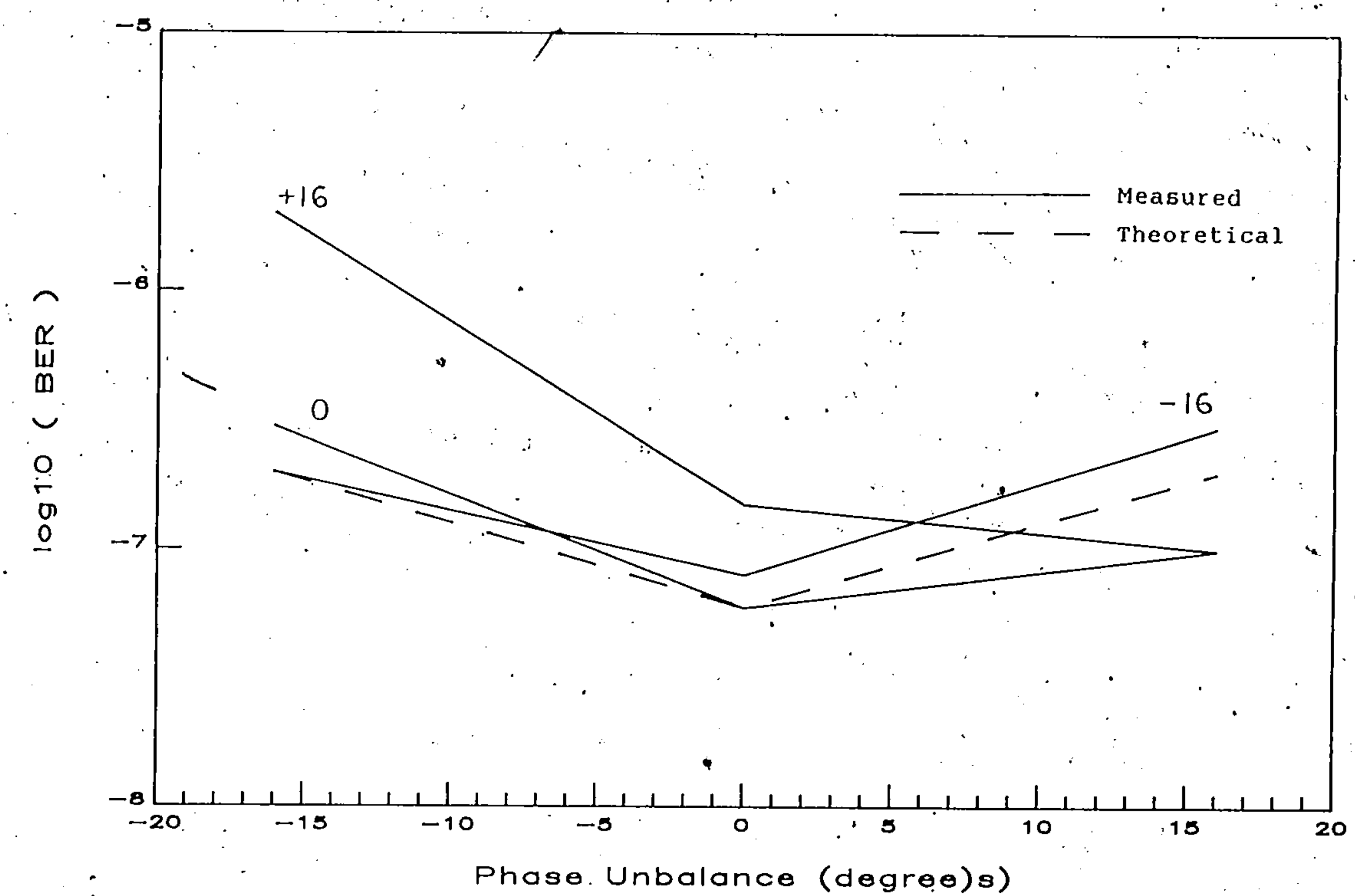

Figure 5.4 Measured BER versus ±16° Phase Unbalances of FLT Demodulator for various FLT Modulator Phase Unbalances, and Theoretical BER versus a Simple Modulator or Demodulator Phase Unbalance

receiver was operated at an RSL of -34dBm for these measurements which is in the region of minimum BER. A source of error between the measured and theoretical values is the assumption of Gaussian distributed noise since the noise controlling the performance may be a combination of non-linearity and noise from the failed front end. The validity of this comparison is related to the closeness of this noise to being Gaussian. The theoretical increase in BER due to amplitude unbalance was determined by increasing the SNR in one dimension and decreasing it in the other dimension by an amount related directly to the amplitude unbalance. This, of course, assumes independent adjustment of the tap-weights affecting I-axis and Q-axis error. In the case of phase unbalance, there are three phase shifters in the FLT which affect the phase quadrature. It is not a simple matter to calculate the theoretical degradation due to phase unbalance for all the permutations of phase errors within the FLT, so the theoretical BER due to Gaussian noise in Figure 5.4 was calculated for the quadrature phase error associated with a simple QAM modulator, and assuming independent I-axis and Q-axis tap-weight adjustment of the DFE. For this case, the theoretical increase in BER due to phase unbalance was determined by decreasing the SNR by the square of the cosine of the phase unbalance. The measured BER's for permutations of 0° and ±16° phase errors of the modulator and demodulator are also plotted in Figure 5.4. The theoretical BER's for equal I-axis and Q-axis tap-weights are much larger. A phase unbalance of 8.9° is enough to cause a minimum decision distance of zero[57]. For both the gain and phase unbalance cases the theoretical and measured values are close. The theoretical BER due to phase unbalance of a QAM modulator is very close to that measured for the demodulator of the FLT when the modulator phase unbalance is set to zero. The slope component of the measured results is likely due to some error in what was thought to be the zero phase unbalance setting.

In Figure 5.5 photographs of the transmitted spectrum are shown. In Figure 5.5a the LOG REF line is equal to the total signal power and the measurement bandwidth is 10KHz, so that by making a 4dB adjustment to obtain the power in a 4KHz slot it can be seen that the transmitted spectrum just meets the FCC mask for 20MHz channel at the ±10MHz points. For measurements further out of band, Figure 5.5a is limited by spectrum analyser noise and Figure 5.5b which is measured in a 300kHz slot demonstrates that the FCC mask is met with increasing margin as the distance out of band increases.

5.4 Performance for Mid-Band Fading

In this section the performance of the receiver will be examined with respect to frequency notch depths due to

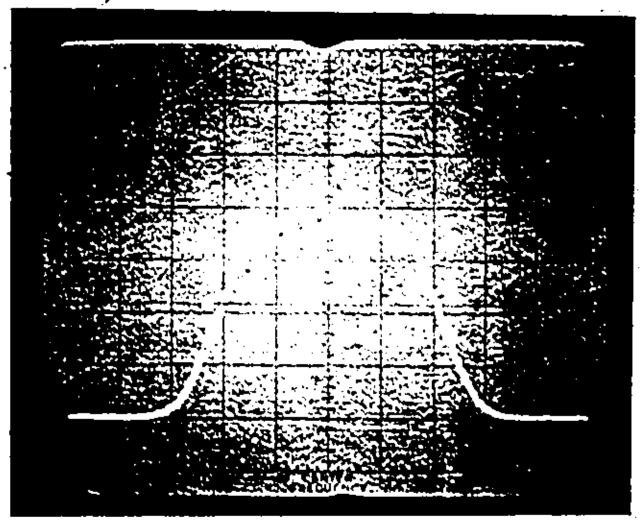

a) Transmitter Spectrum
(LOG REF is total
carrier power)
10 kHz Bandwidth
5 MHz/div
10 dB/div

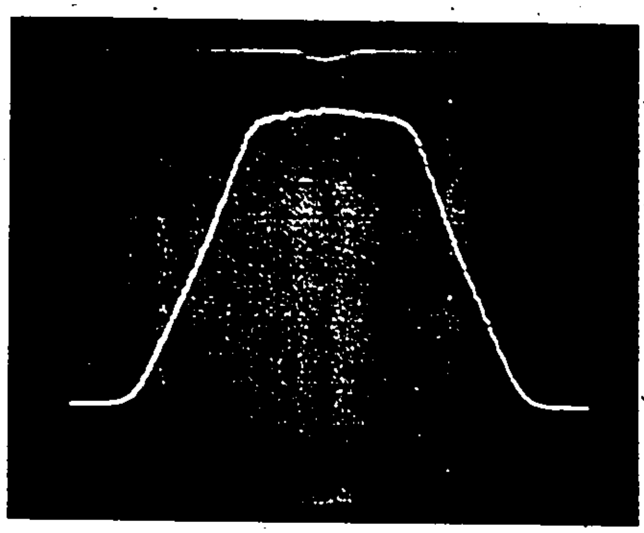

b) Transmitter Spectrum
100 kHz Bandwidth
5 MHz/div
10 dB/div

Figure 5.5 Transmitter Spectrum Photographs two-ray multipath at mid-band, where the loss of signal power is the greatest. The fading model used is given in Equation (4.103). It should be noted again that the fade notch depth parameter B (in dB) and the relative two-ray amplitude b are equal to Rummler's model parameters for the case of MP fading and for NMP fading, B and b are related to Rummler's parameters B_o and b_o by Equations (4.103a) through to (4.103k) and Equation (1.3). For mid-band fading the DFE works according to the objectives stated in Chapter 1. The performance for frequency notches away from band centre, where the ISI component of the MSE is larger, is not as good as the potential indicated in Chapter 4 and this will be discussed in the next section.

In Figure 5.6, photographs of the 7-level eye diagram at the input to the DFE, the equalized eye diagram at the DFE quantizer input, and the IF spectrum at the input to the IF AGC amplifier are shown with no multipath present at an RSL of -34dBm. This RSL is used for measured results throughout this section unless otherwise stated. In Figures 5.7a through Figure 5.7f the photographs of the equalized eye diagrams are shown for values of b ranging from zero to two for f_o equal to zero. In Figure 5.8 the corresponding IF spectrums at the IF filter output (IF AGC amplifier input) are shown. In Figure 5.9 the measured sampling phase and theoretical sampling phase from the calculations of Chapter 4 are compared versus the relative two-ray amplitude b, and

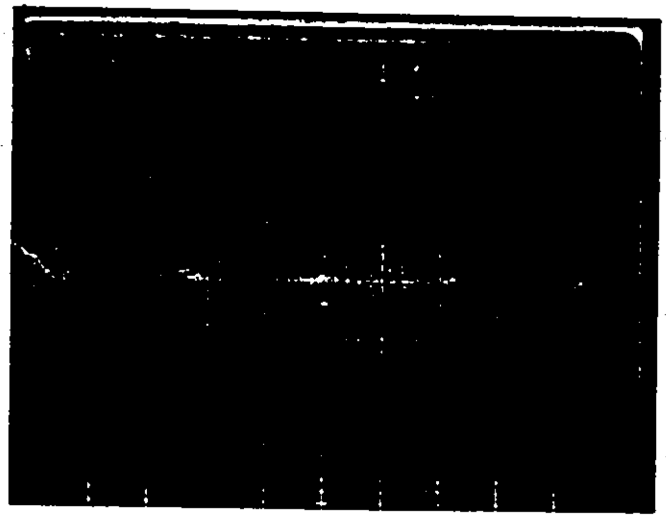

a) Seven Level Eye at DFE Input

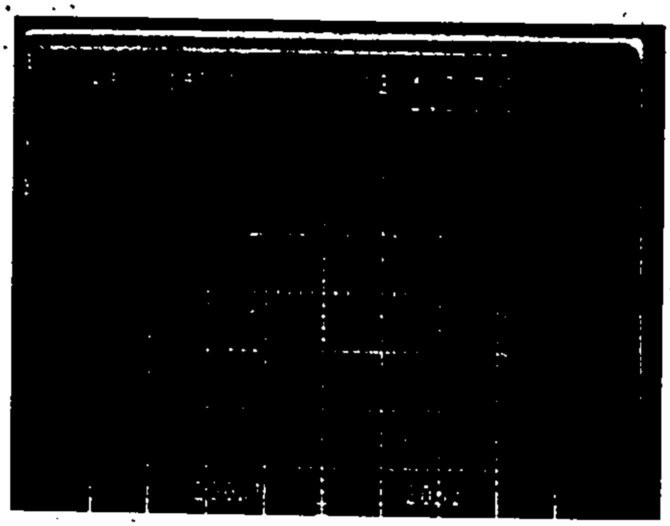

b) Four Level Eye at DFE Quantizer Input

Figure 5.6 Photographs of Eye Diagrams at DFE Input and at DFE Quantizer Input Without Multipath in Figure 5.10 the measured BER and the calculated MSE from Chapter 4 are compared. In Figure 4.10, it can be seen that an infinite notch depth causes a 16dB loss in the RSL, and from Figure 5.1 it can be seen that even a constant versus frequency drop of 16dB in the RSL to -40dBm is enough to reduce the BER to a value of 10^{-5}. The measured BER at an infinite notch, using an RSL of -34dBm is only 10 times the flat faded BER, which means that only a small degradation is suffered due to multipath induced ISI. For this reason, the BER was also measured versus b at an RSL of -24dBm and this is given in Figure 5.11. In order to determine the effect of tap-weight adjustment noise and sampling phase adjustment noise, the measured RMS value of the on-axis tap-weight and the measured RMS value of the sampling phase control signal are given as a function of b in Figure 5.12.

Many observations may be made on these measured results and the comparison to the theory of Chapter 4. A very positive result is the agreement between the measured and theoretical sampling phase as the relative amplitude b is varied between zero and two for f_o equal to zero. It is confirmed also from observation that the most difficult equalization region of the multipath is not at the MP to NMP transition (b=1) where an infinite notch exists but in the approximate NMP region between notch depths of 20dB (b=1.11) and 25dB (b=1.06) where at least for this particular implementation the two distinct loci of the MMSE

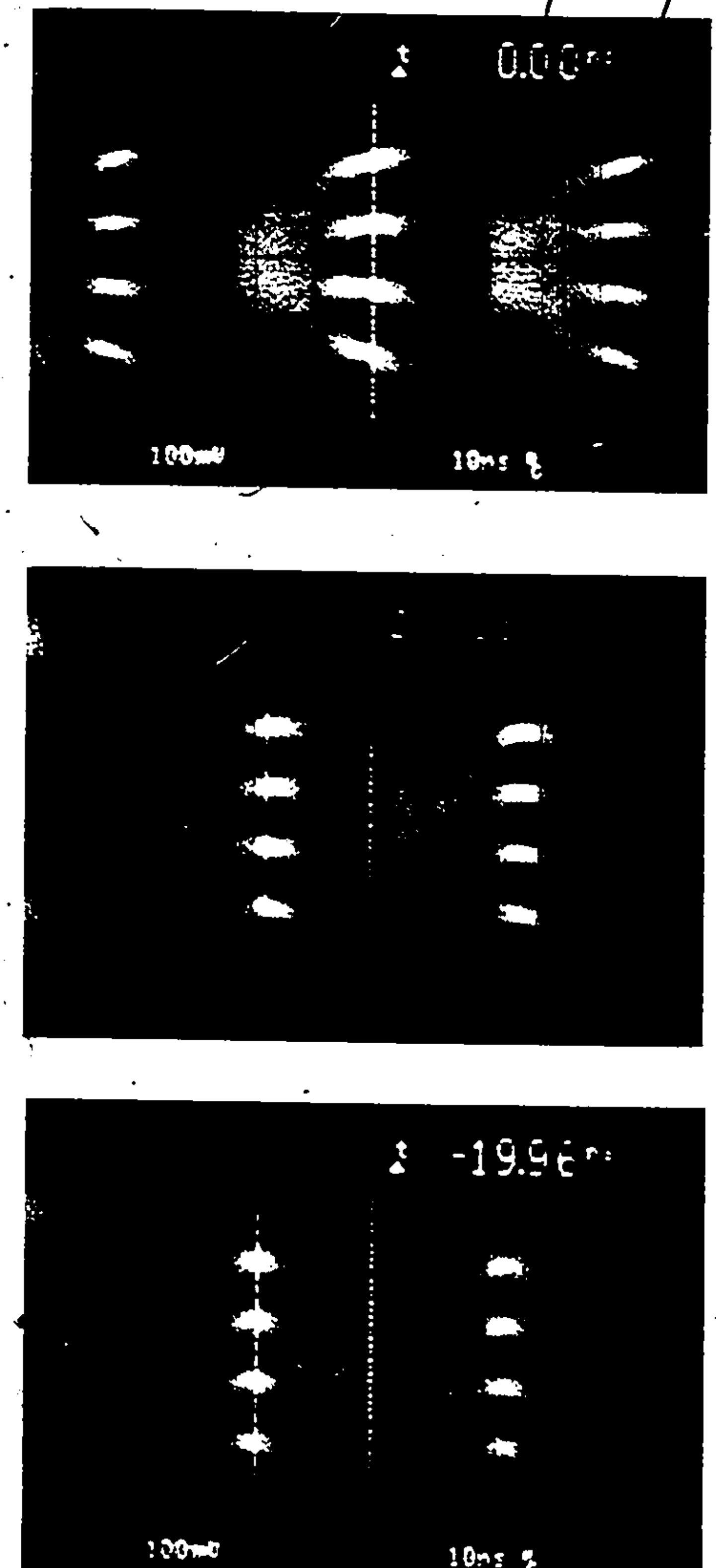

a) $b = 0$

$f_o = 0$ MHz

$B = 0$ dB

BER $= 6 \times 10^{-8}$

$t_o = 0$ ns

b) $b = .94 \pm .02$

$f_o = 0$ MHz

$B = 24$ dB

BER $= 4 \times 10^{-6}$

$t_o = -18.2$ ns

c) $b = 1 \pm .01$

$f_o = 0$ MHz

$B = 38$ dB

BER $= 2 \times 10^{-4}$

$t_o = -20$ ns

Figure 5.7 Photographs of Eye Diagrams at DFE Quantizer Input for various Relative Amplitudes of Two-Ray Multipath

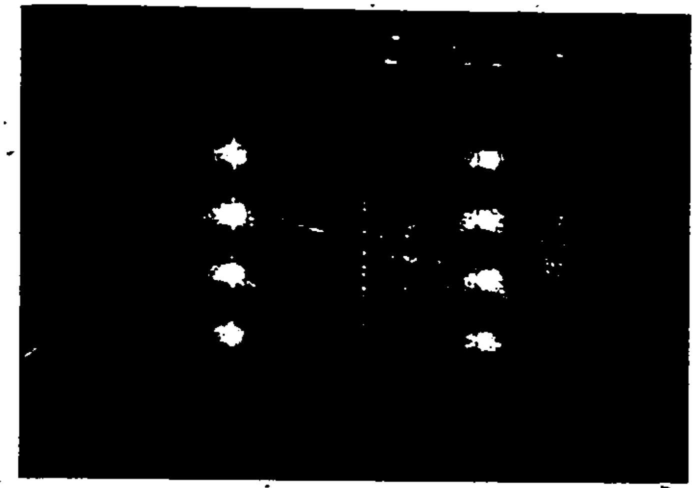

d) $b = 1.05$

$f_o = 0$ MHz

$B = 25$ dB

BER = 8×10^{-3}

$t_o = -22$ ns

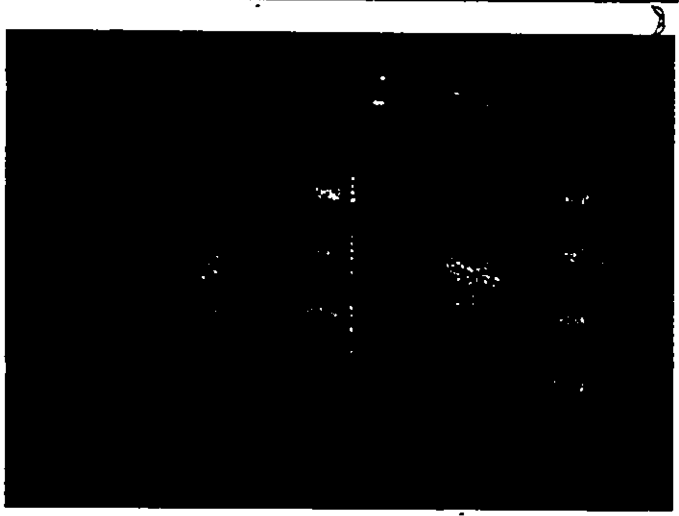

e) $b = 1.07$

$f_o = 0$ MHz

$B = 23$ dB

BER = 2×10^{-2}

$t_o = +40$ ns

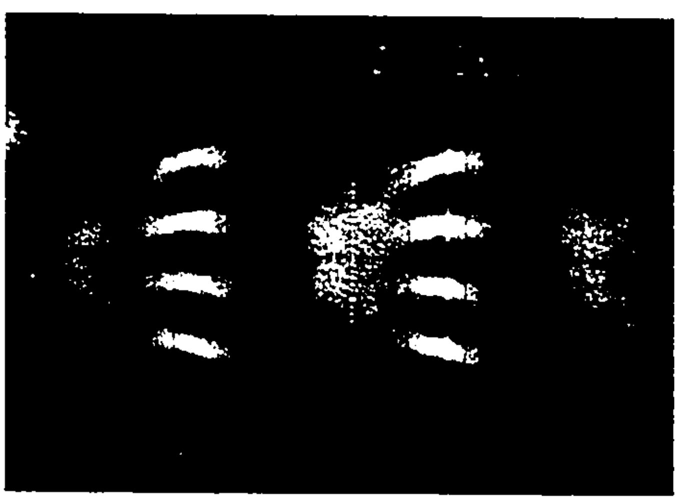

f) $b = 2$.

$f_o = 0$ MHz

$B = 0$ dB

BER = 1×10^{-7}

$t_o = +16.8$ ns

Figure 5.7 Photographs of Eye Diagrams at DFE Quantizer Input for various Relative Amplitudes of Two-Ray Multipath

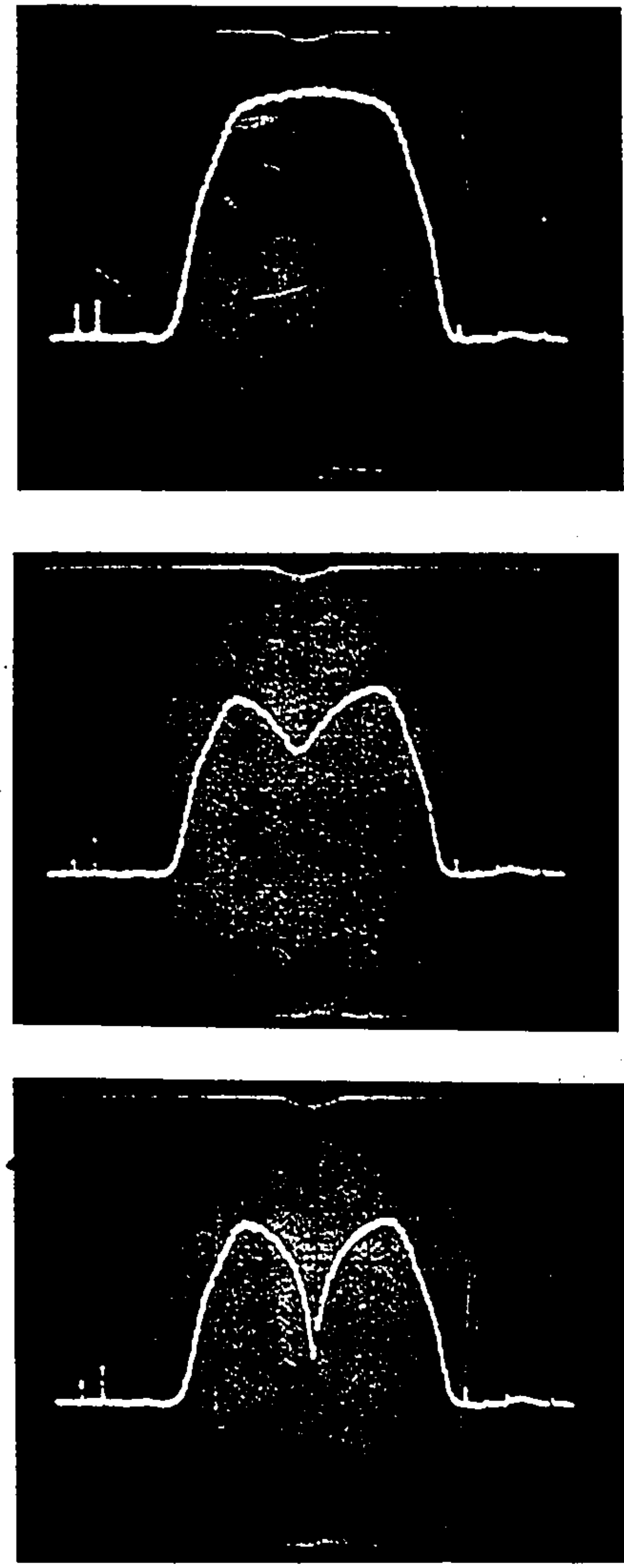

a) $b = 0$

$f_o = 0$ MHz

$B = 0$ dB

BER $\cong 6 \times 10^{-8}$

$t_o = 0$ ns

5 MHz/div   10 dB/div

b) $b = .94 \pm .02$

$f_o = 0$ MHz

$B = 24$ dB

BER $= 4 \times 10^{-6}$

$t_o = -18.2$ ns

5 MHz/div   10 dB/div

c) $b = 1 \pm .01$

$f_o = 0$ MHz

$B = 38$ dB

BER $= 2 \times 10^{-4}$

$t_o = -20$ ns

5 MHz/div   10 dB/div

Figure 5.8   Photographs of Receiver IF Spectrum at IF Filter Output for various Relative Amplitudes of Two-Ray Multipath

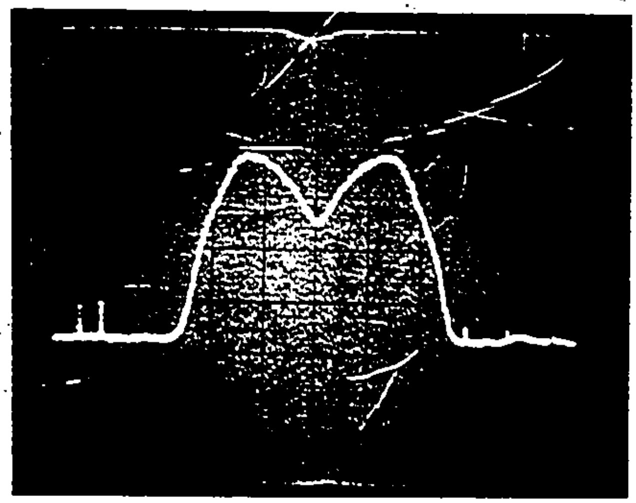

d) $b = 1.05$

$f_o = 0$ MHz

$B = 25$ dB

BER $= 8 \times 10^{-3}$

$t_o = -22$ ns

5 MHz/div 10 dB/div

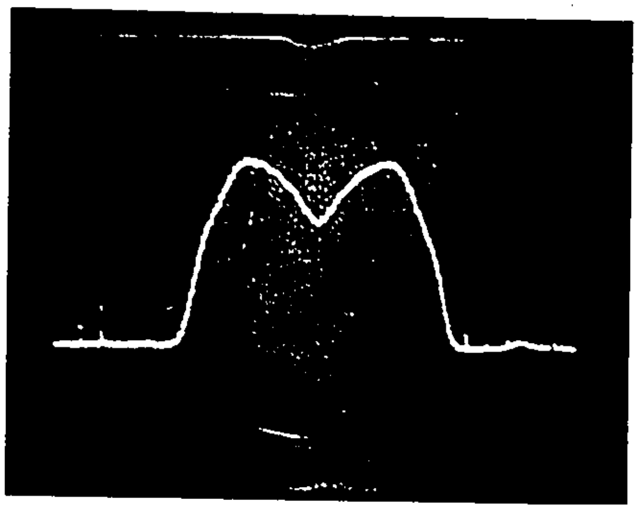

e) $b = 1.07$

$f_o = 0$ MHz

$B = 23$ dB

BER $= 2 \times 10^{-2}$

$t_o = +40$ ns

5 MHz/div 10 dB/div

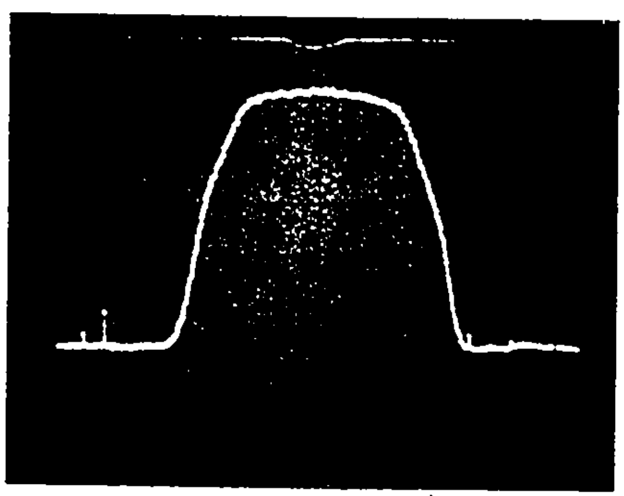

f) $b = 2$

$f_o = 0$ MHz

$B = 0$ dB

BER $= 1 \times 10^{-7}$

$t_o = +16.8$ ns

5 MHz/div 10 dB/div

Figure 5.8 Photographs of Receiver IF Spectrum at IF Filter Output for various Relative Amplitudes of Two-Ray Multipath sampling phases end. As described in Chapter 4, the MP locus was obtained when the system was started up (or the adaptive parameters were initially acquired) in the MP region of the multipath and the NMP locus was obtained when the system was started up in the NMP region of multipath. There are some differences between the theoretical and implemented behaviour with respect to these two loci. In theory, the MP locus exists through both the MP and NMP multipath region although as b increases into the NMP region the ratio of the maximum and minimum eigenvalues gets orders of magnitude larger and the determinant of the channel autocorrelation matrix gets very small, whereas the NMP locus effectively ends for b between 1.1 and 1 due to excessively high MSE. In the implemented system the MP locus ends around b equal to 1.08 but interestingly as b is increased above 1.08 the NMP locus is easily acquired at this point even though the MSE is high. The system can thus track from the MP locus to the NMP locus. For the case of a decreasing values of b on a NMP locus the NMP locus ends, according to theory, due to high MSE but only rarely does the system acquire the MP locus, and this only occurs when the value of b is decreased rapidly. To summarize, the DFE can equalize any mid-band multipath fading, and the sampling phase tracking or acquisition between the MP locus, which ends at b equal to 1.08, and the NMP locus is relatively easy, while the tracking or acquisition between the NMP

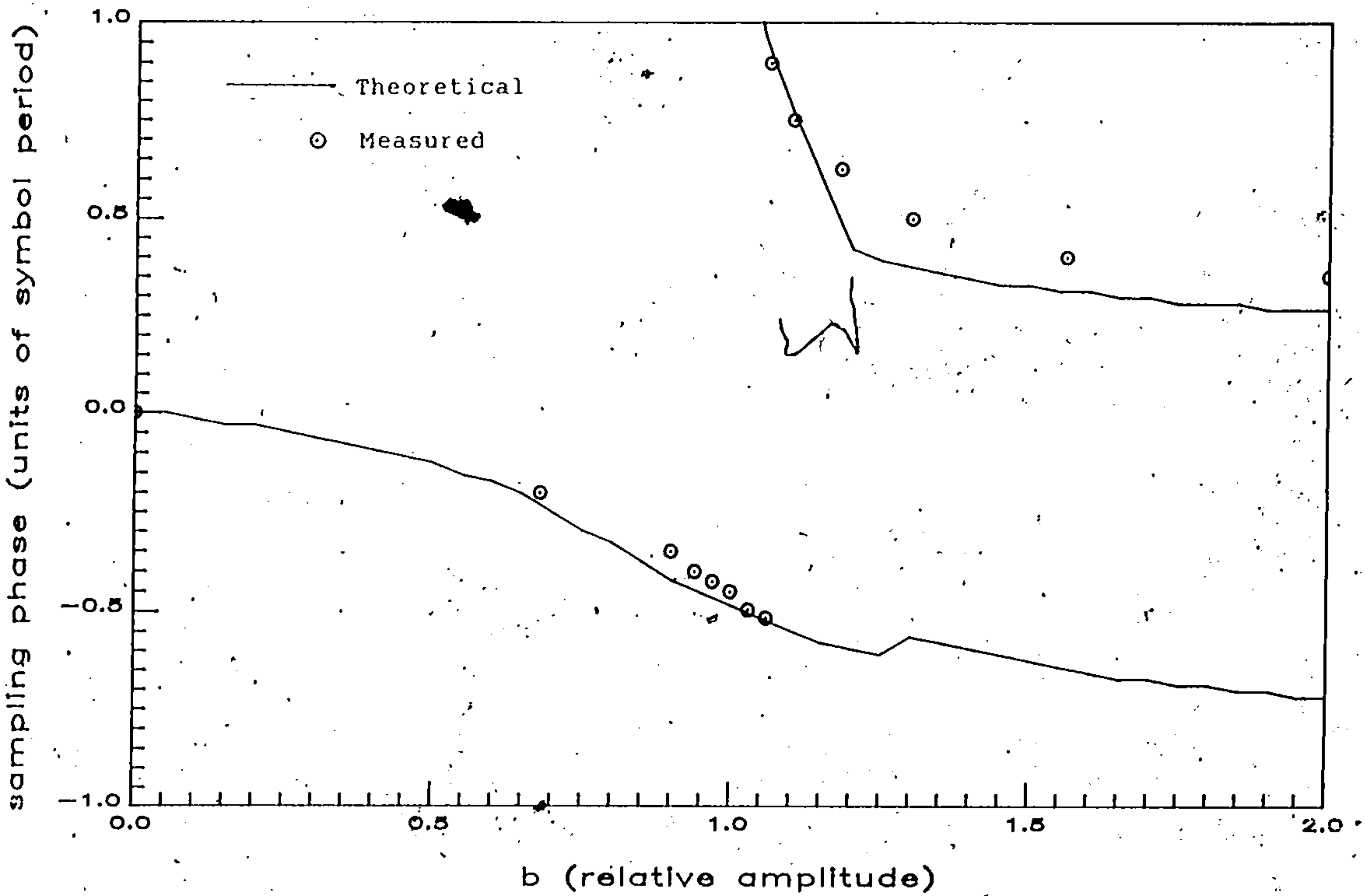

Figure 5.9 Measured and Theoretical Sampling Phase versus Two-Ray Multipath Relative Amplitude

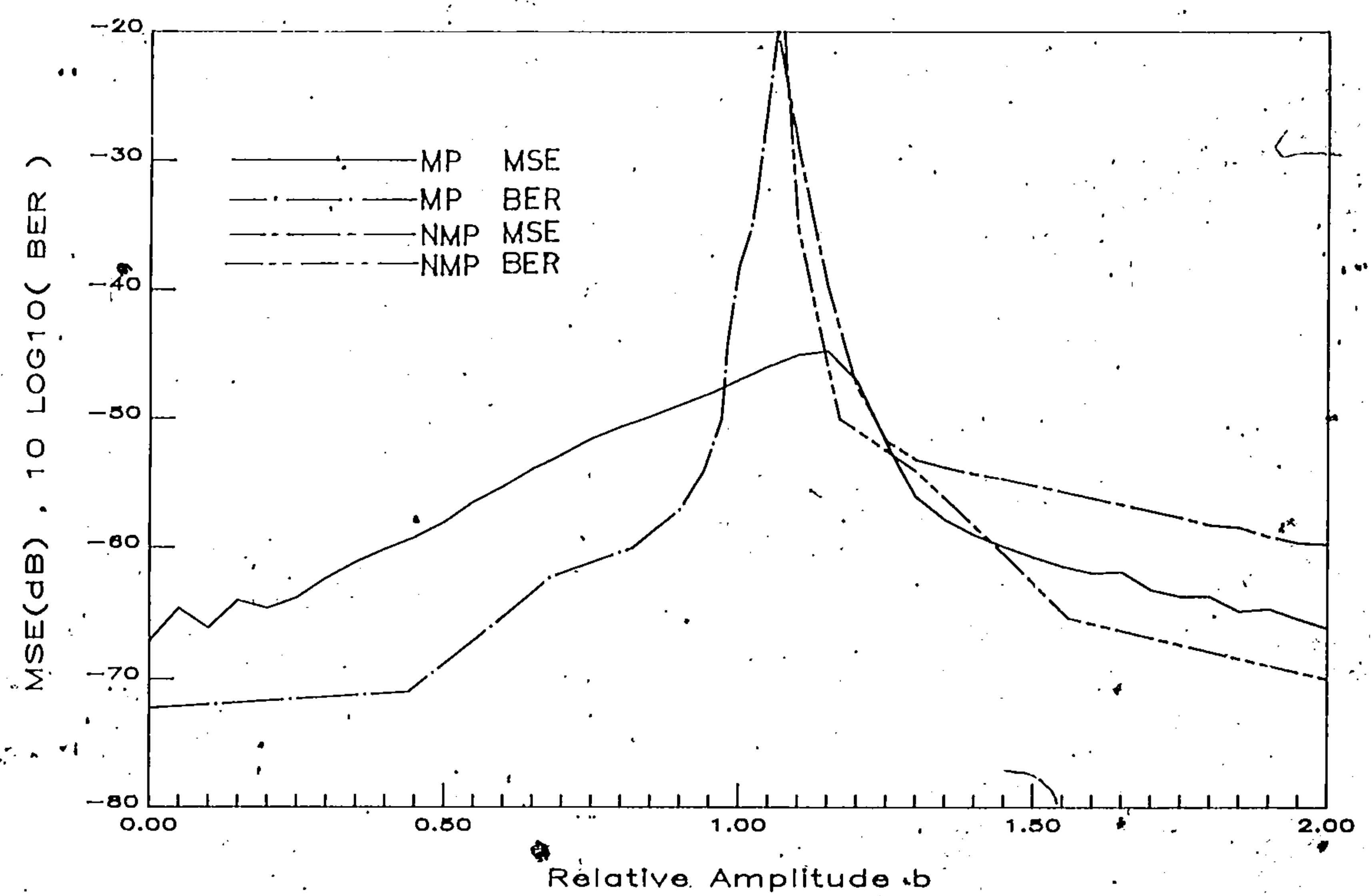

Figure 5.10 Measured BER and Theoretical MMSE versus Two-Ray Multipath Relative Amplitude and at an RSL of -34dBm

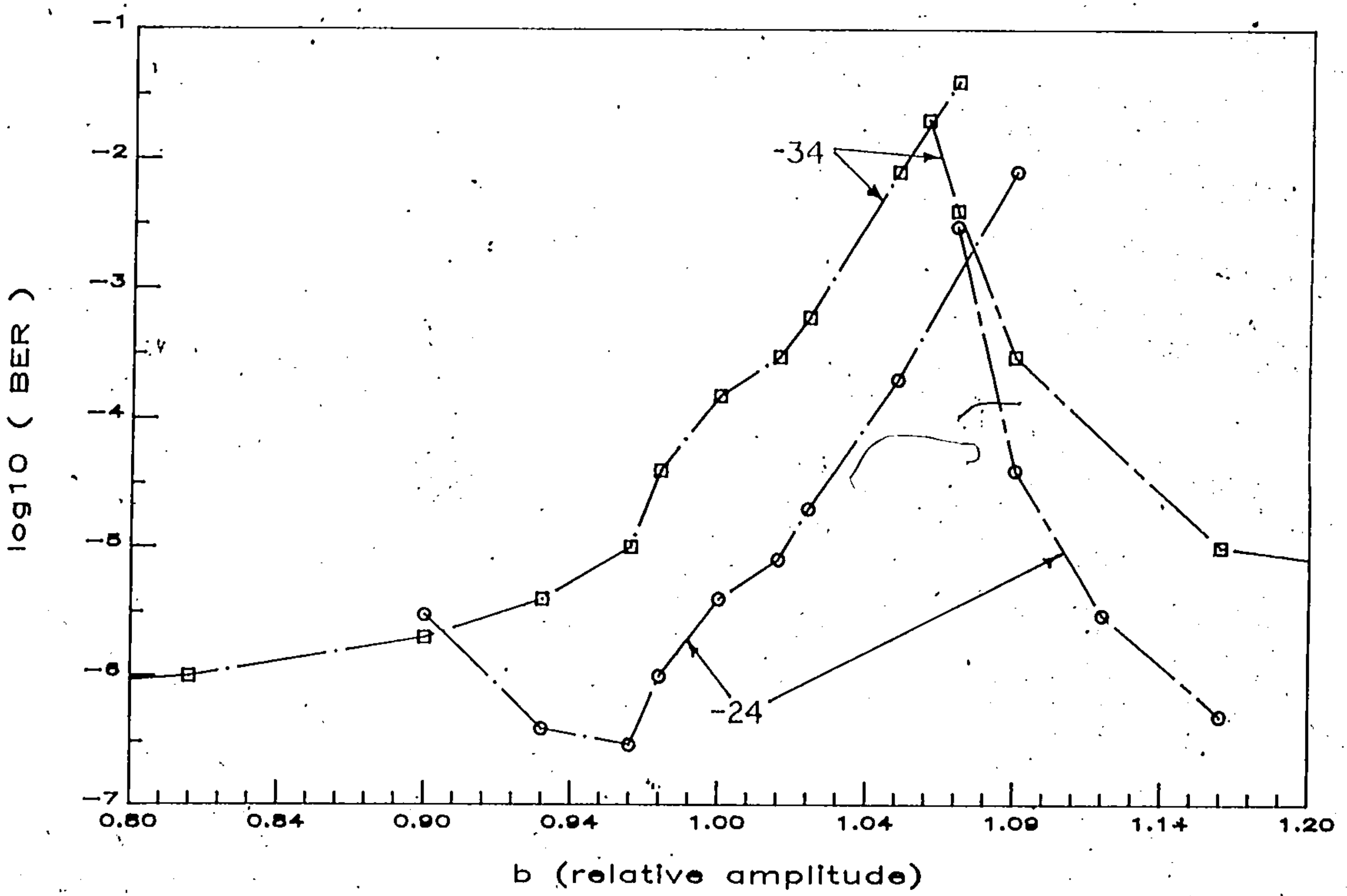

Figure 5.11 Measured BER versus Two-Ray Multipath Relative Amplitude for Received Signal Levels of -34dBm and -24dBm

locus and the MP locus is very difficult and usually causes the implemented system to lose acquisiton until action is taken to reacquire. This leads us into a discussion of the acquisition performance.

Since decision-directed adaptation is being used for 40 tap-weights and two DC offsets in the system and since the sampler phase and frequency are also acquired jointly with the tap-weights, the first question that one might ask about the system operation, would be about acquisition perfotmance. However, before the acquisition performance is described a hardware implementation problem which affects the acquisition performance is described. When a parameter register is at its maximum (or minimum), a positive (or negative) count to the register should cause the register to stay at its maximum (or minimum) value and not to wrap around to the minimum (or maximum) value. Unfortunately, it was overlooked in the design stage that the registers should limit rather than wrap around. The register values represent using offset binary, tap-weights over the range of approximately ±2 in steps of 4/256. The zero multipath on-axis value of the reference tap is ±1, assuming a phase reference of 0°. It has been observed that once one parameter (usually a tap-weight) wraps around, the entire system loses acquisition and all the parameters begin to oscillate by periodically wrapping around and the only way the system can then reacquire is by initializing all the parameter values to zero. This wrap around problem is another problem that must be corrected before the joint carrier recovery subsystem as proposed in Chapter 3 is implemented, since acquisition would be more difficult when carrier acquisition is also required.

The acquisition performance is now described. The system will acquire for any mid-band fade notches between 0dB and 30dB depth in the MP region and up to a 20dB depth in the NMP region. It is interesting to note that the system can acquire in the NMP region of mid-band multipath when the BER is as high as 1×10^{-2}. This acquisition behaviour offers an explanation for the observed system behaviour as b is varied about a value of approximately 1.08. Essentially, the ability of the system to track between the MP and NMP loci is related to the acquisition performance at a value of b equal to 1.08 which corresponds to a notch depth B equal to 22dB.

The reasons for the system not tracking the MP locus for relative amplitudes b above 1.1 is now examined. The theoretical MSE for the MP locus at a b value of 1.08 is just 3×10^{-5}, whereas for the NMP locus the MSE is 3×10^{-3} so that MMSE can probably be ruled out as the cause of the loss of tracking for the MP locus. By examining the measured RMS values of the reference on-axis tap-weight and the sampling phase control signal in Figure 5.12 it can be seen that tap-weight and sampling phase control signal noise is

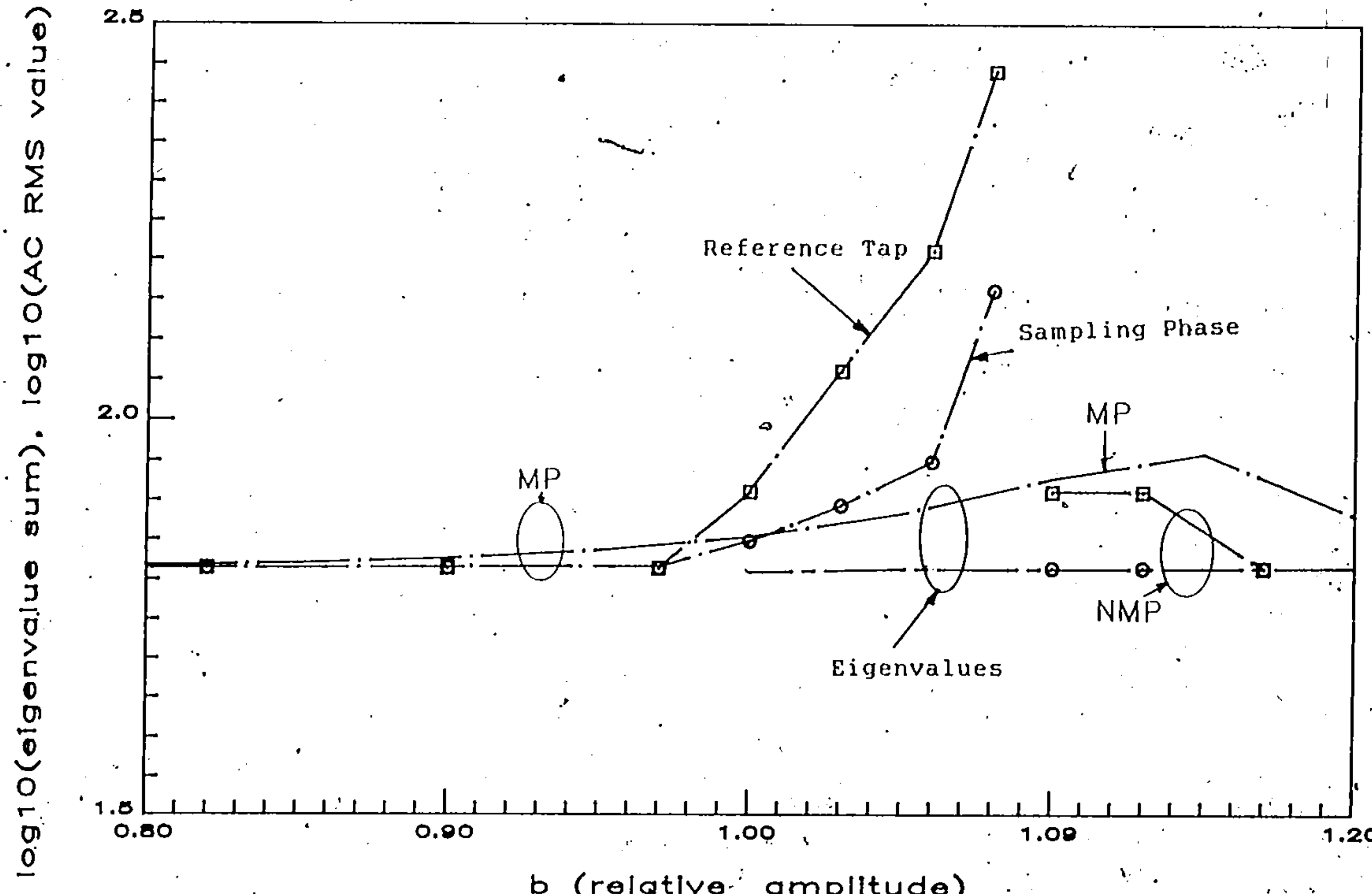

Figure 5.12 Logarithm of Reference Tap and Sampling Phase Control RMS Voltage and Logarithm of the Sum of Adjustment Matrix Eigenvalues

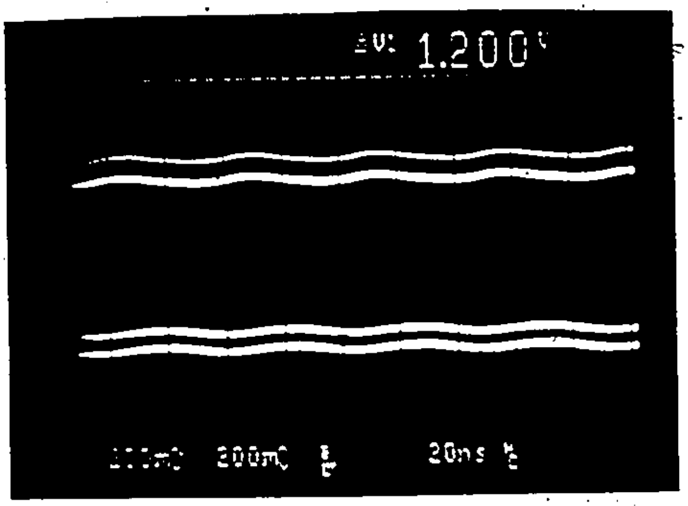

a) $b = 0$

$f_o = 0$ MHz

$B = 0$ dB

$BER = 6 \times 10^{-8}$

$t_o = 0$ ns

on-axis(bottom)

cross-axis(top)

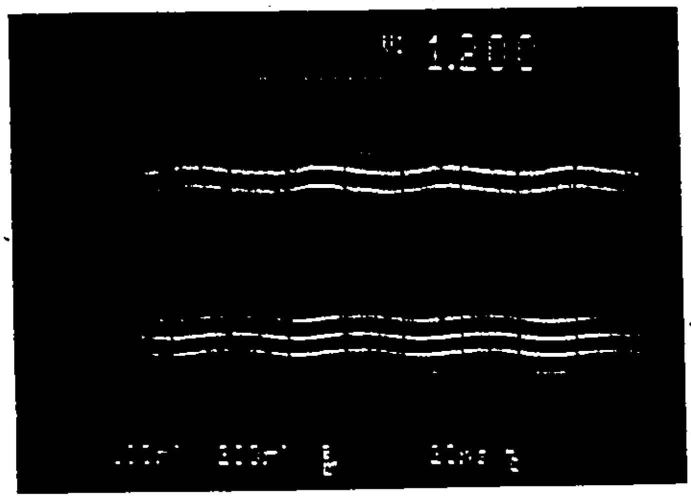

b) $b = 1.05$

$f_o = 0$ MHz

$B = 25$ dB

$BER = 8 \times 10^{-3}$

$t_o = -22$ ns

on-axis(bottom)

cross-axis(top)

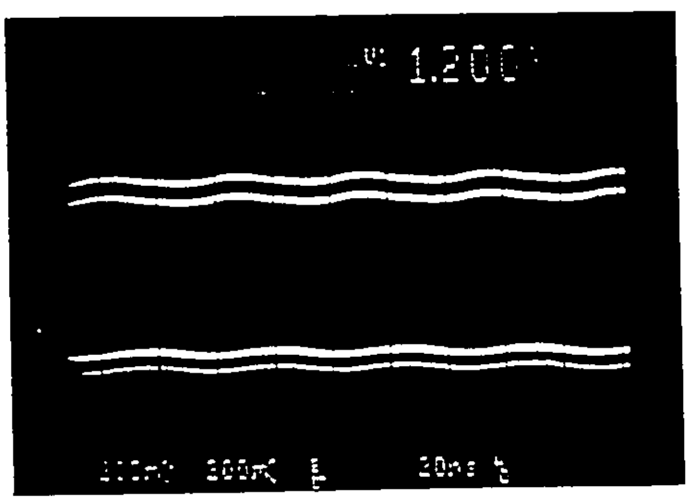

c) $b = 1.07$

$f_o = 0$ MHz

$B = 23$ dB

$BER = 2 \times 10^{-2}$

$t_o = +40$ ns

on-axis(bottom)

cross-axis(top)

Figure 5.13 Photographs of On-axis and Cross-axis Reference Tap-Weight Voltages over One Second Time Period for various Two-Ray Multipath Relative Amplitudes roughly constant over all values of b for both loci, except for the MP locus with b between 1 and 1.1 so that it appears that equalizer misadjustment noise is beginning to control the DFE in this region. This increase in the parameter variance appears to be related to the sum of the eigenvalues of the adjustment matrix, which is also shown in Figure 5.12. Also,the eigenvalue spread, or the ratio of maximum to minimum eigenvalue increases very rapidly as b is increased above 1.05 for the MP loci, and this reduces the system's tracking ability. Another observation is also relevant to the loss of tracking ability for the MP locus at b equal to 1.08. As previously stated, the magnitude of the tap-weights is limited to a range of two in the implemented system and as b is increased beyond one, the magnitude of the complex valued reference tap-weight begins to increase towards a value of two. The implemented DFE then loses its tracking ability the first instant that the sum of the reference tap-weight mean value and the peak error due to tap-weight misadjustment noise exceeds ±2, because of the wrap around problem, which was previously described. Obviously, removing the wrap around problem will improve this situation. Also, by increasing the dynamic range of the tap-weights to greater than two, or by increasing the size C of the up-down counter used to control the tap-weight register (to reduce the tap-weight variance), the tracking range for the MP loci could be extended further into the NMP region.

A flat fade of 16dB at an RSL of -34dBm causes a BER of 10^{-5}. An infinite notch selective-fade, which also causes a 16dB drop in RSL, causes a BER of 10^{-4}. From these two observations it is seen that the BER for an infinite notch selective fade at an RSL OF -34dBm is mostly controlled by the threshold, interference and linearity problems of the receiver. The measured BER versus the multipath relative amplitude b at an RSL of -24dBm shown in Figure 5.11 demonstrates even more conclusively that the unfaded receiver BER performance is controlling the performance with respect to mid-band multipath for all values of b except in the region between 1.03 and 1.10, where for the NMP locus it is controlled by the theoretical MMSE and for the MP locus it appears to be affected by tap-weight noise. This tap-weight noise appears to be related to the eigenvalue sum and possibly, the rapid increase in eigenvalue spread as b is increased above 1.05. The only obvious way to improve the tap-weight noise in this implementation is to increase the size C of the up-down counter register. However, this would also result in a decrease in tracking speed of the system. Without examining dynamic fading, it can not be said whether there is any excess tracking speed which could be traded off for reduced tap-weight noise in this fading region.

To demonstrate the action of the up-down counters and the tap-weight noise just referred to, three photographs of the on-axis and cross-axis tap-weight values are shown in Figure 5.13 for three different multipath situations. The exposure time on these photographs is 1s. From Section 3.5, the number of tap-weight adjustments in a 1s time period has a minimum mean value of $1/(C^2T)$, which is over 1000. The discrete quantization levels of the tap-weights can be seen in the photographs and hence, the brightness of each quantization level gives an indication of the proportion of the 1s time interval spent at that quantization level. It can be seen that for no multipath (b equal to zero) only two or three quantization levels are likely and the probability of correct adjustment P_c is sufficiently close to one. This is also the case for the NMP locus for b at 1.07, even though the theoretical MMSE is only .01 and the BER is approximately 10^{-2}. For the case of the MP locus at b equal to -1.05 it can be seen that the probability of correct adjustment P_c of the tap-weights has decreased and the tap-weight noise has increased.

5.5 Measured and Theoretical Outage Region

In this section a measured b-f_o plane of the outage region is examined for notch frequency offsets ranging between ±8MHz. It is estimated that with the failed LNA the SNR at an RSL of -34 dBm is approximately 41 dB. This estimate assumes that the measured system is 1 dB from theory at the loss-of-lock threshold for which outages are measured in this section. The reason for using the loss-of-lock threshold is explained shortly. If a unfaded SNR of 63 dB is assumed then b-f_o plane presented would be at a flat fade depth of 22 dB. The measured outage region is compared with several different theoretical outage regions based on loss-of-lock outage criterion obtained for different system impulse responses in Chapter 4. This comparison will show that the measured system performance for frequency notches away from band centre is not up to potential, and the comparison to outage regions for different system impulse responses will serve to give possible reasons for the sub-potential operation.

In Chapter 4 it was explained that the desired local minimum of the MSE for the sampling phase could disappear under certain conditions, dependent on the actual channel impulse response. This was observed to occur for values of the relative amplitude b between .85 and 1.15 and notch frequency offsets between 5MHz and 15MHz. The reason for examining loss-of-lock criterion is the fact that this disappearance of the local minima was occuring at normalized MSE's that were less than -30 dB and there was no outage (outage defined by an MSE of -20 dB which if Gaussian would cause a BER of 10^{-3}) due to ISI or thermal noise in the theoretical calculations for any values of b or f_o until the unfaded SNR was reduced to 35.4 dB. i. e. The system would lose lock before the BER above 10^{-3}. The measured system

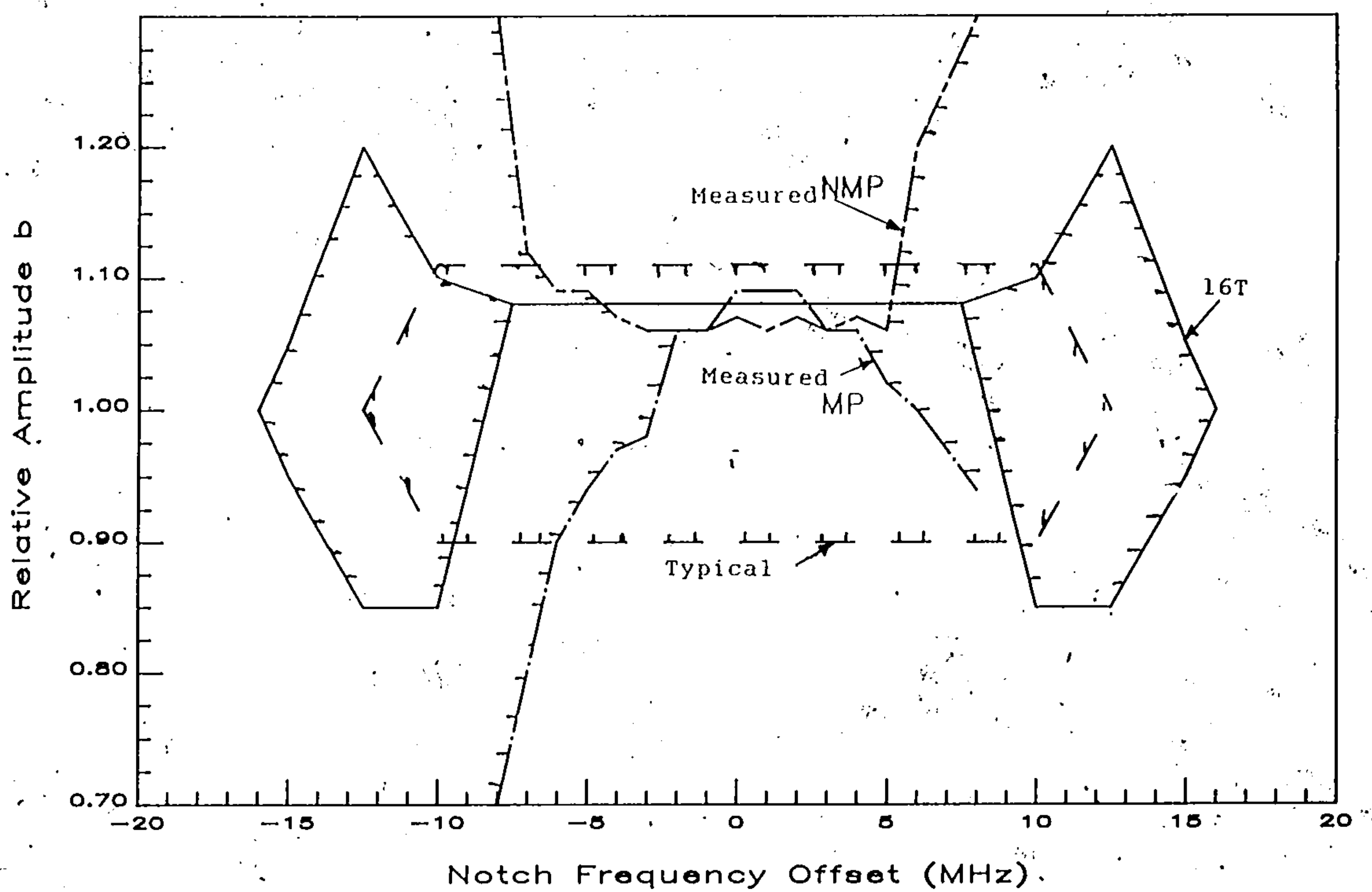

Figure 5.14 Measured Outage Region at SNR=41dB and Theoretical Outage Region for τ_g equal to 16T at SNR>36dB, and Outage Region Typical of "Second Generation" Digital Radios at High SNR

also exhibited behaviour like this for off-band centre fading but near mid-band, there was a significant difference between loss-of-lock and BER greater than 10^{-3}. When this loss of the local minima occurred the first minimum to be found using a gradient approach was about two symbols in the negative direction. Typically, this minimum had a low MMSE, an eigenvalue spread of 10^{7}, and reference tap-weight values much larger than those achievable in the implemented system. It was found that by weighting the sinc pulses of the impulse response with a Gaussian function to reduce the magnitude of the impulse response tails, the region where there was no usable minimum for the sampling phase could be shrunk to nothing for the Gaussian pulse half amplitude width τ_g equal to 8T. For τ_g equal to 16T this region extends from 5MHz to 15MHz in notch frequency offset and from .85 to 1.15 in relative amplitude.

In Figure 5.14 a theoretical outage region for τ_g equal to 16T and the measured outage region of the implemented system are shown using the loss-of-lock as described previously. The measured outage region is only displayed up to a notch frequency offset of 8MHz because the multipath simulator used had not yet been placed under computer control for calibrated operation. The measured results for offsets up to 8MHz are sufficient to determine that the system is not working as close to theory as desired and needs further work to remove the receiver threshold and linearity problem, and the wrap-around problem.

The main reason for comparing these two outage regions is that the implemented system may be suffering a similar problem to the theoretical one. The equipment amplitude and phase versus frequency responses are very different from that assumed for the theoretical case but the net result seems to be the same. If the tails of the implemented system impulse response are too large then it is possible as in the theoretical case that the clock recovery loop will lose lock due to the disappearance of the local minimum of the MSE. This could easily be the case since a steep roll-off IF filter is used in the receiver and no amplitude or group delay equalizers were used before the DFE except a five tap IF transversal equalizer with the reference tap being the middle one.

There are other possible reasons for the measured outage region to be larger than predicted by theory. By referring to Figure 4.5, it is seen that the theoretical MMSE (which does not include parameter quantization and misadjustment noise) is larger for off band centre fades by up to 15dB, yet, the experience from the NMP locus at mid-band suggests that the MSE is not too high as long as there is not an excessive amount of misadjustment noise. However, since the difference between the MSE for the off band centre fades and the NMP locus at f_o equal to zero is only 5dB it would not take a lot of misadjustment noise to cause problems. Another way of viewing the difference between theory and measured results is seen by observing that the measured system BER for no multipath implies a noise source much larger than assumed in the theory. If the noise in question was assumed to be Gaussian then a SNR of between 25dB and 30dB would have to be assumed to explain the measured BER with no multipath and if this level of input noise was assumed in the theoretical system then it would be very unlikely that the resultant MMSE would be sufficiently small for successful operation, since it was found from the measured results for the NMP locus at a two-ray relative amplitude b equal to 1.1 that a theoretical MMSE of approximately -27dB relative to the signal power was required to maintain acquisition of the tap-weights and other parameters.

When all these arguments are considered, it can only be said that to find agreement between theory and practice, it is neccessary to use a theoretical model which agrees more closely with the constructed system, or alternately, to construct a system which agrees more closely with the theoretical model. To summarize, some of the important degrading effects not included in the theoretical model are:

i) non-linearity, degraded threshold, and interference,

ii) actual equipment filter responses,

iii) misadjustment noise,

iv) tap-weight wrap-around.

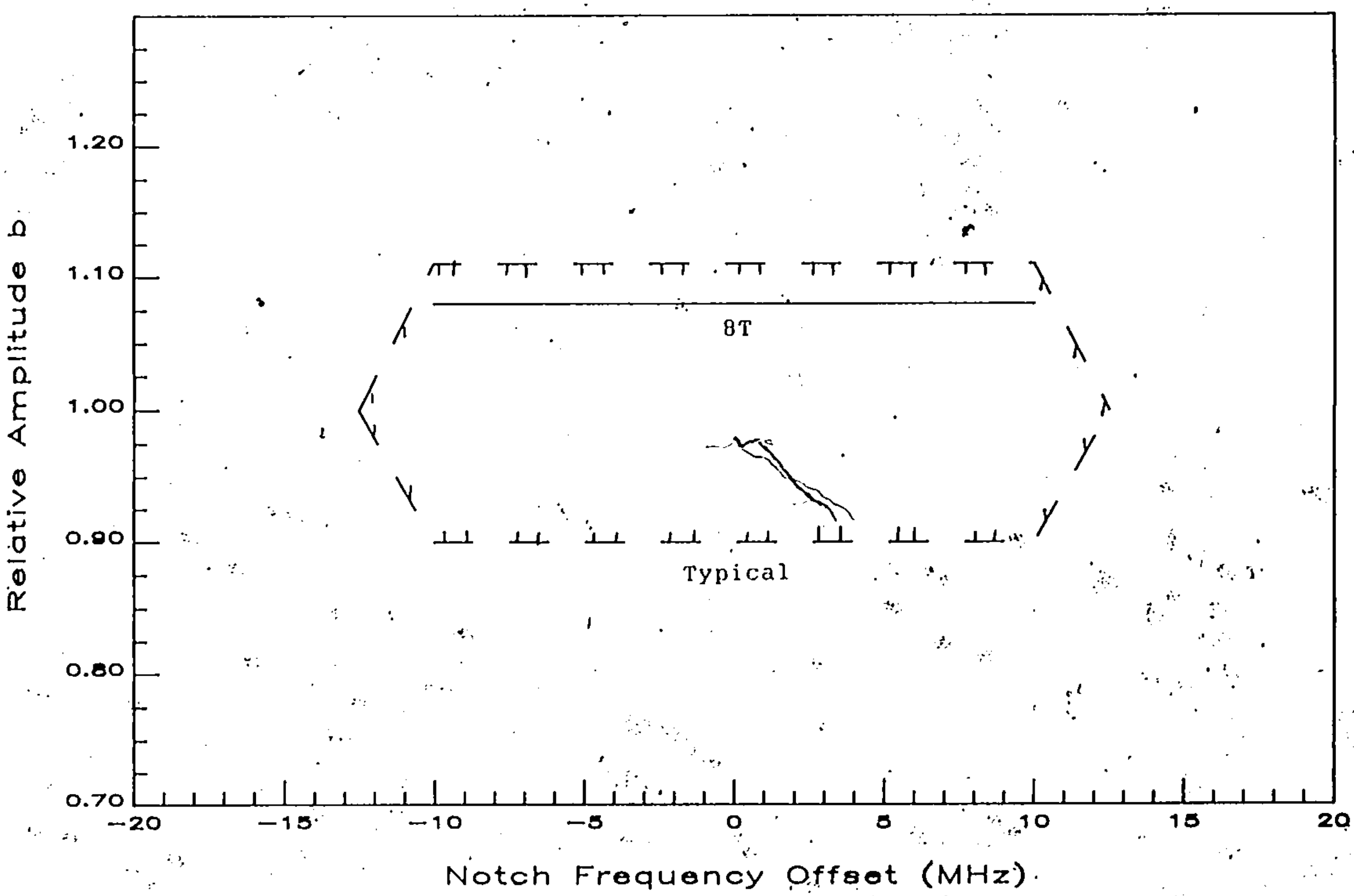

Figure 5.15 Theoretically Predicted Outage Region for τ_g equal to 8T at SNR>36dB and Outage Region Typical of "Second Generation" Digital Radios at High SNR

When these degrading effects are made insignificant or are removed in an implementation, then the theoretical results suggest that the outage region for high SNR may reduce approximately to a straight line in the b-f_o plane that reaches between notch frequency offsets of +12 MHz to -12 MHz at a relative amplitude of b equal to 1.1 as shown in Figure 5.15. The line would not imply any outage for a static multipath situation but would imply an outage time for dynamic multipath determined by the reacquisition time. If acquisition was impossible in some regions then there would be two outage regions determined by the direction of crossing and the region where acquisition was impossible. It should be added here that this complete elimination of static outage for any b and f_o exists for SNR's down to 36 dB. For less than this the outage region opens up very quickly. Assuming the theoretical performance, a flat fade margin of 51 dB would be required to obtain a conditional probability of outage of 2% due to flat fading, conditioned on the occurence of fading, and values of relative amplitude of 1.05 and notch offset of 0 MHz which is the worst case for b and f_o.

CHAPTER 6

CONCLUSION

6.1 Introduction

In this chapter the significant results of the work are summarized, additional conclusions are drawn, and problems for further study are suggested. Several of the significant findings were obtained as a result of the construction of a prototype high capacity digital microwave radio. The radio was designed to operate at 4050MHz in a 20MHz channel allocation according to the FCC mask[51]. The data rate used was 90Mbits/s so that the efficiency of bandwidth utilization was 4.5bits/cycle. The modulation method used was 49 state QPRS. Since the ideal 49QPRS spectrum does not fit within a 20MHz bandwidth, the transmitted signal was overfiltered in the transmitter to meet the FCC mask and the resultant ISI was removed in the receiver by the use of a manually adjustable IF transversal equalizer.

6.2 Description of Significant Contributions

The significant contributions in the application of digital microwave radio are three in number. Two are obtained from the system implementation just described and one which is theoretical in nature has application in other areas besides digital radio. These contributions are summarized as follows:

i) The constructed feedback linearized transmitter is the first application of feedback for linearizaton of a QAM modulator and a transmitter power amplifier. Since the input and output signals are the baseband data signal and modulated bandpass signal, a coherent demodulator is used in the feedback path.

ii) The DFE constructed is the first application of a joint sampling phase and tap-weight adaptive DFE in high rate digital microwave radio. In addition, the sampling phase and tap-weight adaptation is done digitally which is also a first in digital microwave radio. The adaptive DFE is the first implemented adaptive system in digital microwave radio to successfully equalize a 40dB notch depth at mid-band and to track through a transition from the minimum phase region to the non-minimum phase region of a two-ray multipath.

iii) A matrix analysis was done to determine the eigenvalues for the joint MMSE adaptation of sampling phase and tap-weights of a DFE. The MMSE is independent of carrier phase since the DFE can resolve any carrier phase. This analysis establishes both the steady state and tracking behaviour of the jointly adaptive receiver.

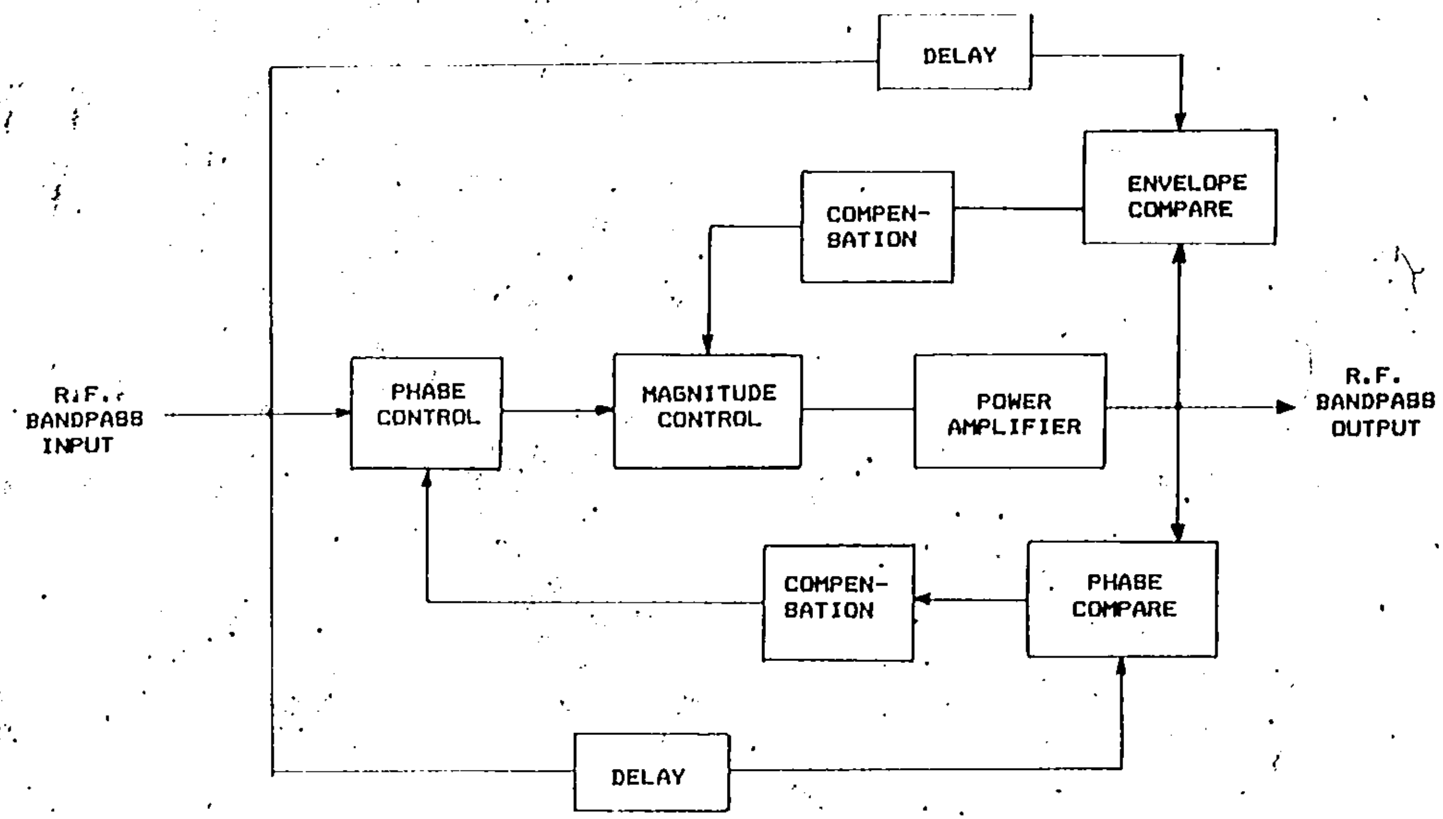

Figure 6.1 A Magnitude and Phase Based Method of Feedback Linearizing a Bandpass Signal, suggested for Future Investigation

6.3 Conclusions and Future Work

i) Although the constructed system used a zero-forcing or peak error based tap-weight adjustment and an MSE based sampling phase adjustment, the eigenvalues calculated for MMSE adjustment were useful in explaining the observed behaviour of the system. For future work, it would be useful to determine the eigenvalues for a decision-directed algorithm as described by Equation (4.91). Also, it would be useful to determine the the effect of parameter quantization on the MSE .

ii) Feedback works well in linearizing the transmitter power amplifier. For the feedback to be practical the symbol period should be much greater than the loop transit time and should be implemented in an integrated form to minimize the loop delay time and the cost of constructing the system. One of the problems involved with using direct modulation, as required by this method is that the convenience of connecting a transmitter modulator and receiver directly at IF is lost. This is particularly troublesome during debugging and test functions when it would be convenient to isolate different parts of the system. It is suggested for future work, to consider another method of feedback linearization where the instantaneous envelope error and phase error are corrected by feedback, rather than the I-axis and Q-axis values, as shown in Figure 6.1. Using this method, the linearization could be done without a modulator or demodulator; and the feedback system would accept a RF bandpass input and, of course, provide an RF bandpass output. This system is potentially simpler than the FLT described in this thesis, and it may be possible to implement it with a smaller loop time delay.

iii) Theoretically there is more than one minimum in the MMSE with respect to the sampling phase, but due to extremely small minimum eigenvalues which makes these minima difficult to acquire in practice or possibly due to restricted range of the tap-weight values, local minima other than the two closest to a sampling time of zero were not observed in the implemented system. With respect to a variation in the two ray multipath relative amplitude, there are two distinct loci of sampling phases which minimize the MSE. These were observed to agree very closely in both theory and practice for mid-band fades. The two loci were referred to as the MP sampling phase loci and the NMP sampling phase loci, according to which region of multipath the parameters were initially acquired. The NMP sampling phase locus cannot be tracked in the implemented system for relative amplitudes b less than 1.05 due to large MMSE. The implemented system can track the MP locus for values of relative amplitude up to 1.1 and is limited at that point by increasing misadjustment noise which is related to the sum of the system eigenvalues, although tap-weight dynamic range, tap-weight quantization noise, and the calculated eigenvalue spread may also be involved. For mid-band fading, performance is good in the region of relative amplitude around 1.00. However, the ability to track through the region of relative amplitude b between 1.05 and 1.10 is related to the acquisition performance since as the ability to track one locus ends, it is neccessary to acquire the other one. As the multipath relative amplitude b is increased through this range, the NMP sampling phase locus can be acquired from the MP sampling phase locus. However, as b is decreased through this region, acquisition of the MP sampling phase locus from the NMP locus is more difficult and could only be observed occasionally.

iv) The acquisition performance of the implemented system for mid-band fading is good, considering that the tap-weight adjustment is decision-directed and considering the tap-weight wrap around problem. Also, the sampling frequency and phase are jointly acquired with the tap-weights. The acquisition performance is good for the relative amplitude b of mid-band fading less than 0.95 or greater than 1.10 and is not noticeably dependent on whether the eye is open or closed due to multipath. The acquisition performance is particularly good for the NMP sampling phase locus, where the eigenvalue spread is smallest. It can also be noted that the region of multipath where acquisition of the implemented system is now impossible (by initializing to zero) is the region with either a large sum of eigenvalues or the region with high eigenvalue spreads. There is the potential for better acquisition if the wrap around problem was removed or possibly if the misadjustment noise in the tap-weights for relative amplitudes between 0.90 and 1.10 was reduced.

v) In the calculated theoretical performance with respect to multipath it is seen that large impulse response tails which are outside the time span of the equalizer can cause the desired local minimum in the MSE with respect to sampling phase to disappear for off band centre fading. Therefore, minimizing the tails of the system impulse response is important for good operation of the clock recovery function. Of course, minimizing the system impulse response outside the time span of the equalizer will also help to provide a lower MMSE. In future work, the measured system impulse response or measured amplitude and group delay versus frequency may be analysed to determine if fixed amplitude or group delay equalizers could be used to reduce any impulse response tails due to the equipment, that are outside the time span of the equalizer and thereby, improve the implemented system performance.

vi) The use of one bit quantized instantaneous gradient estimate works well in parameter adaptation when the up-down counter method of Lucky is used to "average" the instantaneous estimates. However, Lucky's formula for estimating the size of the up-down counters assumes independence between parameters and does not predict the misadjustment noise that results in the implemented system for relative amplitudes b between .90 and 1.1 for the MP sampling phase locus. In future work, it would be very useful to theoretically relate the eigenvalues and eigenvectors to the misadjustment noise and the size of the up-down counter register C when Lucky's up-down counter method is used with a one bit gradient.

vii) The independent adjustment of tap-weights affecting I-axis and Q-axis greatly reduces sensitivity of the BER to the amplitude and phase imbalances experienced in quadrature modulation or demodulation.

viii) In the implemented system, there are several obvious changes and improvements to be made in the future. First, all the problems noted throughout this thesis have to be corrected. Also, the carrier recovery function must be implemented. It is anticipated that if there is a problem with the system proposed in Chapter 3, that it would likely be in relation to acquisition performance, since with the proposed system in Chapter 3 system acquisition would involve carrier and clock frequency and phase acquisition as well as acquisition of 40 decision-directed tap-weights. As the DFE can resolve any carrier phase, the only requirement for carrier recovery is to determine the carrier frequency and to minimize any change in phase that the DFE could not track. With this in mind, an alternative to consider for carrier recovery would be a squaring loop or Costas loop which could operate independently of the DFE. In addition, if it was desired to decouple the clock or sampling frequency acquisition from the DFE, but retain the MMSE sampling phase estimation, the system shown in Figure 6.2 could be considered. The size N_f of the frequency divider in Figure 6.2 would depend on the distance in phase that it was desired to pull the first order phase locked loop.

ix) The outage (at 10^{-3}) region measured in the b-f_o plane at an SNR of 51 dB using the implemented five forward and five backward tap DFE was better than that obtained for any constructed system in existence (measured at higher SNR) for notch frequency offsets within 5MHz of mid-band. For notch frequency offsets greater than 5MHz from mid-band the outage signature quickly grows significantly worse than outage regions previously obtained by others. Problems in implementation are responsible for obtaining less than the full potential of the DFE to equalize multipath. In order to determine the full potential of the DFE more research is required to eliminate the limitations due to implementation and to obtain a better theoretical description of the system in order to confirm the potential operation of the implemented system. Future work planned to improve the theoretical description is previously stated in this section. If the off-band-centre fading performance is not

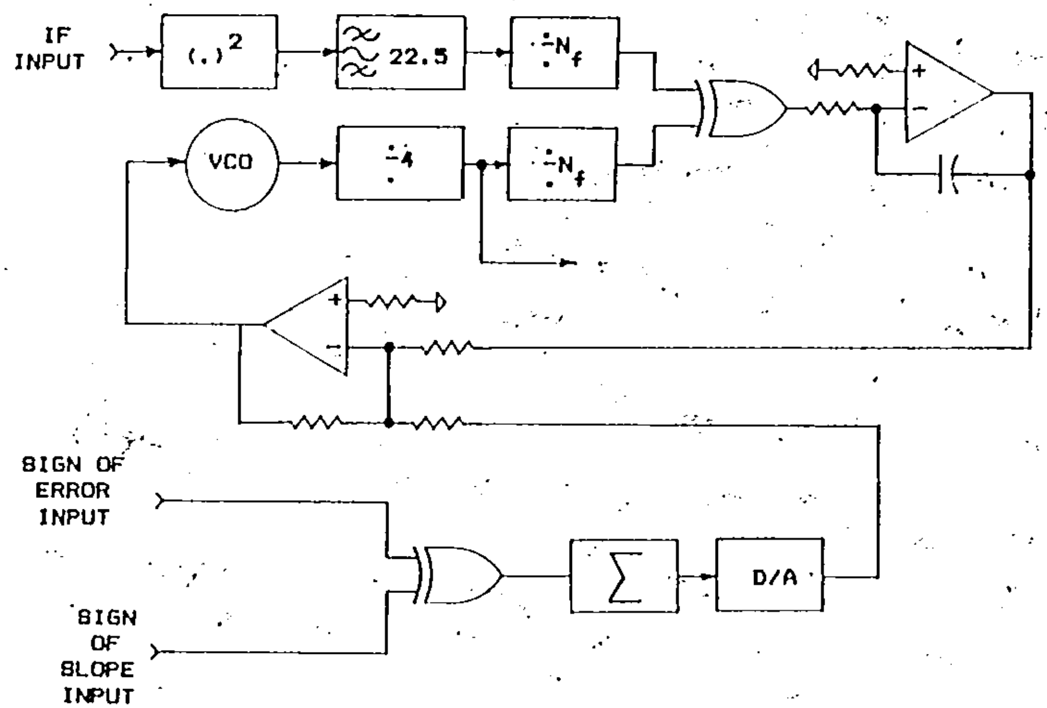

Figure 6.2 A Clock Recovery System With Squaring Loop Derived Frequency Control and MMSE Derived Phase Control

satisfactory after future improvements, then it may be wise at that point to examine the use of an adaptive slope amplitude versus frequency equalizer, since these equalizers are used successfully in nearly all the second generation radio systems.

x) It has not been emphasized in this thesis, but it is important to consider the tracking ability of the adaptive system with respect to the rate of change of multipath, and this is left for future work.

REFERENCES

[1] S. Barber, P.R. Hartman, "An Overview of High Capacity Radio Transmission Systems in North America", IEEE ICC'84, Amsterdam, June 1984, pp. 975-

[2] Roadhouse, Fellows, Spencer, "The Trans-Canada Digital Radio Network", IEEE ICC'77, Chicago, June 1977

[3] "Standard Radio System Plan", SRSP-302, Issue 2, Communications Canada, June 29, 1973

[4] Draft 784-1, Effects of Propagation on the Design and Operations of Line of Sight Radio Relay Systems. International Radio Consultave Committee, 2 Rue de Varembe, Geneva, Switzerland

[5] I. Godier, "DRS-8 Digital Radio for Long Haul Transmission", IEEE ICC'77, Chicago, Illinois, June 12-15, 1977, pp. 5.4-102 - 5.4-105

[6] C. Anderson, S. Barber, R. Patel, "Propagation Experiments Show Path to Success", Telesis, Special Issue:DRS-8 Digital Radio System, Bell Northern Research, Ottawa, Canada, December 1977

[7] R. F. White, Engineering Considerations for Microwave Communications Systems, Lenkurt Electric Co. Inc., San Carlos,CA, USA, June 1970

[8] W.T. Barnett, "Multipath Propagation at 4, 6, and 11 GHz", Bell System Technical Journal, Vol. 51, Feb. 1972, pp. 321-361

[9] C.W. Anderson, S. Barber, R. Patel, "The Effects of Selective Fading on Digital Radio", IEEE ICC'78, Toronto, Canada, June 4-7, 1978

[10] W.C. Jakes, Jr."An Approximate Method to Estimate an Upper Bound on the Effect of Multipath Delay Distortion on Digital Transmission", IEEE ICC'78, June 1978, pp. 47.1.1 - 47.1.5. Also published in IEEE Trans. Comm., COM-27, NO. 1, Jan. 1979, pp. 76-81

[11] M. Emshwiller, "Characterization of the Performance of PSK Digital Radio Transmission in the Presence of Multipath Fading", IEEE ICC'78, June 1978, pp.47.3.1. - 47.3.6

[12] V.K. Prabhu, L.J. Greenstein, "Analysis of Multipath Outage With Applications to 90 Mb/s Systems at 6 and 11 GHz", IEEE ICC'78, Toronto, June 4-7, 1978, pp. 47.2.1-

[13] W.D. Rummler, "A Multipath Channel Model for Line-of-Sight Digital Radio Systems", IEEE ICC'78, Toronto, June 4-7, 1978, pp. 47.5-

[14] W.T. Barnett, "Measured Performance of a High Capacity 6 GHz Digital Radio System", IEEE ICC'78, Toronto, June 4-7, 1978, pp.47.4-

[15] L.J. Greenstein, "A Multipath Fading Channel Model for Terrestrial Digital Radio Systems", IEEE Trans. Comm., Vol.COM-26, No. 8, August 1978, pp. 1247-1250

[16] Y.Ito, T. Ryu, Y. Kitahara, T. Noguchi, "Design and Performance of 6 GHz 135 Mb/s Radio System with 64QAM", IEEE ICC'84, Amsterdam, June 1984, pp.632-

[17] J.A. Crosset, P.R. Hartman, "64 QAM Digital Radio Transmission System Integration and Performance", IEEE ICC'84, Amsterdam, June 1984, pp.636-

[18] S. Takenaka, Y. Takeda, T. Sakane, H. Nakamura, N. Toyonaga, "A New 4GHz 90Mb/s Digital Radio System Using 64-QAM Modulation", IEEE ICC'84, Amsterdam, June 1984, pp.642-645

[19] J.D.McNicol, S.G. Barber, F. Rivest, "Design and Application of the RD-4A and RD-6A QAM Digital Radio Systems", IEEE ICC'84, Amsterdam, June 1984

[20] G.H. Niezgoda, D.P. Taylor, M. Shafi, "Further Results on the Dispersive Fade Performance of a 49QPRS 90 Mb/s Digital Radio", IEEE ICC'84, Amsterdam, 1984, pp. 998-1002

[21] J.G. Smith, "Bandwidth Compressive Modulation Systems", AIAA/CASI 6th Communication Satellite Systems Conference, Montreal, Canada, April 1976

[22] J. Grabowski, R.C. Davis, "An Experimental M-QAM Modem Using Amplifier Linearization and Baseband Equalization Techniques", NTC82, Galveston, Texas, 1982

[23] N.A. Liskov, A. Wood, Raytheon Co., verbal communication

[24] R. Davis, W.Boyd, "Adaptive Predistortion Technique for Linearizing a Power Amplifier for Digital Data Systems". U.S.A. Patent 4291277, Sept. 22,1981

[25] Miyauchi, Seki Ishio, "New Technique for Generating and Detecting Multilevel Signal Formats", IEEE Trans. Comm., Vol. COM-24, Feb. 1976, pp. 263-267

[26] H. Seidel, "A Microwave Feed-Forward Experiment", Bell Systems Technical Journal, Vol. 50, #9, Nov. 1971, pp. 2879-2916

[27] H.S. Black, U.S. Patent 1686792, Oct. 9, 1929

[28] H.S. Black, "Stabilized Feedback Amplifiers", Bell Systems Technical Journal, Vol. 13, Jan. 1934, pp.1-18

[29] D.P. Taylor, K.S. Yeung, "Conceptual Design of a 4/b/s/Hz Radio System", IEEE ICC'79, Boston, Mass., June 11-14, 1979, pp. 5.8.1 - 5.8.5

[30] D.P. Taylor, M. Shafi, "Decision Feedback Equalization for Multipath Induced Interference in Microwave Line of Sight Links", IEEE Trans. Comm., Vol. COM-32, No. 3, March 1984, pp. 269-279

[31] G.R. McMillen, M. Shafi, D.P. Taylor, "Simultaneous Adaptive Estimation of Carrier Phase, Symbol Timing and Data, for a 49QPRS DFE Radio Receiver", IEEE Trans. Comm., Vol. COM-32, No. 4, April 1984, pp. 429-443

[32] P. Monsen, "Feedback Equalization for Fading Dispersive Channels", IEEE Trans. Inform. Theory, IT-17, no. 1, Jan. 1971, pp. 56-64

[33] J.W. Milnor, U.S.Patent 1 717 116, June 11, 1929

[34] L.A. McColl, U.S. Patent 2 056 284, October 6, 1936

[35] M. Austin, "Decision Feedback Equalization for Digital Communications Over Dispersive Channels", M.I.T. Res. Lab. Electron., Tech. Rep. 461, August 1967

[36] C.A. Belfiore, J.H. Park, "Decision Feedback Equalization", Proceedings of the IEEE, Vol. 69, No. 8, August 1979, pp. 1143-1156

[37] P. Monsen, "Adaptive Equalization of the Slow Fading Channel", IEEE Trans. Comm., COM-22, August 1974, pp. 1064-1075

[38] D.A. George, R.R. Bowen, J.R. Storey, "An Adaptive Decision Feedback Equalizer", IEEE Trans. Comm., Vol. COM-19, No. 3, March 1984, pp. 269-279

[39] R.W. Lucky, "Techniques for Adaptive Equalization of Digital Communication Systems", Bell System Technical Journal, Vol. 45, February 1966, pp. 255-286

[40] R.W. Chang, "Joint Equalization, Carrier Acquisition and Timing Recovery for Data Communication", IEEE ICC'70, San Francisco, June 1970, pp.28-34

[41] H. Kobayashi, "Simultaneous Adaptive Estimation and Decision Algorithm for Carrier Modulated Data Transmission Systems",IEEE COM-19, June 1971, pp. 268-

[42] S. Qureshi, "Timing Recovery for Equalized Partial Response Systems", IEEE Trans. Comm., Vol. COM-24, No. 3, pp. 1326-1330

[43] B. R. Salzberg, "Timing Recovery for Synchronous Binary Data Transmission", Bell System Technical Journal, Vol. 46, 1967, pp. 593-622

[44] R.D. Gitlin, J. Salz, "Timing Recovery in PAM Systems", Bell Systems Technical Journal, Vol. 50, May-June 1971, pp.1645-1669

[45] H. Sailer, "Timing Recovery in Data Transmission Systems Using Partial Response", IEEE ICC'75, Boston, Mass.,June 1975

[46] D.D. Falconer, "Jointly Adaptive Equalization and Carrier Recovery in Two-Dimensional Digital Communication Systems", Bell Systems Technical Journal, March 1976, pp. 317-334

[47] G.H. Niezgoda, D.P. Taylor, "Effects of Non-Minimum Phase Fades on the Performance of 49QPRS 90Mb/s Digital Radio Using Decision Feedback Equalization", Globe Comm'83, San Diego, California, Dec. 1983

[48] C.A. Siller, " Multipath Propagation", IEEE Communications Magazine, February 1984, Vol. 22, No. 2, pp. 6-15

[49] P. Monsen, "Fading Channel Communications", IEEE Communications Magazine, Vol. 18, No.1, January 1980, pp.16-25

[50] S. Qureshi, "Adaptive Equalization", IEEE Communications Magazine, Vol. 20, No. 2, March 1982, pp. 9-16

[51] "Policies and Procedures for the Use of Digital Modulation Techniques in Microwave Radio", Federal Communications Commission Docket 19311, September 27, 1974

[52] R.W.Lucky, J.Salz, E.J. Weldon, Principles of Data Communications, New York: McGraw-Hill, 1968

[53] F.M. Gardner, Phaselock Techniques, New York: John Wiley & Sons, Second Edition, 1969

[54] D.R. Green, Jr. "Characterization and Compensation of Nonlinearities in Microwave Transmitters", IEEE Globecom'82, Miami, November 29-Dec. 2, 1982, pp.A7.5

[55] S. Pasupathy, "Correlative Coding - A Bandwidth Efficient Signalling Scheme", IEEE Communications Society Magazine, July 1977, pp. 4-11

[56] W.T. Barnett, "Deterioration of Cross-Polarization Discrimination During Rain and Multipath Fading at 4GHz", IEEE ICC'74, Minneapolis, Minn., June 17-19, 1974, pp. 12D-1,4

[57] G.R. McMillen, "Joint Carrier and Timing Recovery Considerations for a 4.5 bits/s/Hz Digital Radio System", M.Eng. Thesis, McMaster University, September 1981

[58] W. Weber, "Differential Encoding for Multiple Amplitude and Phase Shift Keying Systems", IEEE Trans. Comm., Vol. COM-26, March 1978, pp. 385-391

[59] G.R. McMillen, "Joint Carrier and Timing Recovery Considerations for a 4.5b/s//Hz Digital Radio", Communications Research Lab, McMaster University, Hamilton, Ontario, Report No. CRL-104, Sept. 1982

[60] A. Leclert, P. Vandamme, "Decision Feedback Equalization of Dispersive Radio Channels", IEEE COM-33, No.7, July 1985, pp. 676-684

[61] M. Shafi, D.P. Taylor, "Fade Margin And Outage Computation for a 49QPRS Radio Employing Decision Feedback Equalization", IEEE ICC'83, Boston, Mass., June 19-22, 1983, pp.F2.1.1 - F2.1.6

[62] C.F. Weaver, D.P. Taylor, "The Implementation of Adaptive Decision Feedback Equalization of Multipath Distortion in Microwave Radio", Globe Comm'84, Atlanta, Georgia, 1984

[63] C.F. Weaver, "Feedback Linearization of Power Amplified for Digital Microwave Communications", NTC 82, Galveston, Texas, November 7-10, 1982

[64] G.H. Niezgoda, "A Comparitive Study of the 49QPRS and 64 QAM 90 Mb/s Digital Radios", M. Eng. Thesis, McMaster University, April 1985

[65] K.S. Yeung, "A Bandwidth Efficient Digital Radio System", Communications Research Lab., McMaster University, Hamilton, Canada, Report No. CRL-82, September 1980

[66] M.T. Dudek et al., "Design and Performance of a 4.5-bit/s/Hz Digital Radio Using Reduced Bandwidth QPSK", Globecom'82, Nov.-Dec. 1982, pp. D3.4.1-D3.4.5

[67] T. Murase et al., "200 Mb/s 16-QAM Digital Radio System With New Countermeasure Techniques for Multipath Fading", IEEE ICC'81, Denver, Colorado, June 14-18, 1981, pp.46.1.1 - 46.1.5

[68] S.Haykin, Adaptive Filter Theory, Prentice-Hall, to be published, 1986

[69] P.A. Bello, "Characterization of Randomly Time-Variant Linear Channels", IEEE Trans. Commun. Syst., Vol. CS-11, Dec. 1963, pp.360-393

[70] D. Hirsch, W.J. Wolf, "Adaptive Equalizer for Data Transmission ", IEEE Trans. Commun. Technol., COM-18, No. 1, Feb. 1970, pp. 5-11

[71] J.E. Mazo, "Analysis of Decision-Directed Equalizer Convergence", Bell System Technical Journal, Vol. 59, Dec. 1980, pp. 1857-1876

[72] A. Gersho, "Adaptation in a Quantized Parameter Space", Sixth Annual Allerton Conference on Circuit and System Theory, Monticello, Illinois, October 1968

[73] W.D. Rummler, "Modeling the Diversity Performance of Digital Radios With Maximum Power Combiners", IEEE ICC'84, Amsterdam, June 1984, pp.657-660

[74] T. Noguchi, T. Ryu, Y. Koizumi, S. Mizoguchi, M. Yoshimoto, and K. Nakamura, "6 GHz 135 MBPPS Digital Radio System With 64QAM Modulation", IEEE ICC'83, Boston, Mass., June 1983

[75] C.P. Bates, M.A. Skinner, "Impact of Technology on High Capacity Digital Radio Systems, IEEE ICC'83, Boston, Mass., June 1983

[76] K.H. Mueller, M. Muller, "Timing Recovery in Digital Synchronous Data Receivers," IEEE Trans. on Comm., COM-21, No. 3, May 1976, pp. 516-531